Fundamentals of Radar Imaging

CBMS-NSF REGIONAL CONFERENCE SERIES IN APPLIED MATHEMATICS

A series of lectures on topics of current research interest in applied mathematics under the direction of the Conference Board of the Mathematical Sciences, supported by the National Science Foundation and published by SIAM.

GARRETT BIRKHOFF, *The Numerical Solution of Elliptic Equations*
D. V. LINDLEY, *Bayesian Statistics, A Review*
R. S. VARGA, *Functional Analysis and Approximation Theory in Numerical Analysis*
R. R. BAHADUR, *Some Limit Theorems in Statistics*
PATRICK BILLINGSLEY, *Weak Convergence of Measures: Applications in Probability*
J. L. LIONS, *Some Aspects of the Optimal Control of Distributed Parameter Systems*
ROGER PENROSE, *Techniques of Differential Topology in Relativity*
HERMAN CHERNOFF, *Sequential Analysis and Optimal Design*
J. DURBIN, *Distribution Theory for Tests Based on the Sample Distribution Function*
SOL I. RUBINOW, *Mathematical Problems in the Biological Sciences*
P. D. LAX, *Hyperbolic Systems of Conservation Laws and the Mathematical Theory of Shock Waves*
I. J. SCHOENBERG, *Cardinal Spline Interpolation*
IVAN SINGER, *The Theory of Best Approximation and Functional Analysis*
WERNER C. RHEINBOLDT, *Methods of Solving Systems of Nonlinear Equations*
HANS F. WEINBERGER, *Variational Methods for Eigenvalue Approximation*
R. TYRRELL ROCKAFELLAR, *Conjugate Duality and Optimization*
SIR JAMES LIGHTHILL, *Mathematical Biofluiddynamics*
GERARD SALTON, *Theory of Indexing*
CATHLEEN S. MORAWETZ, *Notes on Time Decay and Scattering for Some Hyperbolic Problems*
F. HOPPENSTEADT, *Mathematical Theories of Populations: Demographics, Genetics and Epidemics*
RICHARD ASKEY, *Orthogonal Polynomials and Special Functions*
L. E. PAYNE, *Improperly Posed Problems in Partial Differential Equations*
S. ROSEN, *Lectures on the Measurement and Evaluation of the Performance of Computing Systems*
HERBERT B. KELLER, *Numerical Solution of Two Point Boundary Value Problems*
J. P. LASALLE, *The Stability of Dynamical Systems*
D. GOTTLIEB AND S. A. ORSZAG, *Numerical Analysis of Spectral Methods: Theory and Applications*
PETER J. HUBER, *Robust Statistical Procedures*
HERBERT SOLOMON, *Geometric Probability*
FRED S. ROBERTS, *Graph Theory and Its Applications to Problems of Society*
JURIS HARTMANIS, *Feasible Computations and Provable Complexity Properties*
ZOHAR MANNA, *Lectures on the Logic of Computer Programming*
ELLIS L. JOHNSON, *Integer Programming: Facets, Subadditivity, and Duality for Group and Semi-Group Problems*
SHMUEL WINOGRAD, *Arithmetic Complexity of Computations*
J. F. C. KINGMAN, *Mathematics of Genetic Diversity*
MORTON E. GURTIN, *Topics in Finite Elasticity*
THOMAS G. KURTZ, *Approximation of Population Processes*
JERROLD E. MARSDEN, *Lectures on Geometric Methods in Mathematical Physics*
BRADLEY EFRON, *The Jackknife, the Bootstrap, and Other Resampling Plans*
M. WOODROOFE, *Nonlinear Renewal Theory in Sequential Analysis*
D. H. SATTINGER, *Branching in the Presence of Symmetry*
R. TEMAM, *Navier–Stokes Equations and Nonlinear Functional Analysis*

MIKLÓS CSÖRGO, *Quantile Processes with Statistical Applications*
J. D. BUCKMASTER AND G. S. S. LUDFORD, *Lectures on Mathematical Combustion*
R. E. TARJAN, *Data Structures and Network Algorithms*
PAUL WALTMAN, *Competition Models in Population Biology*
S. R. S. VARADHAN, *Large Deviations and Applications*
KIYOSI ITÔ, *Foundations of Stochastic Differential Equations in Infinite Dimensional Spaces*
ALAN C. NEWELL, *Solitons in Mathematics and Physics*
PRANAB KUMAR SEN, *Theory and Applications of Sequential Nonparametrics*
LÁSZLÓ LOVÁSZ, *An Algorithmic Theory of Numbers, Graphs and Convexity*
E. W. CHENEY, *Multivariate Approximation Theory: Selected Topics*
JOEL SPENCER, *Ten Lectures on the Probabilistic Method*
PAUL C. FIFE, *Dynamics of Internal Layers and Diffusive Interfaces*
CHARLES K. CHUI, *Multivariate Splines*
HERBERT S. WILF, *Combinatorial Algorithms: An Update*
HENRY C. TUCKWELL, *Stochastic Processes in the Neurosciences*
FRANK H. CLARKE, *Methods of Dynamic and Nonsmooth Optimization*
ROBERT B. GARDNER, *The Method of Equivalence and Its Applications*
GRACE WAHBA, *Spline Models for Observational Data*
RICHARD S. VARGA, *Scientific Computation on Mathematical Problems and Conjectures*
INGRID DAUBECHIES, *Ten Lectures on Wavelets*
STEPHEN F. MCCORMICK, *Multilevel Projection Methods for Partial Differential Equations*
HARALD NIEDERREITER, *Random Number Generation and Quasi-Monte Carlo Methods*
JOEL SPENCER, *Ten Lectures on the Probabilistic Method, Second Edition*
CHARLES A. MICCHELLI, *Mathematical Aspects of Geometric Modeling*
ROGER TEMAM, *Navier–Stokes Equations and Nonlinear Functional Analysis, Second Edition*
GLENN SHAFER, *Probabilistic Expert Systems*
PETER J. HUBER, *Robust Statistical Procedures, Second Edition*
J. MICHAEL STEELE, *Probability Theory and Combinatorial Optimization*
WERNER C. RHEINBOLDT, *Methods for Solving Systems of Nonlinear Equations, Second Edition*
J. M. CUSHING, *An Introduction to Structured Population Dynamics*
TAI-PING LIU, *Hyperbolic and Viscous Conservation Laws*
MICHAEL RENARDY, *Mathematical Analysis of Viscoelastic Flows*
GÉRARD CORNUÉJOLS, *Combinatorial Optimization: Packing and Covering*
IRENA LASIECKA, *Mathematical Control Theory of Coupled PDEs*
J. K. SHAW, *Mathematical Principles of Optical Fiber Communications*
ZHANGXIN CHEN, *Reservoir Simulation: Mathematical Techniques in Oil Recovery*
ATHANASSIOS S. FOKAS, *A Unified Approach to Boundary Value Problems*
MARGARET CHENEY AND BRETT BORDEN, *Fundamentals of Radar Imaging*

MARGARET CHENEY
Rensselaer Polytechnic Institute
Troy, New York

BRETT BORDEN
The Naval Postgraduate School
Monterey, California

Fundamentals of Radar Imaging

SOCIETY FOR INDUSTRIAL AND APPLIED MATHEMATICS
PHILADELPHIA

10 9 8 7 6 5 4 3 2 1

Library of Congress Cataloging-in-Publication Data
Cheney, Margaret, 1955-
Fundamentals of radar imaging / Margaret Cheney, Brett Borden.
p. cm. -- (CBMS-NSF regional conference series in applied mathematics ; 79)
Includes bibliographical references and index.
ISBN 978-0-898716-77-1
1. Radar. I. Borden, Brett, 1954- II. Conference Board of the Mathematical Sciences. III. National Science Foundation (U.S.). IV. Title.
TK6575.C476 2009
621.3848--dc22

2009022439

To Our Parents

Contents

List of Figures

List of Tables

Preface

Radar imaging is a subject of tremendous mathematical richness, with many interesting applications and many challenging open problems that are of a mathematical nature. Yet the topic is almost completely unknown in the mathematical community. This is because the field was developed within the engineering community, and the engineering literature is difficult for mathematicians to penetrate.

Mathematicians tend to like an axiomatic approach: they like to begin with one or more partial differential equations, say, the wave equation or Maxwell's equations, and derive everything from these equations. Physicists, on the other hand, are comfortable beginning with *solutions* of the fundamental equations. Engineers, in contrast, are able to begin with the key *part* of the solution, and proceed from there. Consequently mathematicians find it difficult to read the engineering literature because they don't understand where the *first* equation comes from. The goal of this monograph is to fill that gap and to show how radar imaging arises from the fundamental partial differential equations.

The focus here is on showing the connection between the physics and the mathematics, and on supplying an intuitive mathematical understanding of the basic ideas. Consequently, we ignore many issues of rigor, such as questions about the relevant function spaces and the precise conditions under which interchange of integrals is valid, because attention to these issues would only distract from the focus on the underlying ideas. We hope that this approach will provide a foundation that will enable mathematical readers to begin to read the extensive engineering literature and to start working in the field.

We have provided some references to ongoing work, but we have made no attempt at a complete literature survey or detailed history.

M.C. first developed this material for her Mathematical Sciences course "Introduction to Radar Imaging," a course that borrowed liberally from material prepared by B.B. for physics graduate students at the Naval Postgraduate School. M.C. then developed a ten-lecture version of the Radar Imaging course, first for a tutorial in September 2005 at the Institute for Mathematics and Its Applications, and then again for a lecture series in May 2008 at the University of Texas at Arlington. The latter lecture series was arranged by Tuncay Aktosun and was supported by the Conference Board of the Mathematical Sciences (CBMS). The present monograph corresponds to the CBMS ten-lecture series.

The assumed background for this material consists of the following.

- **A little complex analysis** (in particular Euler's relation $e^{i\theta} = \cos\theta + i\sin\theta$). We use a star ($*$) for complex conjugate.

- **The Fourier transform** [71, 97].

$$f(t) = \int e^{-2\pi i \nu t} F(\nu) d\nu = \frac{1}{2\pi} \int e^{-i\omega t} \tilde{F}(\omega) d\omega, \tag{1}$$

where $\tilde{F}(\omega) = F(2\pi\nu)$ with $\omega = 2\pi\nu$. There are different conventions regarding whether f is called the Fourier transform of F or $\tilde{F}$ or $\tilde{F}/(2\pi)$; these correspond to different choices about where to put the 2π, and we actually use different conventions at different places in the text. We use $\mathcal{F}$ to denote the Fourier transform operator.

  - We also need the inverse Fourier transform

$$F(\nu) = \int e^{2\pi i \nu t} f(t) dt \tag{2}$$

    or, depending on the 2π convention,

$$\tilde{F}(\omega) = \int e^{i\omega t} f(t) dt. \tag{3}$$

    There are also different conventions regarding whether it is the forward transform or inverse transform that has the minus sign in the exponent; the important thing is that the forward and inverse transforms have different signs.
  - A simple consequence of the definition is that when f is real-valued, its Fourier transform obeys the relation $F(-\nu) = F^*(\nu)$.
  - We also need the convolution theorem

$$(f * g)(t) = \int e^{-2\pi i \nu t} F(\nu) G(\nu) d\nu, \tag{4}$$

    where the convolution is defined by

$$(f * g)(t) = \int f(t - t') g(t') dt'. \tag{5}$$

  - We also need the fact that smoothness of a function corresponds to rapid decay of its Fourier transform [71]; this connection can be seen by integrating the Fourier transform by parts.
  - The connection between smoothness and decay is closely related to the *Paley–Wiener theorem* [71], which states that a function $F(\omega)$ that is identically zero for negative ω has a Fourier transform that is analytic in the upper half-plane.
  - Finally, we need the n-dimensional Fourier transform and its inverse:

$$f(\boldsymbol{x}) = \frac{1}{(2\pi)^n} \int e^{-i\boldsymbol{x}\cdot\boldsymbol{\xi}} F(\boldsymbol{\xi}) d\boldsymbol{\xi}, \qquad F(\boldsymbol{\xi}) = \int e^{i\boldsymbol{x}\cdot\boldsymbol{\xi}} f(\boldsymbol{x}) d\boldsymbol{x}. \tag{6}$$

- **The Dirac delta function** δ [54], which has the property

$$\int \delta(t) f(t) dt = f(0), \tag{7}$$

and the Fourier transform of the delta function,

$$\delta(t) = \int e^{2\pi i \nu t} d\nu = \frac{1}{2\pi} \int e^{i\omega t} d\omega, \tag{8}$$

are used repeatedly throughout the text. If t is replaced by $t - t'$ in (8), the resulting identity can also be thought of as a shorthand for the Fourier transform followed by its inverse.

- **The one-dimensional wave equation**

$$\frac{\partial^2 u}{\partial x^2} - \frac{1}{c^2} \frac{\partial^2 u}{\partial t^2} = 0$$

and its traveling-wave solutions [62], [132].

- **Facts from vector calculus**
  - Spherical coordinates.
  - If the vector field $\boldsymbol{B}$ has zero divergence, then $\boldsymbol{B}$ can be written as the curl of a vector field.
  - If the curl of a vector field $\boldsymbol{E}$ is zero, then $\boldsymbol{E}$ can be written as the gradient of a scalar function.
  - A few vector identities, including

$$\nabla \times (\nabla \times \boldsymbol{E}) = \nabla(\nabla \cdot \boldsymbol{E}) - \nabla^2 \boldsymbol{E} \tag{9}$$

    and the "BAC-CAB" identity

$$\boldsymbol{A} \times (\boldsymbol{B} \times \boldsymbol{C}) = \boldsymbol{B}(\boldsymbol{A} \cdot \boldsymbol{C}) - \boldsymbol{C}(\boldsymbol{A} \cdot \boldsymbol{B}). \tag{10}$$

  - The divergence theorem

$$\int_\Omega \nabla \cdot \boldsymbol{V} \, d\boldsymbol{x} = \int_{\partial\Omega} \hat{n} \cdot \boldsymbol{V} \, dS \tag{11}$$

    and its less well-known analogue [62]

$$\int_\Omega \nabla \times \boldsymbol{V} \, d\boldsymbol{x} = \int_{\partial\Omega} \hat{n} \times \boldsymbol{V} \, dS, \tag{12}$$

    where $\partial\Omega$ denotes the boundary of Ω.

- **A little functional analysis**, in particular the following:
  - The definition of L^2 as the vector space of square-integrable functions, together with its inner product $\langle f, g \rangle = \int f(\boldsymbol{x}) g^*(\boldsymbol{x}) d\boldsymbol{x}$.
  - The adjoint of an operator. We denote the adjoint by a dagger.

– The Cauchy–Schwarz inequality:

$$\left| \int h(t) f^*(t) dt \right| \leq \|h\|_2 \|f\|_2, \quad \text{where} \quad \|f\|_2^2 = \int |f(t)|^2 dt \tag{13}$$

with equality only when h is proportional to f.

- **A little linear algebra:** Properties of orthogonal matrices are needed in Chapter 7.
- **A little familiarity with random processes:** The expected value [75], [101] is needed in Chapter 4 .
- **A little physics**:
  - The notions of frequency (denoted by ν), angular frequency (ω), wave speed (c), wavelength (λ), and wave number (k). The relationships $\nu = c/\lambda$, $k = \omega/c$ (in free space), $\omega = 2\pi\nu$, and $k = 2\pi/\lambda$ will be used.
  – Current, voltage, and Ohm's law

$$V = IR, \tag{14}$$

where V is voltage, I is current, and R is resistance.

The notion of a Green's function [119, 132] will also be needed in the text; readers are not assumed to be familiar with this notion, but those who have some familiarity with the concept will feel more comfortable.

Acknowledgments. M.C. is grateful to the many researchers who have generously shared their knowledge, resources, writings, diagrams, and images. She would particularly like to thank the following: Reza Malek-Madani of the Office of Naval Research for including her in the ONR Sea Ice project, which introduced her to radar researchers, in particular to Bob Onstott, who patiently answered many questions about his radar equipment; David Isaacson (RPI) and Gerhard Kristensson (Lund Institute of Technology), who both taught her a great deal about electromagnetics; Lars Ulander of the Swedish Defence Institute, who encouraged her as a mathematician to work in radar; Charles Elachi of the Jet Propulsion Laboratory, who kindly sent copies of his excellent books; Nick Marechal of Aerospace Corporation, who suggested the inclusion of some key topics and who sent helpful figures; Armin Doerry of Sandia National Laboratories, who made available many of the beautiful SAR images; and Jim Van Damme at the Air Force Research Laboratory (AFRL) Sensors Directorate, who provided many of the antenna photographs. She would also like to thank a number of people who read an earlier version, including her former postdoctoral advisor Joe Keller (Stanford University), Matt Ferrara (AFRL), Lorenzo Lo Monte (General Dynamics), and Mike Kupferschmidt (RPI). She is also grateful to Arje Nachman of the Air Force Office of Scientific Research, who tacitly encourages mathematical radar work by supporting her current research, to Tuncay Aktosun, who arranged for the CBMS lectures and did an excellent job hosting the participants, and to the CBMS for supporting the writing of this monograph.

Some of this material has previously appeared in Institute of Physics publications.

Part I

Radar Basics

Chapter 1

Introduction

Radar is an acronym for RAdio Detection And Ranging. Radar was originally developed as a technology for detecting objects and determining their positions by means of *echo-location*, and this remains the principal function of modern radar systems. However, radar systems have evolved over more than seven decades to perform a variety of very complex functions; one such function is imaging.

Radar imaging is a technology that has been developed mainly within the engineering community. There are good reasons for this: some of the critical ingredients are (1) transmitting microwave energy at high power, (2) detecting microwave energy, and (3) interpreting and extracting information from the received signals. The first two problems have to do with the development of appropriate hardware; however, these problems have now largely been solved, although there is ongoing work to make the hardware smaller and lighter. The third problem is essentially a set of mathematical challenges, and this is the area in which most of the current effort is taking place.

Radar imaging is a subject with tremendous mathematical richness. In particular, it involves partial differential equations, scattering theory, microlocal analysis, integral geometry, linear algebra, electromagnetic theory, harmonic analysis, approximation theory, group theory, and statistics.

1.1 Uses for Radar

There are many advantages to using radar for remote sensing. Unlike many optical systems, radar systems can be used during either day or night. Because the long radar wavelengths pass through clouds, smoke, sand, etc., radar systems can be used in all weather. Moreover, some radar systems can penetrate foliage, buildings, soil, and other materials.

Radar can provide very accurate distance (range) measurements and can also measure the rate at which this range is changing.

Radar waves scatter mainly from objects and features whose size is on the same order as the wavelength. This means that radar is sensitive to objects whose length scales range from centimeters to meters, and many objects of interest are in this range.

Radar has many applications, both military and civilian. It is widely used in aviation and transportation, for navigation, for collision avoidance, and for low-altitude flight.

Most of us are familiar with police radar for monitoring vehicle speed. Radar is also used to monitor weather, including Doppler measurements of precipitation and wind velocity. Imaging radar is used for land-use monitoring, agricultural monitoring, and environmental monitoring. Radar systems are used to map surface topography and to measure crustal change. Medical microwave tomography is currently under development.

1.2 A Brief History of Radar up to 1950

The name "radar" was coined in late 1940, but the earliest radar-like devices predate this appellation by almost four decades. (As a palindrome, this name also evokes the basic send/echo idea behind these measurement systems.) Of course, the principles underlying radar are those underlying all classical electromagnetic phenomena and can be formally traced back to James Clerk Maxwell, but this seems to imply an idealized sequential development from theory to experiment that does not really apply to the radar story. Rather, it was probably Heinrich Hertz who started the idea of radio echo-location in the last quarter of the nineteenth century by *experimentally* demonstrating that radio waves could be reflected from objects.

Devotees of Nikola Tesla sometimes attribute the "invention" of radar to his legendary year of 1899 in Colorado Springs. It is more realistic to say that Tesla's actual contribution appears to be only a conceptual description that was probably unknown by other remote sensing investigators until after the first radar sets were being refined. The distinction of "first electromagnetic echo-location device" is generally awarded to a ship anticollision system developed by Christian Hülsmeyer in 1904. Hülsmeyer's invention operated at a frequency of about 700 megahertz (MHz) and was successfully demonstrated to the German Navy and a Dutch shipping company. Because of its limited range, however, it was never put into service.

Radar development began in earnest after Taylor and Young (who were studying radio propagation for the U.S. Navy in 1922) observed reflection phenomena from buildings, trees, and other objects. These results were based on 60 MHz continuous-wave measurements, but, at about the same time, radio *pulse* echo measurements of the altitude of the ionosphere were also (independently) performed. In 1930, Young and Hyland, using a network of transmitters and receivers, observed signal variations that were due to passing aircraft. This event initiated the first significant American radar research effort, which was directed by the Naval Research Laboratory.

In the 1930s, Great Britain and Germany also began their own radar programs. The British program appears to have begun as a fallback effort when the original idea of an electromagnetic "death ray" was shown to be infeasible as a method for air-defense. The German effort, which was initially applied to ship detection, quickly included aircraft echo-location as an important goal. The prewar British radar aircraft detection effort resulted in the famous Chain Home early-warning system, which was a widespread collection of radar transmitters and receivers operated (typically) at about 22–50 MHz. The Chain Home system is credited with saving England from a Nazi invasion.

British and German radar systems were also used for fire control (i.e., systems for aiming and detonating munitions) and aircraft navigation, and, late in the decade, the British succeeded in developing an airborne radar. These radar systems were operated at frequencies from tens to hundreds of megahertz. Higher frequencies, which could increase antenna directivity and allow for smaller antenna sizes, were not used because efficient methods for

their generation were unknown—the klystron tube, which was developed in the late 1930s as a microwave source, lacked the necessary power for radar applications. The big breakthrough came with the British development of the cavity magnetron at the end of the decade.

In 1940 the British began a collaborative research effort with the United States, and, at this time, U.S. researchers were informed of the existence of the cavity magnetron as a means for producing high-power microwaves. A new research center was established at the Radiation Laboratory at MIT, and a usable microwave tracking radar, capable of being mounted in an aircraft, followed in less than six months. Other microwave radar systems were developed for artillery fire-control, improved bombing accuracy, and U-boat detection. Microwave radar components captured from downed British and American aircraft led Germany to adopt the cavity magnetron and begin manufacturing their own microwave radars—although these came too late to have a significant wartime impact. By the end of the war, radar frequencies of 10 gigahertz (GHz) were common.

Radar developments during the war were transitioned to peacetime applications afterward. Notable among these were navigation aids for commercial ships and aircraft as well as shipborne collision avoidance systems. It was the Cold War and Korean conflict, however, that reinvigorated many of the radar research efforts that were downsized after World War II. Improvements in radar sensitivity and the application of frequency shift (Doppler shift) measurements for determining target speed—which were never really used during the war—enabled radars to meet the more demanding requirements imposed by high-speed jet aircraft. In addition, radar sets became small enough to be placed within guided missiles. Advances in signal processing algorithms allowed for the development of increased effective range and improved clutter rejection techniques. Significantly, the tendency toward computer control of radars and computer processing of radar data has become something of a "theme" in modern radar research and development [11, 20, 24, 51, 128, 143] and has led to a need for mathematical research in radar.

1.3 Rudimentary Imaging Methods

At the end of the 1940s, the available radar imaging methods were the following.

1.3.1 Detection and Ranging

Active radar systems accomplish echo-location by transmitting an electromagnetic wave and measuring the reflected field as a time-varying voltage in the radar receiver.

To understand the basic idea of echo-location, we consider an ideal radar system that launches, at time $t = 0$, a short pulse that travels at speed c, reflects from an object at a range R, and returns to the radar. If the return pulse can be detected at a time τ (see Figure 1.2), then because $c\tau = 2R$ (speed $\times$ time = round-trip distance), we can determine that the range R must be equal to $R = c\tau/2$. It is this basic principle upon which much radar theory is based.

1.3.2 High-Range-Resolution (HRR) Imaging

Most objects of interest are not simply isolated point-like targets. For example, if a short radar pulse reflects off a more complicated object like an airplane, the response will be

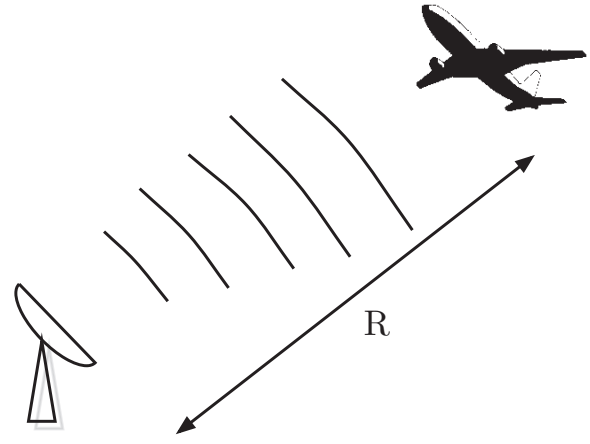

Figure 1.1. *A radar system measuring the distance to a target.*

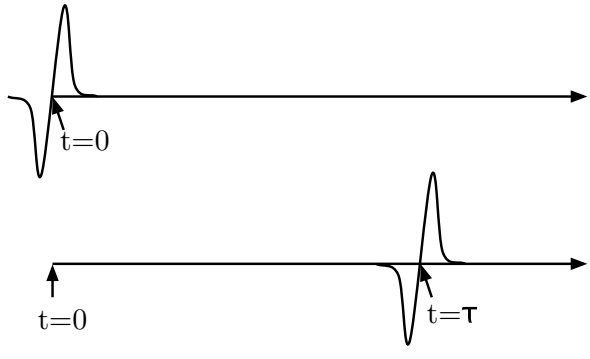

Figure 1.2. *A pulse is transmitted at time zero (top) and received at time τ (bottom).*

a superposition of reflections (see Figure 1.3). Such a response is called a *high-range-resolution* (HRR) profile, and can be considered to be a one-dimensional "image" of the target.

Under some circumstances it may be possible to identify a target from such HRR profiles.

1.3.3 Real-Aperture Imaging

Another imaging approach is to use an antenna that forms a narrow beam and scan the beam over the region to be imaged (see Figures 1.4 and 1.5). At each beam location and pulse delay, the system plots the received intensity. This is called *real-aperture* imaging: the antenna is a physical (real) aperture. The spot on the ground is referred to as the antenna *footprint*.

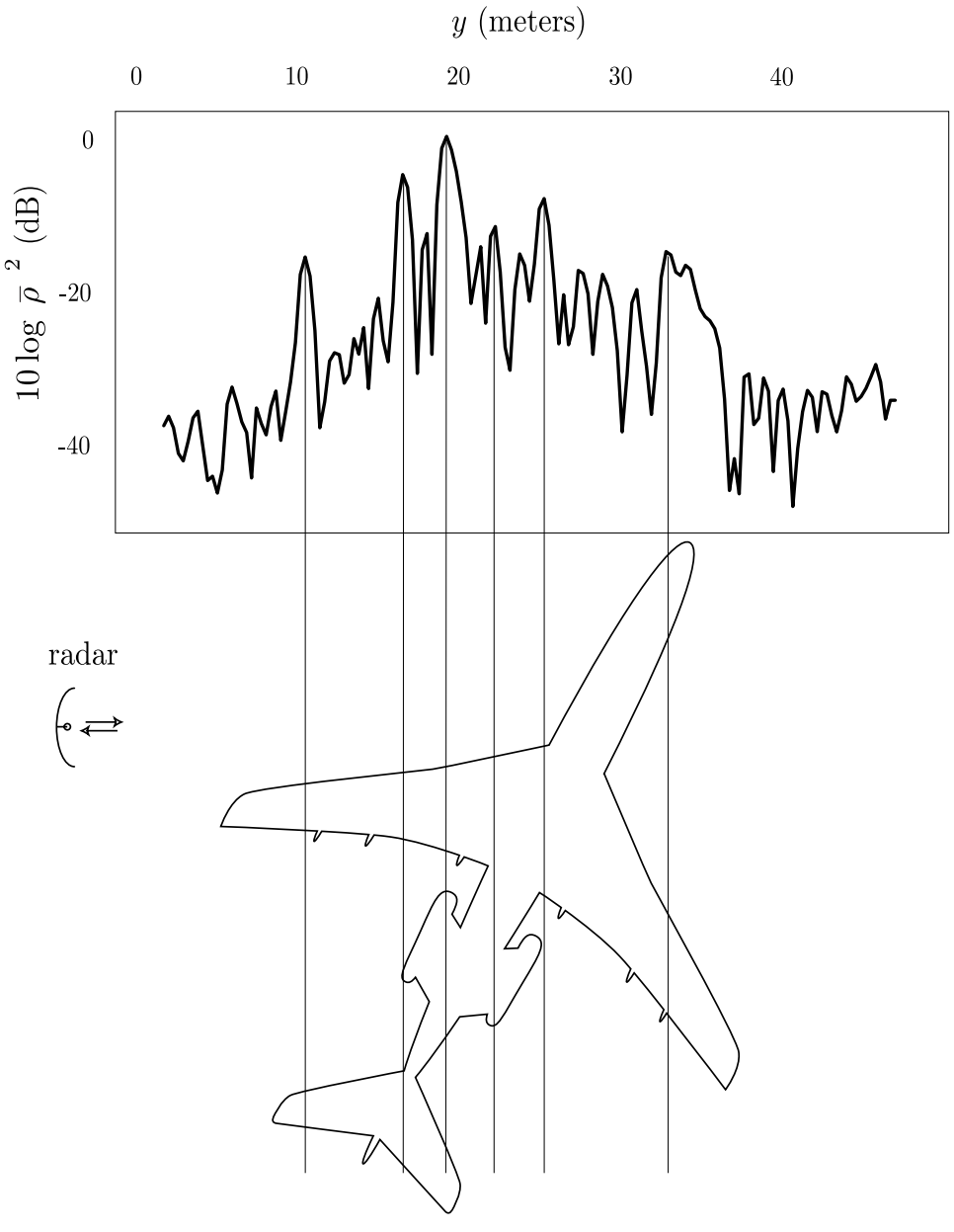

Figure 1.3. *Radar reflections from a complex target.*

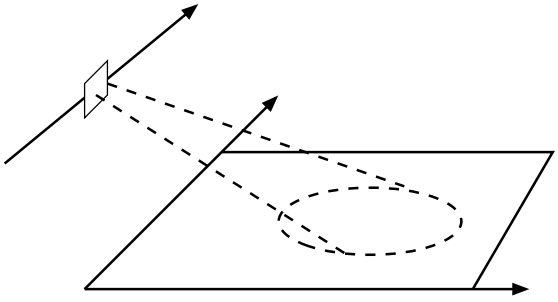

Figure 1.4. *In a real-aperture imaging system, the beam is scanned over the surface, and the scattered intensity is plotted at each location.*

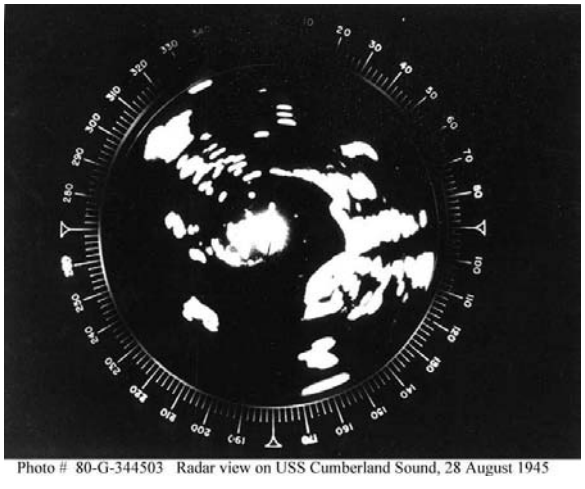

Figure 1.5. *A photograph of a PPI display from the U.S. Navy. This shows Tokyo Bay with U.S. occupation forces, August 28, 1945 (courtesy of the U.S. National Archives).*

An example of real-aperture imaging is a system in which a narrow radar beam sweeps around in a circle. Responses are displayed in polar coordinates on a *Plan Position Indicator* (PPI), shown in Figure 1.5.

1.4 Synthetic-Aperture Radar

A more effective way to form images, *Synthetic-Aperture Radar* (SAR), was developed in the early 1950s. SAR systems use an antenna mounted on a satellite or airplane, which is referred to as the *platform*. As the antenna moves along a flight trajectory, it transmits radio waves and receives the scattered waves (see Figure 1.6). Then mathematical techniques similar to those of X-ray tomography are used to form high-resolution images (see Figure 1.7). It is this form of radar imaging that is the topic of this monograph.

1.5 A Brief History of Synthetic-Aperture Radar

The invention of Synthetic-Aperture Radar (SAR) is generally credited to Carl Wiley, of the Goodyear Aircraft Corporation, in 1951. The mid-1950s saw the development of the first operational systems, under sponsorship of the U.S. Department of Defense. These

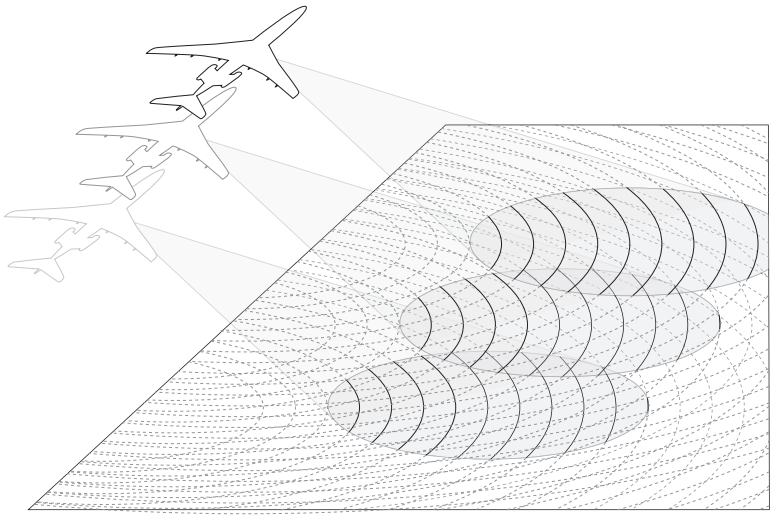

Figure 1.6. *A SAR system.*

Figure 1.7. *A SAR image of Washington, D.C. Although the antenna footprint is typically on the order of tens of kilometers, the images show much smaller features (courtesy of Sandia National Laboratories).*

systems were developed by a collaboration between universities, such as the University of Illinois and the University of Michigan, together with companies such as Goodyear Aircraft, General Electric, Philco, and Varian. In the late 1960s, the National Aeronautics and Space Administration (NASA) began sponsoring unclassified work on SAR. Around this time the first digital SAR processors were developed (earlier systems having used analog optical processing). In 1978 the SEASAT-A satellite was sent up, and even though it operated only for 100 days, the images obtained from it were so useful that it became obvious that more such satellites were needed. In 1981, the Shuttle Imaging Radar (SIR) series began, and

many shuttle missions since then have involved radar imaging of the earth. In the 1990s, satellites were sent up by many countries (including Canada, Japan, and the European Space Agency), and SAR systems were sent to other planets and their moons, including Venus, Mars, and Titan. Since the beginning of the new millennium, more satellites have been launched, including, for example, the new European Space Agency satellite ENVISAT, and the TerraSAR-X satellite, which was developed and launched by a (mainly European) public-private partnership.

1.6 The Equations of Electromagnetic Wave Propagation

Radar waves are electromagnetic waves and are therefore governed by Maxwell's equations. Maxwell's equations in the time domain are

$$\nabla \times \boldsymbol{\mathcal{E}} = -\frac{\partial \boldsymbol{\mathcal{B}}}{\partial t}, \tag{1.1}$$

$$\nabla \times \boldsymbol{\mathcal{H}} = \boldsymbol{\mathcal{J}} + \frac{\partial \boldsymbol{\mathcal{D}}}{\partial t}, \tag{1.2}$$

$$\nabla \cdot \boldsymbol{\mathcal{D}} = \rho, \tag{1.3}$$

$$\nabla \cdot \boldsymbol{\mathcal{B}} = 0. \tag{1.4}$$

Here $\boldsymbol{\mathcal{E}}(t, \boldsymbol{x})$ is the *electric field*, $\boldsymbol{\mathcal{B}}(t, \boldsymbol{x})$ is the *magnetic induction field*, $\boldsymbol{\mathcal{D}}(t, \boldsymbol{x})$ is the *electric displacement field*, $\boldsymbol{\mathcal{H}}(t, \boldsymbol{x})$ is the *magnetic intensity* or *magnetic field*, $\rho(t, \boldsymbol{x})$ is the charge density, and $\boldsymbol{\mathcal{J}}(t, \boldsymbol{x})$ is the current density.

Much of radar wave propagation takes place in dry air, which has electromagnetic properties similar to that of vacuum or *free space*. In free space, we have $\rho(t, \boldsymbol{x}) = 0$ and $\boldsymbol{\mathcal{J}}(t, \boldsymbol{x}) = 0$, together with the free-space constitutive relations

$$\boldsymbol{\mathcal{D}} = \epsilon_0 \boldsymbol{\mathcal{E}} \qquad \text{and} \qquad \boldsymbol{\mathcal{B}} = \mu_0 \boldsymbol{\mathcal{H}}. \tag{1.5}$$

Taking the curl of (1.1) and using the result in (1.2), together with the constitutive relations (1.5), results in

$$\nabla \times \nabla \times \boldsymbol{\mathcal{E}} = -\mu_0 \epsilon_0 \frac{\partial^2 \boldsymbol{\mathcal{E}}}{\partial t^2}. \tag{1.6}$$

To the left side of (1.6), we apply the vector identity (9). In free space, (1.3) takes the form $\nabla \cdot \boldsymbol{\mathcal{E}} = 0$, which imples that (1.6) reduces to

$$\boxed{\nabla^2 \boldsymbol{\mathcal{E}} = \mu_0 \epsilon_0 \frac{\partial^2 \boldsymbol{\mathcal{E}}}{\partial t^2}.} \tag{1.7}$$

Thus in Cartesian coordinates, each component of the vector $\boldsymbol{\mathcal{E}}$ satisfies a scalar wave equation.

The same argument can be applied to $\boldsymbol{\mathcal{H}}$; thus we see that in free space, each component of the electric and magnetic field satisfies the same scalar wave equation, which has a constant wave speed of $c = (\mu_0 \epsilon_0)^{-1/2} \approx 3 \cdot 10^8$m/sec.

Plane Waves. Plane waves are electromagnetic fields of the form

$$\boldsymbol{\mathcal{E}}(t,\boldsymbol{x}) = \boldsymbol{E}e^{-i\omega(t-\hat{\boldsymbol{e}}\cdot\boldsymbol{x}/c)}, \qquad \boldsymbol{\mathcal{H}}(t,\boldsymbol{x}) = \boldsymbol{H}e^{-i\omega(t-\hat{\boldsymbol{e}}\cdot\boldsymbol{x}/c)}, \tag{1.8}$$

where $\hat{\boldsymbol{e}}$ denotes a unit vector. An elementary consequence of Maxwell's equations [62] is that an electromagnetic plane wave must have $\boldsymbol{E}$, $\boldsymbol{H}$, and $\hat{\boldsymbol{e}}$ mutually perpendicular. The field (1.8) is said to be *linearly polarized* with polarization $\hat{\boldsymbol{E}}$. (Here $\hat{\boldsymbol{E}}$ denotes a unit vector in the same direction as $\boldsymbol{E}$.)

Boundary Conditions for a Perfect Electrical Conductor. A perfect electrical conductor (PEC) allows the charges to move freely and instantaneously in response to a field; consequently the fields inside a PEC are zero. It can be shown with the help of the generalized Stokes theorem (12) that the electric and magnetic fields just outside a PEC must satisfy

$$\hat{\boldsymbol{n}} \times \boldsymbol{\mathcal{E}} = \boldsymbol{0} \qquad \text{and} \qquad \hat{\boldsymbol{n}} \times \boldsymbol{\mathcal{H}} = \boldsymbol{\mathcal{J}}_S, \tag{1.9}$$

where $\boldsymbol{\mathcal{J}}_S$ denotes a surface current. In other words, the tangential components of the electric field must be zero, and the tangential components of the magnetic field are connected to currents flowing on the surface of the PEC.

The Wave Equation in the Angular Frequency Domain. If we use the inverse Fourier transform[1]

$$\boldsymbol{E}(\omega) = \int e^{i\omega t}\boldsymbol{\mathcal{E}}(t)dt, \tag{1.10}$$

then (1.7) becomes

$$\boxed{\nabla^2\boldsymbol{E} + k^2\boldsymbol{E} = \boldsymbol{0},}$$

where $k = \omega/c$. Here ω is the angular frequency (radians per second), which is related to the frequency ν in Hertz (cyles per second) as $\omega = 2\pi\nu$. The corresponding wavelength is $\lambda = c/\nu$.

1.7 Radar Frequency Bands

The frequencies that are typically used for radar are the so-called *radio frequencies* (RF), for which the wavelengths range from centimeters to meters (see Tables 1.1 and 1.2). Typically waves scatter mainly from objects whose features are on the same scale as the wavelength.

In practice, radar signals are always of finite duration and therefore technically cannot have Fourier transforms supported only in a finite frequency band [71]. However, in practice, their energy is very small outside some finite interval of frequencies, which is called the frequency *band* of the radar system. The length of this interval is called the *bandwidth* of the system. A more precise definition can be found in many sources [37, 21] but is not needed here.

[1] Here it is convenient to use the convention for the Fourier transform with the 2π in the forward transform and not in the exponent.

Table 1.1. *Radar frequency bands.*

Band designation	Approximate frequency range
HF ("high frequency")	3–30 MHz
VHF ("very high frequency")	30–300 MHz
UHF ("ultra high frequency")	300–1000 MHz
L band	1–2 GHz
S band	2–4 GHz
C band	4–8 GHz
X band	8–12 GHz
Ku band ("under K")	12–18 GHz
K band	18–27 GHz
Ka band ("above K")	27–40 GHz
mm-wave	40–300 GHz

Table 1.2. *Frequencies and wavelengths.*

Frequency ν	Wavelength $\lambda = c/\nu$
1 MHz = 10^6 Hz	300m
10 MHz (HF)	30 m
100 MHz (VHF)	3m
1 GHz = 10^9 Hz (L band)	30 cm
10 GHz (X band)	3 cm
100 GHz (mm-wave)	3 mm

More specifically, most radar systems operate in one of the atmospheric "windows," which are frequency bands in which electromagnetic waves are not absorbed appreciably (see Figure 1.8). In these frequency bands, the free-space constitutive relations (1.5) are generally valid.

Code letters for the radar frequency bands were originally used during wartime, and the usage has persisted. These abbreviations are given in Table 1.1. The HF band usually carries radio signals; VHF carries radio and broadcast television; the UHF band carries television, navigation radar, and cell phone signals. Some radar systems operate at VHF and UHF; these are typically systems built for penetrating foliage, soil, and buildings. Most of the satellite SAR systems operate in the L, S, and C bands. The S band carries wireless internet. Many military systems operate at X band.

1.8 Outline of a Typical Radar System

A description of a radar system is shown in Figure 1.9, which shows the main elements of a generic (and greatly simplified) radar measurement system. (More detail is give in Chapter 2.) An incident time-varying signal $s_{\text{inc}}(t)$ is multiplied by a a *carrier wave*, which is a single-frequency waveform with an (angular) frequency ω_0. The process of multiplying by a carrier wave is referred to as *upmodulation*. Roughly speaking, the signal $s_{\text{inc}}(t)$

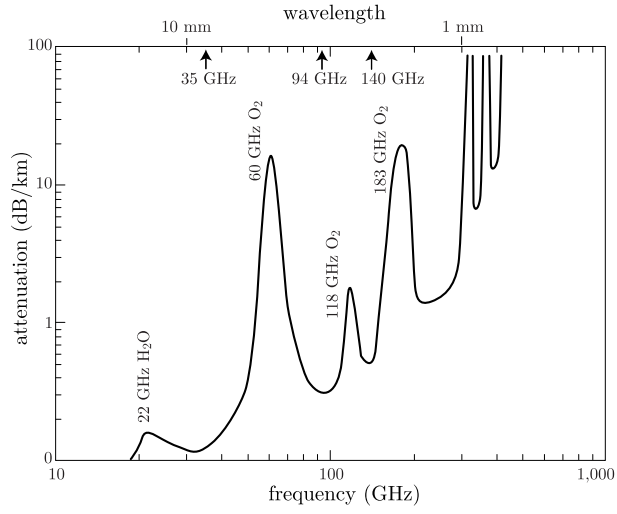

Figure 1.8. *Atmospheric windows for radar wave propagation. Most radar systems operate in bands in which the attenuation is low. Note that both the horizontal and vertical scales are logarithmic; the units on the vertical axis are explained in section 1.9.*

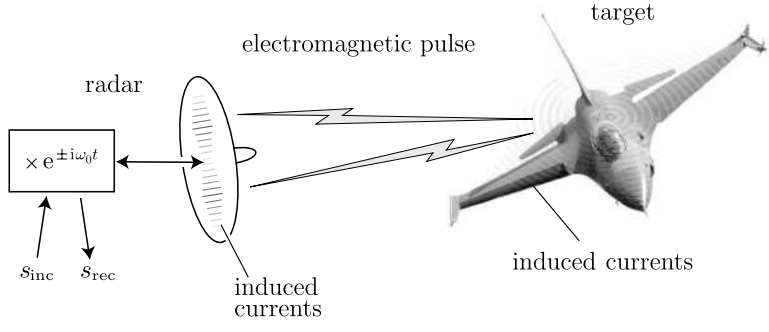

Figure 1.9. *A generic radar detection system.*

becomes the envelope of the more rapidly varying carrier wave. The frequency ω_0 is typically chosen to be in one of the bands in Table 1.1.

The upmodulated signal is then used to excite currents on an antenna that cause an electromagnetic wave to be launched toward the target. (This antenna is usually designed to have some degree of directionality or *gain* (see Chapter 8), and this directionality can also be used to estimate target direction or *bearing*.) The wave is reflected from objects in the environment (see Chapters 3 and 6) and propagates back to the receiver, where the electromagnetic field induces currents on the antenna. By Ohm's law (14), these currents give rise to a time-varying voltage, which is again multiplied by a version of the carrier signal and filtered to remove (*beat down* or *demodulate*) the carrier frequency dependence; finally the demodulated time-varying voltage $s_{\text{rec}}(t)$ is sent to a signal processor (Chapter 4). Note that while the target scattering physics involves RF's (ω_0 is typically in the range from

Table 1.3. *Decibels.*

dB	Power ratio
0 dB	$1 = 10^0$
10 dB	$10 = 10^1$
20 dB	$100 = 10^2$
30 dB	$1000 = 10^3$

$2\pi \times 1$ GHz to $2\pi \times 35$ GHz), the signal processor usually sees much lower *baseband* frequencies, for which $\omega \lesssim 0.1 \times \omega_0$.

1.9 Decibels

Because of the very wide range of power intensities that arise in radar, it is common to use a logarithmic scale for measuring relative power. The number of *Bels* (named for Alexander Graham Bell) that represents the ratio $\left(\frac{\text{power in}}{\text{power out}}\right)$ is defined to be $\log_{10}\left(\frac{\text{power in}}{\text{power out}}\right)$; however it is too small for radar applications, so quantities expressed in Bels have too many zeros at the end. Instead the unit that is commonly used is the *decibel* (dB), which is defined as

$$\boxed{\text{number of dB} = 10\log_{10}\frac{\text{power in}}{\text{power out}}.}$$

Because power is proportional to the square of voltage, the number of dB representing the voltage ratio $\frac{\text{V}_{\text{in}}}{\text{V}_{\text{out}}}$ is $10\log_{10}\frac{V_{in}^2}{V_{out}^2} = 20\log_{10}\frac{V_{in}}{V_{out}}$.

The unit dBW is an absolute unit referenced to one watt; dBm (or dBmW) is referenced to one milliwatt.

Chapter 2

Radar Systems

There are two main designs for radar systems, namely, stepped-frequency and pulsed.

2.1 Stepped-Frequency Systems

The systems that are easiest to understand are stepped-frequency radars. Most laboratory systems are of this type, and there are a few fielded stepped-frequency systems as well. Figure 2.1 shows an example of an indoor test range.

Stepped-frequency systems consist of one or more antennas and a network analyzer, which is an electronic instrument capable of creating a signal at its output port and measuring a corresponding received signal at its input port. (See Figure 2.1.) The network analyzer creates a waveform of the form $\cos(\omega_1 t)$ that appears as a voltage on the output port. The output port is connected to an antenna, which radiates electromagnetic waves that scatter back and induce time-varying voltages on the antenna connected to the input port of the network analyzer. If the environment is stationary, these voltages at the input port are of the form $A_1 \cos(\omega_1 t) + B_1 \sin(\omega_1 t)$; the system records A_1 and B_1.

Next, the network analyzer creates a waveform of the form $\cos(\omega_2 t)$, and records the corresponding A_2 and B_2. This process is repeated for a sequence of angular frequencies $\omega_1, \omega_2, \ldots, \omega_N$ (see Table 2.1).

The mathematical analysis is aided by the observation that $\cos(\omega_j t)$ can be written as $\mathrm{Re}\exp(-i\omega_j t)$, where Re denotes the real part; writing $R = R_R + iR_I$, we have

$$\begin{aligned}\mathrm{Re}\,[R(\omega)\exp(-i\omega t)] &= \mathrm{Re}\,[(R_R(\omega) + iR_I(\omega))\,(\cos(\omega t) - i\sin(\omega t))] \\ &= R_R(\omega)\cos(\omega t) + R_I(\omega)\sin(\omega t). \end{aligned} \tag{2.1}$$

Consequently, we see that recording the real-valued coefficients A_j and B_j is equivalent to recording the complex *reflection coefficient* $R(\omega_j)$.

From knowledge of the Rs, we can synthesize the (approximate) response to *any* transmitted waveform s whose Fourier transform is supported in the frequency range $[\omega_1, \omega_N]$. To do this, first we use the Fourier transform (1) to determine how to decompose s into complex exponentials:

$$s(t) = \sum a_n e^{-i\omega_n t} \approx \int_{\omega_1}^{\omega_N} a(\omega) e^{-i\omega t} d\omega, \tag{2.2}$$

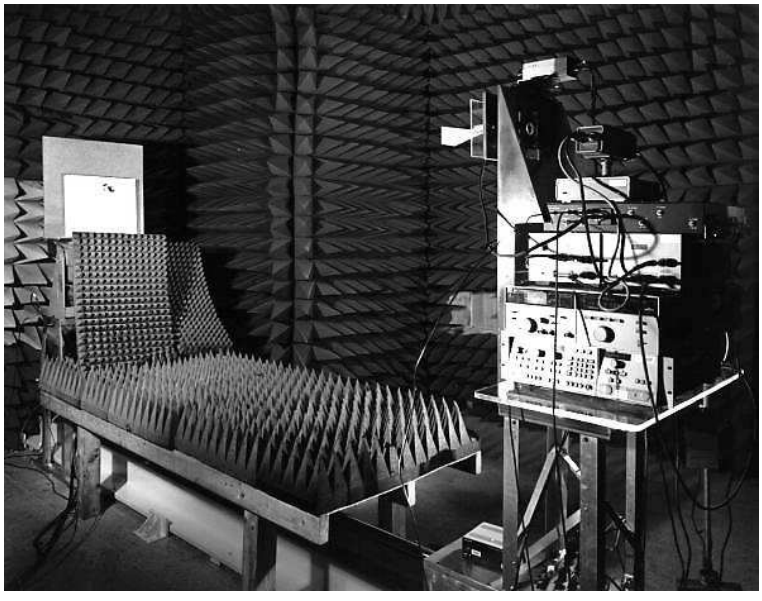

Figure 2.1. *An indoor test range with a stepped-frequency radar system and a horn antenna. The pyramids consist of radar-absorbing material (courtesy of NASA Glenn Research Center).*

Table 2.1. *Data from a stepped-frequency radar system.*

Transmit	Receive	Record
$\underbrace{\cos(\omega_1 t)}_{\mathrm{Re}(e^{-i\omega_1 t})}$	$\underbrace{R_R(\omega_1)\cos(\omega_1 t) + R_I(\omega_1)\sin(\omega_1 t)}_{\mathrm{Re}[R(\omega_1)e^{-i\omega_1 t}]}$	$R(\omega_1)$
$\mathrm{Re}\ (e^{-i\omega_2 t})$	$\mathrm{Re}[R(\omega_2)e^{-i\omega_2 t}]$	$R(\omega_2)$
$\vdots$	$\vdots$	$\vdots$
$\mathrm{Re}(e^{-i\omega_N t})$	$\mathrm{Re}[R(\omega_N)e^{-i\omega_N t}]$	$R(\omega_N)$

where $a_n \approx a(\omega_n)$, and then we use the coefficients a_n and the measurements $R(\omega_n)$ to determine the corresponding response s_{rec}:

$$s_{\mathrm{rec}}(t) = \sum a_n R(\omega_n) e^{-i\omega_n t} \approx \int_{\omega_1}^{\omega_N} a(\omega) R(\omega) e^{-i\omega t} d\omega. \tag{2.3}$$

Here we are using the linearity of the map from incident waves to scattered waves.

2.2 Pulsed Systems

Most fielded systems, on the other hand, are pulsed systems.

A block diagram of a typical pulsed radar system can be seen in Figure 2.2. We begin with the waveform generator at the top left. The waveform (pulse) $s(t)$ is mixed with (i.e., multiplied by) a *carrier waveform* at the angular frequency ω_0. The resulting product, the *modulated signal* $p(t) = s(t)\cos(\omega_0 t) = Re\left(s(t)e^{-i\omega_0 t}\right)$ is then amplified by the transmitter. The peak power of the transmitted waveform is typically on the order of megawatts with average power in kilowatts. Common pulse widths are in the microsecond range with hundreds of pulses transmitted per second.

The modulated signal p passes through a *duplexer*, which is a switching device that prevents the high-power transmitted wave from entering into the very sensitive receiver side of the system. The waveform p excites currents on the antenna, which radiate electromagnetic waves into the environment. We defer a discussion of wave propagation and scattering to the next chapter. For now, we note simply that scattered waves return, and again excite currents on the antenna, which produces voltages of the form

$$p_{\text{rec}}(t) = a(t)\cos(\phi(t) + \omega_0 t). \tag{2.4}$$

These voltages are typically extremely small, often smaller than the voltages due to thermal noise in the radar system itself. They are passed through a low-noise amplifier (LNA), and then on to the *I/Q demodulator*.

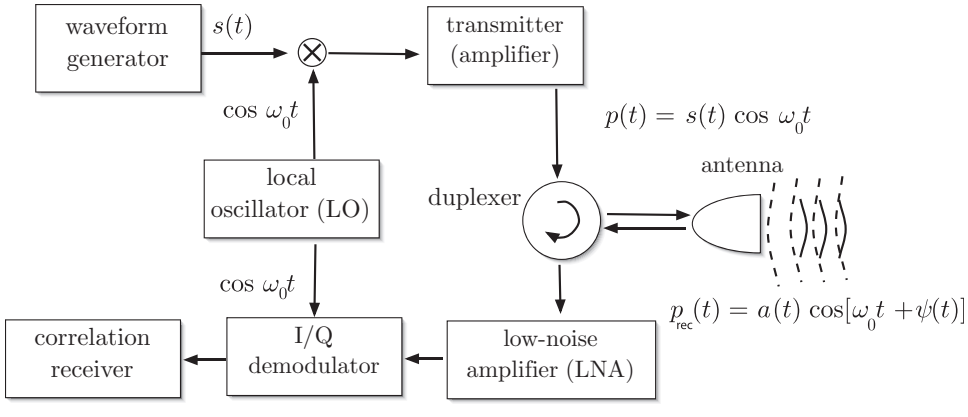

Figure 2.2. *A system diagram for a typical pulsed radar system.*

2.2.1 I/Q Demodulation and the Analytic Signal

Real-valued system signals, when Fourier transformed, involve both positive and negative frequencies; however, the values at the negative frequencies are the complex conjugates of those at the positive frequencies. Thus the negative frequencies provide no new information. Consequently, it is conventional to convert the signal to one that has only positive frequencies; by the Paley–Wiener theorem (see the Preface), the resulting signal is analytic in the upper half-plane in t. This signal is called the *analytic signal*.

The process of converting a real-valued signal to a complex-valued one that is analytic in the upper half-plane can be carried out approximately by a process called *I/Q demodulation*, which is described below. This process provides a good approximation [37] to the analytic signal when the signal is *narrowband*, i.e., has a bandwidth much smaller than its carrier frequency.

Conveniently, this approximation can be implemented in hardware (in a process known as *heterodyne reception*); if $p_{\text{rec}}(t) = a(t)\cos(\phi(t) + \omega_0 t)$ is the (real-valued) voltage output from the receiving antenna, then the *in-phase* I and *quadrature* Q components of $s_{\text{rec}}(t)$ are respectively found by mixing, phase-shifting, and low-pass filtering; more details follow below.

More specifically, I/Q demodulation or heterodyne reception involves splitting the incoming signal into two identical copies, mixing (multiplying) one copy by an in-phase (I) version of the carrier, mixing the other copy by a 90° out-of-phase (phase-shifted) or quadrature (Q) version, and then low-pass filtering both results. Low-pass filtering is simply convolving with a smooth function in order to get rid of rapdily oscillating components of a function; this is discussed in section 2.2.2 below.

The in-phase (I) channel results in

$$\begin{aligned} I(t) &= F_{LP}\, p_{\text{rec}}(t)\cos(\omega_0 t) \qquad (2.5)\\ &= F_{LP} a(t)\cos(\phi(t)+\omega_0 t)\cos(\omega_0 t) = F_{LP} a(t)\frac{1}{2}\Bigg(\underbrace{\cos(\phi(t)+2\omega_0 t)}_{\text{filter out}} + \cos\phi(t)\Bigg), \end{aligned}$$

where we have used the angle-adddition formula for the cosine and where F_{LP} denotes a low-pass filter.

The out-of-phase or *quadrature* (Q) channel results in

$$\begin{aligned} Q(t) &= F_{LP}\, p_{\text{rec}}(t)\sin(\omega_0 t) \qquad (2.6)\\ &= F_{LP} a(t)\cos(\phi(t)+\omega_0 t)\sin(\omega_0 t) = F_{LP} a(t)\frac{1}{2}\Bigg(\underbrace{-\sin(\phi(t)+2\omega_0 t)}_{\text{filter out}} + \sin\phi(t)\Bigg), \end{aligned}$$

where we have used the angle-addition formula for the sine.

2.2.2 Filters

Filters are needed above to eliminate the high-frequency terms in (2.5) and (2.6). Filters are simply convolutions, or multiplication operators in the Fourier transform domain. The following diagram shows the procedure for applying a filter.

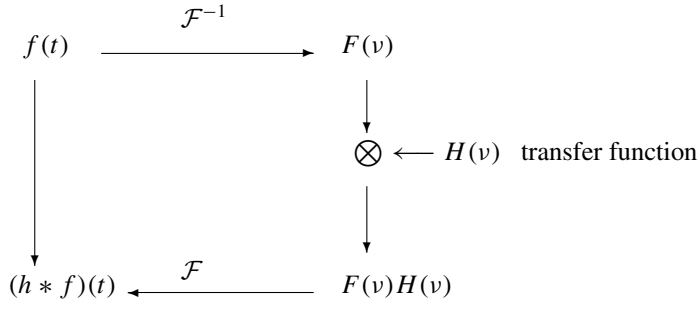

Here $\mathcal{F}$ denotes the Fourier transform (1). In other words, to apply a filter, we inverse Fourier transform, multiply by the transfer function H, and then Fourier transform. If we interchange the order of integration, we see that this is equivalent to convolving with the inverse Fourier transform h of H:

$$\begin{aligned}\mathcal{F}^{-1}\left[H(\nu)(\mathcal{F}f)(\nu)\right](t) &= \int e^{-2\pi i\nu t} H(\nu) \int e^{2\pi i\nu t'} f(t')dt'd\nu \\ &= \int \underbrace{\left[\int e^{-2\pi i\nu(t-t')} H(\nu)d\nu\right]}_{h(t-t')} f(t')dt'. \end{aligned} \tag{2.7}$$

The function h is called the *impulse response* of the filter.

Example: Low-pass filter. For a low-pass filter, we take

$$H_b(\nu) = \begin{cases} 1, & |\nu| < b, \\ 0 & \text{otherwise.} \end{cases} \tag{2.8}$$

This corresponds to convolution with the impulse-response function

$$h(t) = \frac{b}{\pi}\frac{\sin bt}{bt} = \frac{b}{\pi}\operatorname{sinc} bt. \tag{2.9}$$

Applied to $f(t)$, this low-pass kernel will eliminate any Fourier components of $F(\nu)$ that fall outside of the "band" $(-b, b)$.

Example: High-pass filter. For a high-pass filter, we take

$$H_b(\nu) = \begin{cases} 0, & |\nu| < b, \\ 1 & \text{otherwise.} \end{cases} \tag{2.10}$$

Example: Riesz potential. The one-dimensional *Riesz potential* [87, 89, 121] is defined in terms of the transfer function

$$H_\alpha(\nu) = |\nu|^{-\alpha}, \tag{2.11}$$

so that the one-dimensional Riesz potential $\mathcal{I}^\alpha f$ associated with f is

$$\mathcal{I}^\alpha f = \mathcal{F}^{-1}\left[|\nu|^{-\alpha}\mathcal{F}f\right]. \tag{2.12}$$

This filter is used in X-ray tomography [87, 89]. For $\alpha = -1$, it is often approximated by the *Ram–Lak* filter, for which the transfer function is a low-pass version of (2.11):

$$H_b(\nu) = \begin{cases} |\nu| & \text{for } |\nu| < b, \\ 0 & \text{otherwise.} \end{cases} \tag{2.13}$$

2.2.3 The Quadrature Model

The I and Q channels together give the *quadrature model* [37] for the radar signal

$$\boxed{s_{rec}(t) = a(t)e^{-i\phi(t)}.}$$

Within the radar literature, this model is so pervasive that the term "quadrature" is often dropped. The function $a(t)$ is known as the *envelope* and $\phi(t)$ is the *phase modulation.*

Conditions under which the quadrature signal model is approximately analytic in the upper half-plane are discussed in [37]. We consider only conventional radar systems for which these conditions are satisfied, and consequently we use the terms "analytic signal" and "quadrature model" interchangeably.

In Chapter 3 we show explicitly how solutions of the wave equation are converted to a quadrature signal model; in subsequent chapters, we simply assume an analytic signal.

Chapter 3

Introduction to Scattering

We now turn our attention to the rightmost part of Figure 2.2, namely, the propagation and scattering of electromagnetic waves. We begin our study of wave propagation with a simple one-dimensional model that we can solve exactly. The solution to this simple model exhibits certain important features that are common to many radar scattering problems.

3.1 One-Dimensional Scattering from a Fixed PEC Plate

We consider an antenna at position $x = 0$, and an infinite metal (perfectly electrically conducting or *PEC*) plate at position $x = R$.

We assume that the waveform generator produces a waveform $s(t)$, which is then mixed with the carrier wave to produce $f(t) = s(t)\cos(\omega_0 t)$. For a one-dimensional problem, we take the transmitted wave to be

$$\boldsymbol{\mathcal{E}}^{\text{in}}(t, \boldsymbol{x}) = \boldsymbol{E}^{\text{in}} f(t - x/c), \tag{3.1}$$

where $\boldsymbol{E}^{\text{in}}$ is perpendicular to the x direction (see (1.8)). This transmitted field satisfies (1.7).

The total electric field consists of both the transmitted wave and the wave scattered from the plate:

$$\boldsymbol{\mathcal{E}}^{\text{tot}} = \boldsymbol{\mathcal{E}}^{\text{in}} + \boldsymbol{\mathcal{E}}^{\text{sc}}. \tag{3.2}$$

The total electric field satisfies (1.7) together with the boundary condition on the perfectly conducting plate:

$$\boldsymbol{\mathcal{E}}^{\text{tot}}_{\text{tan}}\Big|_{x=R} = 0, \tag{3.3}$$

where the subscript tan denotes the components of the field tangential to the conducting plate. Since $\boldsymbol{\mathcal{E}}^{\text{tot}}$ and $\boldsymbol{\mathcal{E}}^{\text{in}}$ both satisfy (1.7), from (3.2) we discover that the scattered field $\boldsymbol{\mathcal{E}}^{\text{sc}}$ also satisfies (1.7), and using (3.2) in (3.3), we find that $\boldsymbol{\mathcal{E}}^{\text{sc}}$ satisfies the boundary condition

$$\boldsymbol{\mathcal{E}}^{\text{sc}}\Big|_{x=R} = -\boldsymbol{\mathcal{E}}^{\text{in}}\Big|_{x=R}. \tag{3.4}$$

We expect that the scattered field will consist of a left-travelling wave and will thus be of the form $\boldsymbol{\mathcal{E}}^{\rm sc}(t,\boldsymbol{x}) = \boldsymbol{E}^{\rm sc} g(t + x/c)$. To determine $\boldsymbol{\mathcal{E}}^{\rm sc}$ and g, we use (3.4):

$$\boldsymbol{E}^{\rm sc} g(t + R/c) = -\boldsymbol{E}^{\rm in} f(t - R/c). \tag{3.5}$$

Thus we obtain a solution by taking $\boldsymbol{E}^{\rm sc} = -\boldsymbol{E}^{\rm in}$ and $g(u) = f(u - 2R/c)$, where we have simply made the substitution $u = t + R/c$ for the argument of g and used $t = u - R/c$ in the argument of f. Thus we find that the scattered field is $\boldsymbol{\mathcal{E}}^{\rm sc}(t,\boldsymbol{x}) = -\boldsymbol{E}^{\rm in} f(t - x/c - 2R/c)$. Evaluating this field at the antenna position $x = 0$, we find that $\boldsymbol{\mathcal{E}}^{\rm sc}(t, x = 0) = -\boldsymbol{E}^{\rm in} f(t - 2R/c)$. Consequently the received signal is

$$p_{\rm rec}(t) = f(t - 2R/c) = s(t - 2R/c)\cos[\omega_0(t - 2R/c)].$$

I/Q demodulation of the received signal. The in-phase and quadrature components of the received signal are found as in (2.5) and (2.6), where $a(t) = s(t - 2R/c)$ and $\phi(t) = -2\omega_0 R/c$. Consequently the analytic signal is $s(t-2R/c)e^{2i\omega_0 R/c}$. The exponential factor is independent of t and contributes only an overall phase. This phase can be used to extract the velocity of a moving target, as we will see in Chapter 5.

3.2 One-Dimensional Scattering from a Moving PEC Plate

Here we consider the same problem but with a moving plate. We assume that the position of the plate is $x = R(t)$. The analysis is the same as that for the fixed plate up to the point of the boundary condition (3.5), which in this case becomes

$$\boldsymbol{E}^{sc} g(t + R(t)/c) = -\boldsymbol{E}^{\rm in} f(t - R(t)/c).$$

We again use the substitution $u = t + R(t)/c$, but this time we cannot solve explicitly for t unless we know the motion of the plate. We assume for simplicity that it is undergoing linear motion,[2] so that $R(t) = R + vt$. The rate v at which the range changes is called the *range-rate*. In this case, we can solve for t in terms of u:

$$t = \frac{u - R/c}{1 + v/c}.$$

Inserting this expression for t into $g(u) = f(u - 2R/c)$, we obtain

$$g(u) = f\left(\alpha(u - R/c) - R/c\right),$$

where the *Doppler scale factor* α is

$$\alpha = \frac{1 - v/c}{1 + v/c}. \tag{3.6}$$

[2]Even if the motion is not linear, the linear expression $R(t) = R + vt$ can be considered to be the first two terms in a Taylor expansion that is valid for small t (i.e., for short pulses), where the origin of time is chosen to be at a time when the pulse is interacting with the target center.

Thus we find that the scattered field is $\boldsymbol{\mathcal{E}}^{\rm sc}(t,\boldsymbol{x}) = -\boldsymbol{E}^{\rm in} f[\alpha(t + x/c - R/c) - R/c]$. At the antenna at $x = 0$, this is

$$\boldsymbol{\mathcal{E}}^{\rm sc}(t, x = 0) = -\boldsymbol{E}^{\rm in} f[\alpha(t - R/c) - R/c].$$

Recalling that the transmitted waveform is $f(t) = s(t)\cos(\omega_0 t)$, we obtain the scattered signal at the antenna:

$$p_{\rm rec}(t) = f[\alpha(t - R/c) - R/c] = s[\alpha(t - R/c) - R/c]\cos[\omega_0(\alpha(t - R/c) - R/c)].$$

From the coefficient of t in the argument of the cosine, we see that the scatterer's motion has resulted in a change in the carrier frequency, from ω_0 to $\alpha\omega_0$.

For a scatterer moving slowly, so that v/c is small, we can expand the denominator of (3.6) in a geometric series to obtain

$$\alpha = (1 - v/c)\left(1 - v/c + \mathcal{O}[(v/c)^2]\right) = 1 - 2v/c + \mathcal{O}[(v/c)^2]$$

and consequently use the approximation

$$p_{\rm rec}(t) \approx s[t - 2R/c]\cos\left(\omega_0[(1 - 2v/c)(t - R/c) - R/c]\right), \tag{3.7}$$

where we have also used the fact that s is slowly varying to replace the argument $\alpha(t - R/c) - R/c$ by $t - 2R/c$. From looking at the coefficient of t in the argument of the cosine function, we see that the carrier frequency has been shifted (relative to the transmitted carrier frequency) by an amount

$$\omega_D = -\frac{2v}{c}\omega_0. \tag{3.8}$$

This is the (angular) *Doppler shift*. If the target moves away from the antenna ($v > 0$), then the Doppler shift is negative; if the target moves toward the antenna ($v < 0$), then the shift is positive. (See Figure 3.1.)

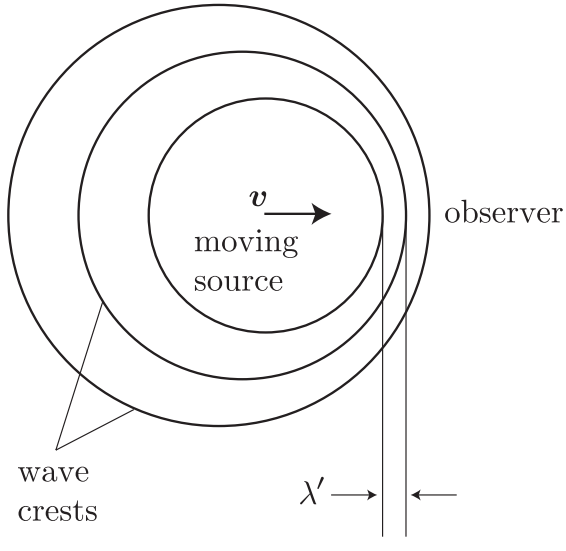

Figure 3.1. *An object moving with velocity v toward the observer and transmitting a signal with wavelength λ will appear to be transmitting a signal of shorter wavelength λ'.*

I/Q demodulation of the received signal. We note that (3.7) can be put into the form (2.4) with $a(t) = s(t - 2R/c)$ and $\phi(t) = \omega_D(t - R/c) - 2\omega_0 R/c$. Consequently the analytic signal is

$$\boxed{s(t - 2R/c)e^{-i\omega_D(t-R/c)}e^{2i\omega_0 R/c}.} \tag{3.9}$$

In summary, *the received signal is a time-delayed, Doppler-shifted version of the transmitted signal*.

Chapter 4

Detection of Signals in Noise

We have found that for one-dimensional scattering from a fixed plate (section 3.1), the signal that returns to the radar is a time-delayed version of the transmitted signal. As we will see in Chapter 6, this is also the case for three-dimensional scattering from a fixed, point-like target.

In order to obtain a good estimate of the target range, we would like to use a short pulse. Unfortunately, a short pulse has little energy, and it is therefore difficult to detect in noise. We will see in Chapter 6 that spherical waves emanating from a small source, such as an antenna, decay like $1/R$. This means that the power decays like $1/R^2$. These waves scatter, and again for a small target, the scattered field behaves like a spherical wave emanating from the scatterer; the power of this spherical wave undergoes decay of another factor of $1/R^2$. Consequently the power of the signal received by the antenna has decayed by a factor of $1/R^4$ relative to the signal that was transmitted. For distances on the order of 20 or 30 km, which are typically needed for tracking airborne objects, the received power can be as low as 10^{-18} Watts and is swamped by the power of the thermal noise in the receiver. This means that we may not even be able to detect the target, much less form an image of it.

Fortunately, a brilliant mathematical solution to this problem was invented by D.O. North [94] in 1943. The solution involves transmitting long *coded* pulses, together with appropriate mathematical processing called *matched filtering* or *correlation reception*. The resulting technique is called *pulse compression*. This chapter will briefly explain the methods employed.

We consider first scattering from an isolated, point-like target that is fixed.

4.1 Detection of Signals Scattered from Fixed Targets

The signal scattered from a fixed, point-like target is simply a time-delayed version of the transmitted waveform:

$$s_{\text{rec}}(t) = \rho s(t - \tau) + n(t),$$

where τ corresponds to the $2R/c$ delay we found in the last chapter, where ρ is the scattering strength (which for a small target is proportional to $1/R^4$), and where n denotes noise.

We would like to apply a filter to s_{rec} in order to improve the signal-to-noise ratio (SNR). We denote the filter's impulse response (convolution kernel) by h and write for the filter output

$$\eta(t) = (h * s_{\text{rec}})(t) = \rho\eta_s(t) + \eta_n(t), \tag{4.1}$$

where

$$\eta_s(t) = \int h(t-t')s(t'-\tau)\,dt' \qquad \text{and} \qquad \eta_n(t) = \int h(t-t')n(t')\,dt'.$$

We would like the signal output $\eta_s(\tau)$ at time τ to be as large as possible relative to the noise output $\eta_n(\tau)$.

We model the noise as a random process. Thermal noise in the receiver is well modeled by white noise, which means that $E[n(t)n^*(t')] = N\delta(t-t')$, where E denotes expected value and where N is a constant corresponding to the noise power. Since the noise is random, so is η_n. Thus the SNR we would like to maximize is

$$\text{SNR} = \frac{|\eta_s(\tau)|^2}{E|\eta_n(\tau)|^2}. \tag{4.2}$$

First we compute the denominator of (4.2):

$$\begin{aligned} E|\eta_n(\tau)|^2 &= E\left|\int h(\tau-t')n(t')\,dt'\right|^2 = E\int h(\tau-t')n(t')dt'\left(\int h(\tau-t'')n(t'')dt''\right)^* \\ &= \iint h(\tau-t')h^*(\tau-t'')\underbrace{E[n(t')n^*(t'')]}_{N\delta(t'-t'')}\,dt'\,dt'' \\ &= N\int \left|h(\tau-t')\right|^2 dt' = N\int |h(t)|^2\,dt, \end{aligned}$$

where in the last line we have made the change of variables $t = \tau - t'$ and where $*$ denotes complex conjugation. Thus (4.2) becomes

$$\text{SNR} = \frac{\left|\int h(\tau-t')s(t'-\tau)\,dt'\right|^2}{N\int |h(t)|^2\,dt} = \frac{\left|\int h(t)s(-t)\,dt\right|^2}{N\int |h(t)|^2\,dt}, \tag{4.3}$$

where in the numerator we have made the change of variables $t = \tau - t'$. To the numerator of (4.3), we can apply the Cauchy–Schwarz theorem (13) to conclude that the numerator, and therefore the quotient (4.3), is maximized when h is chosen so that

$$\boxed{h(t) = s^*(-t).}$$

This is the *matched filter*. Thus to obtain the best SNR, we should convolve the received signal with the time-reversed, complex-conjugated version of the signal we expect to see.

With this choice, the filter (4.1) can be written

$$\eta(t) = \int h(t-t'')s_{\text{rec}}(t'')\,dt'' = \int s^*(t''-t)s_{\text{rec}}(t'')\,dt'' = \int s^*(t')s_{\text{rec}}(t'+t)\,dt', \tag{4.4}$$

which is a *correlation* between s and s_{rec}. If $s = s_{\text{rec}}$, (4.4) is called an *autocorrelation*.

Matched filtering improves SNR at the receiver by concentrating the energy of the received signal at a single delay time. This process results in *pulse compression*, a phenomenon which is most easily explained by some examples.

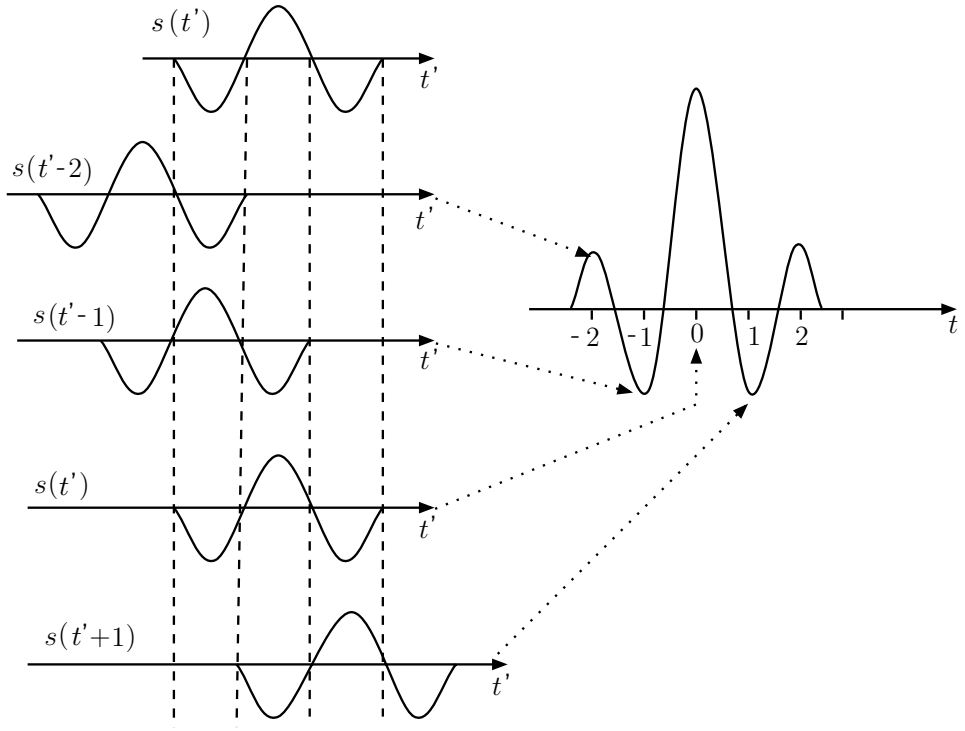

Figure 4.1. *Pulse compression. The signal at the top represents the transmitted waveform. The lower graphs represent the received signal for different shifts, according to the rightmost expression of (4.4). When a signal shifted by t is multiplied by the waveform at the top and the product is integrated over t', the resulting number is plotted at position t on the graph to the right.*

4.1.1 Pulse Compression

Figure 4.1 shows an example of the (auto)correlation process. In this case both signals are real-valued, so the complex conjugation appearing in (4.4) has no effect. Note that although the output signal has a longer time duration than the original signal s, its energy is more concentrated about the center.

It is a consequence of the Cauchy–Schwarz inequality (13) that the highest peak occurs when the signals are not shifted relative to each other. The smaller peaks, called *sidelobes*, are undesirable, and an open problem is to design pulses whose autocorrelations have the lowest and fewest sidelobes.

4.1.2 Phase Coding

A radar system makes the most efficient use of power when it transmits a constant-amplitude waveform. Consequently, most radar waveforms are designed with variations only in the

phase of the signal. A constant-amplitude signal of duration T can be written as a multiple of the characteristic function $u_{[0,T]}(t)$ that is 1 in the interval $[0, T]$ and 0 otherwise:

$$s(t) = e^{i\phi(t)} u_{[0,T]}(t). \tag{4.5}$$

The *instantaneous (angular) frequency* [79] is defined to be the quantity $d\phi/dt$. Note that, unlike the notion of frequency, the instantaneous frequency is *not* defined in terms of the Fourier transform.

Chirps

The most commonly used radar waveform is the *chirp*. A chirp is a constant-amplitude signal whose instantanous frequency varies linearly with time; chirps are therefore also called *linearly frequency modulated* (LFM) waveforms. Linear variation of the instantaneous frequency implies that $d\phi/dt = \omega_{\min} + \gamma t$, which in turn implies that $\phi(t) = \omega_{\min} t + \gamma t^2/2$. The coefficient γ is called the (angular) *chirp rate* or *chirp slope*.

A chirp is thus of the form

$$p(t) = e^{i(\omega_{\min} t + \gamma t^2/2)} u_{[0,T]}(t). \tag{4.6}$$

A chirp with positive chirp slope is called an *upchirp*; one with a negative chirp slope is a *downchirp*. An example of an upchirp is shown in Figure 4.2.

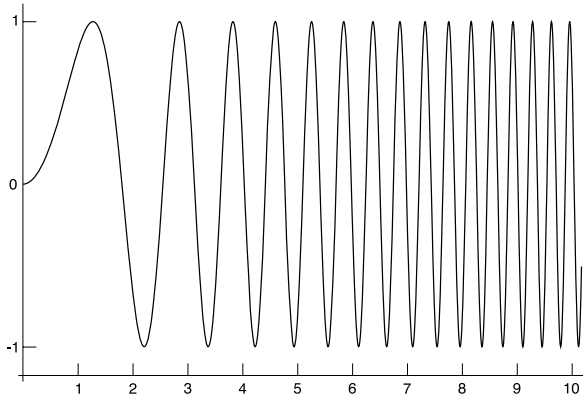

Figure 4.2. *A baseband chirp. Here the horizontal axis is time and the vertical axis is the real part of the signal $p(t)$ (4.6) with $\omega_{\min} = 0$.*

The instantaneous (angular) frequency of the chirp (4.6) varies from $\omega_{\min}$ to $\omega_{\max} = \omega_{\min} + \gamma T$, with a center frequency of $\omega_0 = (\omega_{\min} + \omega_{\max})/2 = \omega_{\min} + \gamma T/2$. Thus the instantaneous frequency of the chirp varies over the interval $[\omega_0 - T\gamma/2, \omega_0 + T\gamma/2]$.

The *power spectrum* (i.e., square of the magnitude of the Fourier transform) of a chirp can be seen in Figure 4.3. We see that the spectrum of a chirp is roughly constant over the frequency band $[\omega_0 - T\gamma/2, \omega_0 + T\gamma/2]$, which is the same range over which the instantanous angular frequency varies as t ranges from 0 to T. Thus the angular frequency

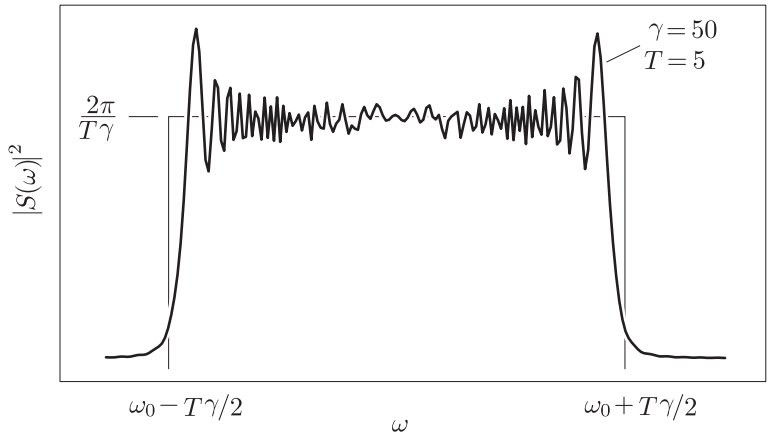

Figure 4.3. *The power spectrum of a chirp.*

bandwidth $T\gamma$ can be estimated by looking at the range of instantaneous frequencies. The bandwidth in Hertz is $2\pi T\gamma$.

A straightforward calculation shows that the autocorrelation of the normalized chirp $s(t) = T^{-1/2}u_{[0,T]}(t)\exp(i\gamma t^2)$ is

$$\chi(\tau) = \begin{cases} e^{-i\tau T\gamma/2}\text{sinc}\,[(T - |\tau|)\gamma\tau/2], & |\tau| \le T, \\ 0, & |\tau| > T, \end{cases}$$

where the sinc function[3] is defined as (see Figure 4.4)

$$\text{sinc}\, x = \frac{\sin x}{x}. \tag{4.7}$$

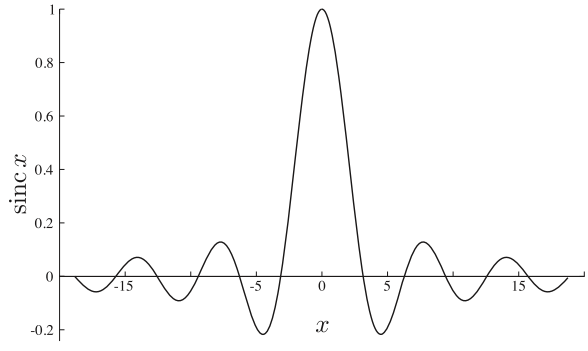

Figure 4.4. *The sinc function.*

[3]There are also different conventions, differing by factors of π, for the definition of the sinc function.

Chirps are very commonly used in radar imaging. Pulse compression for chirps has the following intuitive interpretation: When the pulse is transmitted, different parts of the pulse are coded with different instantaneous frequencies. In the pulse compression process, the different frequencies are delayed by different amounts of time, so that all the energy emerges at the same time. In fact, pulse compression for chirps can be carried out by an analog component called a surface acoustic wave (SAW) device, which delays different frequencies by different amounts of time.

Digital pulse coding

Another approach to obtaining a constant-amplitude waveform with a good autocorrelation function is to use a coded digital signal. Digital signals can be converted into radar waveforms by associating bit symbols with a phase shift. *Binary pulse codes*, for example, are sequences consisting only of zeros and ones, say, or pluses and minuses. They can be coded onto a waveform by associating the plus symbol with a 0° phase shift and the minus symbol with a 180° shift. This is illustrated in Figure 4.5.

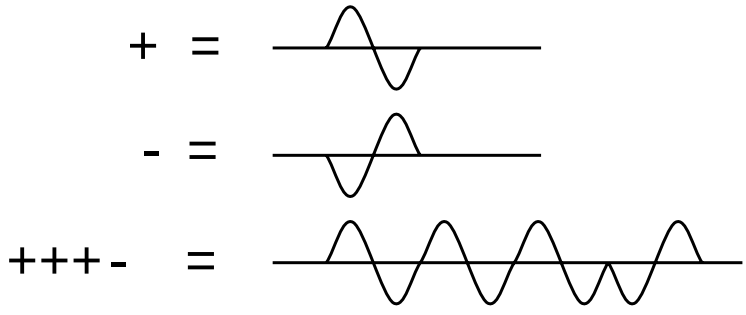

Figure 4.5. *Implementation of binary sequences as RF waveforms.*

An alphabet of size n leads to a *polyphase code*, in which each symbol is associated with a different phase shift. One example of an n-element polyphase code is the *n-phase code* that uses phase shifts that are multiples of $2\pi/n$ radians or $360°/n$. Thus, for example, a 3-phase code uses the phase shifts of 0, $2\pi/3$, and $4\pi/3$.

4.2 High-Range-Resolution Imaging

If multiple objects (targets) are present in our field of view, we can hope to form an image that shows their relative positions. The presence of multiple targets, however, can involve *multiple scattering*, in which waves bounce back and forth between the targets. Multiple scattering can be extremely complex and for this reason is typically neglected in radar imaging. In this discussion we follow the standard approach of ignoring multiple scattering. We use the term *noninteracting* targets to refer to objects for which multiple scattering can be neglected.

4.2.1 Two Point-Like Targets

The signal received from two fixed and noninteracting point-like targets is

$$s_{\text{rec}}(t) = \rho_1 s(t - \tau_1) + \rho_2 s(t - \tau_2) + n(t).$$

Application of a matched filter results in a sum of outputs from each individual target.

4.2.2 A Distribution of Fixed Targets

The signal received from a distribution of noninteracting targets is

$$s_{\text{rec}}(t) = \int \rho(\tau') s(t - \tau') d\tau' + n(t).$$

Application of a matched filter results in

$$\begin{aligned} \eta(t) &= \int s^*(t' - t) s_{\text{rec}}(t')\, dt' = \int s^*(t' - t) \int \rho(\tau') s(t' - \tau')\, d\tau'\, dt' + \text{noise term} \\ &= \int \int s^*(t' - t) s(t' - \tau')\, dt' \rho(\tau')\, d\tau' + \text{ noise term.} \end{aligned} \tag{4.8}$$

In the last line of (4.8), we make the substitution $t'' = t' - \tau'$. The result can be written

$$\eta(t) = \int \chi(t - \tau') \rho(\tau')\, d\tau', \tag{4.9}$$

where χ is the autocorrelation

$$\chi(t) = \int s^*(t'' - t) s(t'')\, dt'' = \int s^*(t') s(t + t')\, dt'.$$

The left side of (4.8) can be considered a one-dimensional image (see Figure 1.3), and (4.9) shows how the true distribution ρ is related to the image η. The image is the convolution of ρ with χ, which is called the *point-spread function* (PSF). The PSF obtains its name from the fact that if ρ consists of a single point $\delta(t)$, then the image is $\eta(t) = \int \chi(t - t')\delta(t')\, dt' = \chi(t)$. Thus χ quantifies the degree to which a single point appears spread out in the image.

In order to form an image with good resolution, we choose a waveform s for which χ is delta-like. This is the basis of *high-range-resolution (HRR)* imaging.

4.3 Detection of Signals Scattered from Moving Targets

We now consider processing of signals scattered from moving targets. In this case, we can hope to form an image that shows both range and velocity of the targets. An example of such a *range-Doppler* image is shown in Figure 4.6.

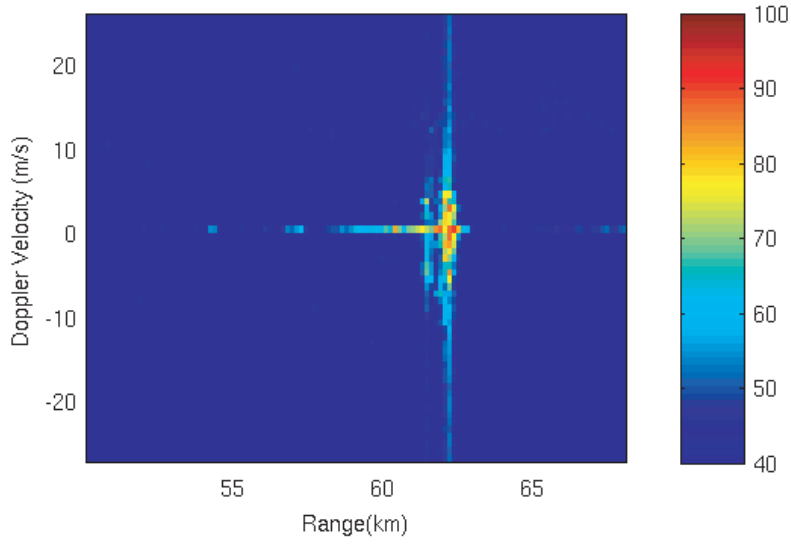

Figure 4.6. *An example of a range-Doppler image from the CSU-CHILL weather radar system. The horizontal streak in the middle of the image corresponds to objects on the ground that are not moving and therefore give rise to no Doppler shift. The vertical streak in the middle is from a wind turbine, whose blades move with a variety of speeds relative to the radar (courtesy of CSU-CHILL; the work was supported by Colorado State University and by the National Science Foundation).*

4.3.1 A Single Moving Point-Like Target

We recall from (3.9) that the signal due to a moving target is a time-delayed, Doppler-shifted version of the transmitted signal. Thus, up to an overall constant phase, we can write the signal from a single point-like moving target as

$$s_{\text{rec}}(t) = \rho s(t-\tau)e^{-i\omega_D(t-\tau)} + n(t).$$

Now we have two unknown parameters to estimate, namely, the delay τ and the Doppler shift ω_D. Instead of applying a single matched filter, we now use a set of matched filters, one for every possible Doppler shift:

$$\eta(\tau, \nu) = \int h_\nu(t-t')s_{\text{rec}}(t')\,dt' = \rho \int h_\nu(t-t')s(t'-\tau)e^{-i\omega_D(t'-\tau)}\,dt' + \text{ noise term.}$$

Such a set of filters is called a *filter bank*.

The same argument as before shows that the best filter is the matched filter, whose impulse response is

$$h_\nu(t) = s^*(-t)e^{-i\omega_D t}$$

with $\omega_D = 2\pi\nu_D$. For the matched filter, the receiver output is

$$\eta(\tau, \nu) = \rho \int s^*(-t + t')e^{-i\omega(t-t')}s(t' - \tau)e^{-i\omega_D(t'-\tau)}\,dt' + \text{noise term}. \tag{4.10}$$

In order to estimate τ and ν_D, we find the arguments τ and ν where $|\eta|$ takes on its maximum.

4.3.2 Two Moving Point-Like Targets

The signal from two noninteracting moving targets can be written

$$s_{\text{rec}}(t) = \rho_1 s(t - \tau_1)e^{-i\omega_1(t-\tau_1)} + \rho_2 s(t - \tau_2)e^{-i\omega_2(t-\tau_2)} + n(t).$$

Applying a filter bank to this signal results in a sum of terms of the form (4.10), one for each target.

4.3.3 A Distribution of Moving Targets

The signal from a distribution of noninteracting moving targets can be written

$$s_{\text{rec}}(t) = \iint \rho(\tau', \nu')s(t - \tau')e^{2\pi i\nu'(t-\tau')}\,d\tau'\,d\nu',$$

which reduces to the two-target case when $\rho(\tau', \nu') = \rho_1\delta(\tau' - \tau_1)\delta(\nu' - \nu_1) + \rho_2\delta(\tau' - \tau_2)\delta(\nu' - \nu_2)$.

The output from the filter bank is

$$\begin{aligned}
&\eta(\tau, \nu)\\
&\quad= \int s^*(t' - \tau)e^{-2\pi i\nu(\tau-t')}s_{\text{rec}}(t')\,dt'\\
&\quad= \int s^*(t' - \tau)e^{-2\pi i\nu(\tau-t')} \iint \rho(\tau', \nu')s(t' - \tau')e^{-2\pi i\nu'(t'-\tau')}\,d\tau'\,d\nu'\,dt' + \text{ noise term}\\
&\quad= \iiint s^*(t' - \tau)e^{-2\pi i\nu(\tau-t')}s(t' - \tau')e^{-2\pi i\nu'(t'-\tau')}\,dt'\rho(\tau', \nu')\,d\tau'\,d\nu' + \text{ noise term}\\
&\quad= \iiint s^*(t'' + \tau' - \tau)e^{-2\pi i\nu(\tau-t''-\tau')}s(t'')e^{-2\pi i\nu't''}\,dt''\rho(\tau', \nu')\,d\tau'\,d\nu' + \text{ noise term}\\
&\quad= \iint \chi(\tau - \tau', \nu - \nu')e^{-2\pi i\nu'(\tau-\tau')}\rho(\tau', \nu')\,d\tau'\,d\nu' + \text{ noise term},
\end{aligned} \tag{4.11}$$

where we have made the substitution $t' \mapsto t'' = t' - \tau'$ in the third line and where

$$\chi(\tau, \nu) = \int s^*(t'' - \tau)e^{-2\pi i\nu(\tau-t'')}s(t'')\,dt'' = \int s^*(t')s(t' + \tau)e^{2\pi i\nu t'}\,dt' \tag{4.12}$$

is the *radar ambiguity function*, which we study in the next chapter.

The ambiguity function is the PSF for range-Doppler imaging. The fidelity of the range-Doppler imaging process, and consequently the accuracy of target range and velocity estimation, can be found by analysis of the ambiguity function.

Chapter 5

The Radar Ambiguity Function

In this chapter, we study the radar ambiguity function[4] $\chi(\nu, \tau)$, which was defined by (4.12). We note that the ambiguity function, and thus the accuracy with which we can estimate target range and velocity, is determined by the transmitted waveform s. In this chapter we study this relationship.

5.1 Basic Properties

Clearly if we multiply s by a scalar a, then the ambiguity function is multiplied by the scalar a^2. To avoid having to deal with this simple scaling, we consider only signals that are normalized by their total energy: $\int_{-\infty}^{\infty} |s(t')|^2\, dt' = 1$.

Elementary properties of the ambiguity function [38, 126, 76, 110] follow from the definition (4.12):

1. **Relation to signal energy:** It follows from the Cauchy–Schwarz inequality (13) that

$$|\chi(\tau, \nu)| \leq |\chi(0, 0)| = \int_{-\infty}^{\infty} s_{\text{inc}}(t') s_{\text{inc}}^*(t')\, dt' = \text{ total energy in the signal} = 1.$$

2. **Conservation of ambiguity volume:** The total volume under the ambiguity surface

[4] In some literature, the ambiguity function is defined as $|\chi(\nu, \tau)|^2$.

$|\chi(\tau, \nu)|^2$ is

$$\begin{aligned}
&\iint |\chi(\tau,\nu)|^2\,d\tau\,d\nu = \iint \chi(\nu,\tau)\chi^*(\nu,\tau)\,d\tau\,d\nu \\
&= \iint\int s^*(t')s(t'+\tau)e^{2\pi i\nu t'}\,dt' \int s(t'')s^*(t''+\tau)e^{-2\pi i\nu t''}\,dt''\,d\tau d\nu \\
&= \iiint s^*(t')s(t'+\tau)s(t'')s^*(t''+\tau) \underbrace{\int e^{2\pi i\nu(t'-t'')}\,d\nu}_{\delta(t'-t'')}\,dt'\,dt''\,d\tau \\
&= \iint |s(t')|^2|s(t'+\tau)|^2\,dt'\,d\tau \\
&= \int |s(t')|^2\,dt' \int |s(\tau')|^2\,d\tau' = 1,
\end{aligned}$$

where to obtain the last line we have made the change of variables $\tau \mapsto \tau' = t' + \tau$.

This result gives rise to a *radar uncertainty principle*: choosing a signal $s(t)$ so that the ambiguity surface will be narrow in one dimension will cause it to be correspondingly wide in the other dimension. In particular, a waveform with good range resolution has poor Doppler resolution, and a waveform with good Doppler resolution has poor range resolution.

3. **Symmetry:**
$$|\chi(-\tau,-\nu)| = |\chi(\tau,\nu)|.$$

4. **Effect of time translation:** The magnitude of the ambiguity function remains the same when the signal is translated in time.

5. **Effect of modulation:** The magnitude of the ambiguity function for $s(t)e^{-i\omega t}$ is the same as it is for $s(t)$.

6. **Effect of chirping:** If $\chi(\tau,\nu)$ is the ambiguity function for s, then the ambiguity function for $s(t)e^{-i\pi\alpha t^2}$ satisfies $|\chi_\alpha(\tau,\nu)| = |\chi(\tau,\nu+\alpha\tau)|$.

7. **Frequency-domain expression:** If we write s in terms of its Fourier transform[5] S as
$$s(t) = \int S(\nu)e^{-2\pi i\nu t}\,d\nu, \tag{5.1}$$
then we can write the ambiguity function as
$$\begin{aligned}
\chi(\tau,\nu) &= \int s^*(t') \int e^{-2\pi i\nu'(t'+\tau)}S(\nu')\,d\nu' e^{2\pi i\nu t'}\,dt' \\
&= \int \left[\int s(t')e^{-2\pi i(\nu-\nu')t'}\,dt'\right]^* S(\nu')e^{-2\pi i\nu'\tau}\,d\nu' \\
&= \int S^*(\nu'-\nu)S(\nu')e^{-2\pi i\nu'\tau}\,d\nu' \\
&= \int S^*(\nu'')S(\nu+\nu'')e^{-2\pi i\nu'\tau}\,d\nu'' e^{-2\pi i\nu''\tau}.
\end{aligned} \tag{5.2}$$

[5]Here it is convenient to use the convention for the Fourier transform with 2π in the exponent.

Thus, up to an overall phase factor, the ambiguity function has the same expression in the time domain and in the frequency domain.

5.2 Resolution and Cuts through the Ambiguity Function

5.2.1 Range Resolution

To study range resolution, we consider a fixed ($\nu = 0$) target. Thus in (5.2) we set $\nu = 0$:

$$|\chi(\tau, 0)| = \left| \int |S(\nu')|^2 e^{-2\pi i \nu' \tau} \, d\nu' \right|. \tag{5.3}$$

The quantity $|S|^2$ is the *power spectral density*. In order to make (5.3) as close to a delta function as possible, we would like the power spectral density to be identically one; however, such a signal would have infinite energy. Nevertheless, because the Fourier transform of a narrow peak is a broadly supported function in the Fourier domain, it is clear from (5.3) that *we obtain better range resolution when the signal bandwidth is very broad*.

This important observation is the motivation for high range resolution systems based on *ultrawideband (UWB) signals* for which $\Delta\omega \gtrsim .25\,\omega_0$. (Note that the narrowband approximation is not valid in this case and some of our results—in particular, the definition of the ambiguity function—need to be reworked when dealing with UWB waveforms.)

5.2.2 Doppler Resolution

To study Doppler resolution, we consider a target whose range is known. Thus in (4.12) we can set $\tau = 0$:

$$|\chi(0, \nu)| = \left| \int |s(t)|^2 e^{-2\pi i \nu t} \, dt \right|, \tag{5.4}$$

from which we see that *we obtain better Doppler resolution from a long-duration signal*. From (5.4) we also see that the Doppler resolution is determined only by the amplitude modulation of the signal and not by the phase.

5.3 Special Cases

In this section we discuss resolution for a few common waveforms.

Resolution is commonly quantified by one of the following criteria (see Figure 5.1):

1. The distance from the peak to the first null.

2. The distance between the first nulls.

3. The half-power width. This is sometimes called "full width at half max." Since half corresponds to about 3dB, this is also commonly referred to as the *3dB width*.

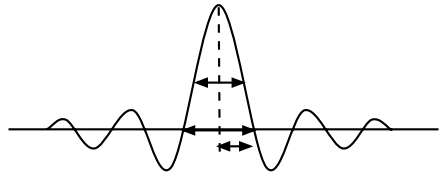

Figure 5.1. *This shows the three most common ways to quantify resolution: The 3dB width, the distance between the first nulls, and the distance from the peak to the first null.*

5.3.1 Resolution for a CW Pulse

A *continuous wave* (CW) is a single-frequency or sinusoidal wave; a CW pulse is such a wave that is chopped to form a pulse (and therefore no longer consists of a single frequency). A CW pulse of duration T has the form

$$\frac{1}{\sqrt{T}}\cos(2\pi i \nu_0 t)\text{rect}(t/T) = \text{Re}\frac{1}{\sqrt{T}}e^{2\pi i \nu_0 t}\text{rect}(t/T), \tag{5.5}$$

where the rect function is defined as

$$\text{rect}(t) = \begin{cases} 1, & |t| < 1/2, \\ 0 & \text{otherwise.} \end{cases} \tag{5.6}$$

A typical duration might be $T = 100\mu\text{s} = 100 \times 10^{-6}\text{s}$. At baseband, the CW pulse is simply

$$s(t) = (1/\sqrt{T})\text{rect}(t/T), \tag{5.7}$$

where we see that the $\sqrt{T}$ factor normalizes the waveform to have unit energy.

A straightforward calculation shows that the ambiguity function for this CW pulse is [126, 76, 110]

$$\chi(\tau, \nu) = \begin{cases} (1 - |\tau|/T)\text{sinc}\left[\pi\nu(T - |\tau|)\right], & |\tau| \le T, \\ 0 & \text{otherwise,} \end{cases} \tag{5.8}$$

where the sinc function was defined in (4.7).

The *ambiguity surface* $|\chi(\nu, \tau)|^2$ is shown in Figure 5.2(a).

For $\nu = 0$, the CW pulse ambiguity function is

$$\chi(\tau, 0) = \begin{cases} 1 - |\tau|/T, & |\tau| \le T, \\ 0 & \text{otherwise.} \end{cases} \tag{5.9}$$

If we know the velocity of our target, then the delay resolution, by the peak-to-first-null measure, is $\delta\tau_{\text{pn}} = T$, which corresponds to a range resolution of $\delta r_{\text{pm}} = cT/2$. By the null-to-null measure, we have $\delta\tau_{\text{nn}} = 2T$ and range resolution of $\delta r_{\text{nn}} = cT$. The 3dB

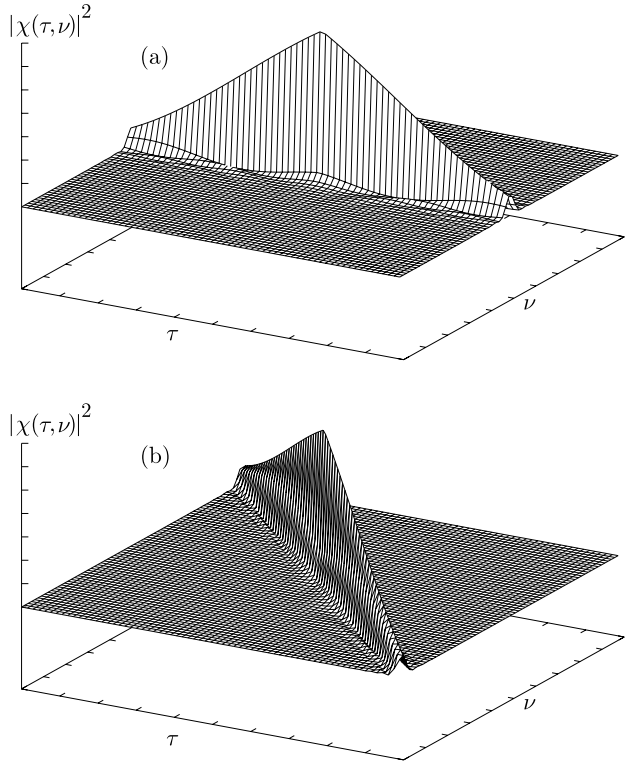

Figure 5.2. *Example ambiguity surfaces: (a) is the ambiguity surface (5.8) for a CW pulse; (b) is the ambiguity surface of a chirp (4.6).*

resolution is obtained by setting $|\chi(\tau, 0)|^2 = 1/2$, solving for τ, and multiplying by 2 to obtain the full width. This results in $\delta\tau_{3\text{dB}} = 2T(1 - 1/\sqrt{2}) \approx .586T$.

For $\tau = 0$, $|\chi(0, \nu)| = |\text{sinc}(\pi\nu T)|$. Since the first zero of the sinc function occurs when its argument is π, we find that the Doppler resolution of the CW pulse, by the peak-to-first-null measure, is $\delta\nu_{\text{pn}} = 1/T$, or, by the null-to-null measure, is $\delta\nu_{\text{nn}} = 2/T$. Since the Doppler shift is related to down-range relative velocity by $\nu_D = -2v\nu_0/c$, Doppler resolution of $2/T$ corresponds to velocity resolution of $\delta v_{\text{nn}} = c/(\nu_0 T) = \lambda_0/T$, where we have used the fact that $\lambda_0 = c/\nu_0$.

We note that a pulse with $\tau = 0$ (i.e., the return occurs at the expected time) and a Doppler shift of $1/T$ results in a matched filter output of 0! The speed $\lambda_0/(2T)$ for which this happens is called a *blind speed*.

Resolution for a Chirp

A normalized chirp is

$$p(t) = e^{i(\omega_{\min} t + \gamma t^2/2)} u_{[0,T]}(t). \tag{5.10}$$

To find the ambiguity function of a chirp, we can use (5.8) together with properties of the ambiguity function. The result is

$$|\chi(\tau,\nu)| = \begin{cases} |(T-|\tau|)\mathrm{sinc}\left[(T-|\tau|)(\pi\nu+\gamma\tau/2)\right]|, & |\tau|<T, \\ 0 & \text{else.} \end{cases} \tag{5.11}$$

The ambiguity surface $|\chi(\nu,\tau)|^2$ for a chirp is shown in Figure 5.2(b).

For $\tau = 0$, we have $|\chi(0,\nu)| = |\mathrm{sinc}(\pi\nu T)|$, which is the same result as for the CW pulse, as it should be, because the amplitude modulation is the same. Consequently the Doppler resolution is the same as for the CW pulse.

For $\nu = 0$, we find that when $\tau > 0$ the first null occurs when $\pi = (T-\tau)\gamma\tau/2$. This can be rewritten as the quadratic equation $\gamma\tau^2 - \gamma\tau T + 2\pi = 0$, from which we find

$$\begin{aligned} \tau &= \frac{\gamma T \pm \sqrt{(\gamma T)^2 - 8\pi\gamma}}{2\gamma} = \frac{T}{2} \pm \frac{T}{2}\sqrt{1-\frac{8\pi}{\gamma T^2}} \\ &= \frac{T}{2} \pm \frac{T}{2}\left(1-\frac{4\pi}{\gamma T^2}+\cdots\right) = \begin{cases} \frac{2\pi}{T\gamma} & (-\text{sign}), \\ T-\frac{2\pi}{T\gamma} & (+\text{sign}), \end{cases} \end{aligned}$$

where we have used the Taylor expansion $\sqrt{1-a} = 1 - a/2 + \ldots$ and where we have assumed that $T^2\gamma \gg 8\pi$. The root corresponding to the minus sign is the smaller of the two, so we conclude that $\delta\tau_{\mathrm{pn}} = 2\pi/(T\gamma)$ and $\delta\tau_{\mathrm{nn}} = 4\pi/(T\gamma)$. In other words, we find that the (null-to-null) delay resolution is $2/B$, where $B = 2\pi T\gamma$ is the bandwidth in Hertz. This implies that the range resolution is $\delta r_{\mathrm{pn}} = c/B$.

If we compare the delay resolution for the chirp to that for the CW pulse, we find that the *pulse compression ratio* is

$$\frac{\delta\tau_{\mathrm{pn,CW}}}{\delta\tau_{\mathrm{pn,chirp}}} = \frac{2T}{2/B} = TB.$$

This is the *time-bandwidth product*. From the delay resolution, we determine the range resolution from the relation $\delta r_{\mathrm{nn}} = c\delta\tau_{\mathrm{pn}}$; thus we find the range resolution ratio to be

$$\frac{\delta r_{\mathrm{n,CW}}}{\delta r_{\mathrm{nn,chirp}}} = \frac{cT}{c/B} = TB,$$

which can also be written

$$\frac{\delta r_{\mathrm{nn,CW}}}{TB} = \delta r_{\mathrm{pn,chirp}}.$$

In other words, *phase modulation improves the range resolution by a factor of the time-bandwidth product.* The time-bandwidth product can be very large, typically a factor of 10^4 for many radar systems.

Although large time-bandwidth products result in tremendous improvement in range resolution, the ambiguity volume reappears as uncertainty in ν. This means that the unknown velocity of a target can appear as an erroneous delay; the consequence of this is that moving objects can appear in the wrong position in radar images.

5.3.2 Resolution for Coherent Pulse Trains

Here we consider a train of N identical pulses

$$s(t) = \frac{1}{\sqrt{N}} \sum_{n=0}^{N-1} u(t - nT_{\mathrm{R}}),$$

where T_{R} is the pulse repetition interval, which might be on the order of 1ms. The reciprocal $1/T_{\mathrm{R}}$ is called the *pulse repetition frequency* (PRF). We assume that the pulse train is *coherent*, which means that the entire pulse train is referenced to the same zero of phase, so that the upmodulated waveform is simply $s(t)\cos(2\pi\nu_0 t)$.

The ambiguity function for the pulse train is

$$\begin{aligned}\chi(\tau,\nu) &= \frac{1}{N}\sum_{n=0}^{N-1}\sum_{m=0}^{N-1}\int u^*(\tau+\tau'-mT_{\mathrm{R}})u(\tau'-nT_{\mathrm{R}})e^{2\pi i\nu\tau'}d\tau' \\ &= \frac{1}{N}\sum_{n=0}^{N-1}\sum_{m=0}^{N-1}\chi_u(\tau-(n-m)T_{\mathrm{R}},\nu)e^{2\pi i\nu nT_{\mathrm{R}}},\end{aligned}$$

where χ_u denotes the ambiguity function for u and where we have used the substitution $t'' = \tau' - nT_{\mathrm{R}}$. A lengthy calculation (see [76, 110, 126]) involving a clever rearrangement of the order of summation and the summing of a geometric series results in

$$\chi(\tau,\nu) = \frac{1}{N}\sum_{p=-(N-1)}^{N-1}\chi_u(\tau-pT_{\mathrm{R}},\nu)e^{\pi i\nu T_{\mathrm{R}}(N-1-|p|)}\frac{\sin[\pi\nu T_{\mathrm{R}}(N-|p|)]}{\sin[\pi\nu T_{\mathrm{R}}]}. \tag{5.12}$$

If the pulses u are sufficiently well separated so their ambiguity functions χ_u do not overlap, then when we take the absolute value of (5.12), we obtain

$$|\chi(\tau,\nu)| = \frac{1}{N}\sum_{p=-(N-1)}^{N-1}|\chi_u(\tau-pT_{\mathrm{R}},\nu)|\left|\frac{\sin[\pi\nu T_{\mathrm{R}}(N-|p|)]}{\sin[\pi\nu T_{\mathrm{R}}]}\right|. \tag{5.13}$$

Such an ambiguity function has a "bed of nails" appearance (see Figure 5.3), with peaks at $\tau = pT_{\mathrm{R}}$, $p = -(N-1), -(N-2), \ldots, -1, 0, 1, 2, \ldots, (N-1)$ and ν such that $\pi\nu T_{\mathrm{R}}N = (m+1/2)\pi$, $m = 0, 1, 2, \ldots$.

To estimate the range resolution, we consider the $\nu = 0$ cut of (5.13):

$$|\chi(\tau,0)| = \frac{1}{N}\sum_{p=-(N-1)}^{N-1}|\chi_u(\tau-pT_{\mathrm{R}},0)|(N-|p|), \tag{5.14}$$

where we have used the fact that $\lim_{x\to 0}[\sin bx]/\sin x = b$. We see that *the range resolution of the main peak is the same as the range resolution of the individual pulse u*, but that we now have *range ambiguities* due to the extraneous peaks at $\tau = pT_{\mathrm{R}}$.

To estimate the Doppler resolution, we consider the $\tau = 0$ cut of (5.13):

$$|\chi(0,\nu)| = \frac{1}{N}\sum_{p=-(N-1)}^{N-1}|\chi_u(-pT_{\mathrm{R}},\nu)|\left|\frac{\sin[\pi\nu T_{\mathrm{R}}(N-|p|)]}{\sin[\pi\nu T_{\mathrm{R}}]}\right|.$$

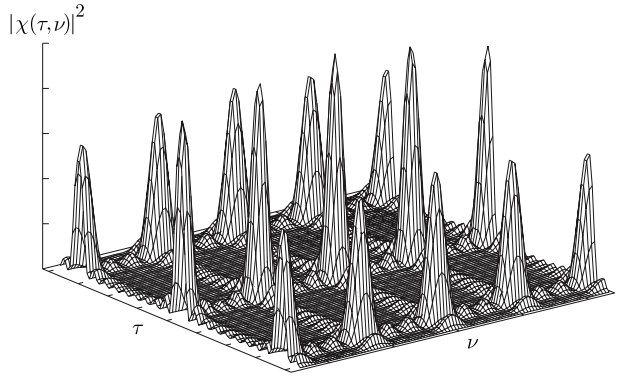

Figure 5.3. *This shows an ambiguity function for a train of pulses.*

For well-separated pulses, only the $p = 0$ term contributes:

$$|\chi(0,\nu)| = \frac{1}{N}|\chi_u(0,\nu)|\left|\frac{\sin[\pi\nu T_{\mathrm{R}}N]}{\sin[\pi\nu T_{\mathrm{R}}]}\right|. \tag{5.15}$$

Because the argument $\pi\nu T_{\mathrm{R}}N$ varies much faster than $\pi\nu T_{\mathrm{R}}$, we can focus our attention on the numerator. We find that the first null is at $\min[\delta\nu_{\mathrm{pn}}, 1/(NT_{\mathrm{R}})]$, which, for large NT_{R}, is $1/(NT_{\mathrm{R}})$. Thus we see that *the Doppler resolution of the pulse train is improved relative to that of a single pulse*.

The gain in Doppler resolution is achieved at the expense of having *ambiguous velocities*. These ambiguous velocities arise from the fact that the numerator of (5.15) has peaks at $\nu = (m + \frac{1}{2})/(NT_{\mathrm{R}})$ for m any integer. These peaks are *Doppler ambiguities*. The first Doppler ambiguity occurs at $\nu = 1/(2NT_{\mathrm{R}})$, which implies that the first ambiguous velocity is $|v| = [c/(2\nu_0)][1/(2NT_{\mathrm{R}})] = \lambda_0/(4NT_{\mathrm{R}})$, where we recall that $\lambda_0 = c/\nu_0$. The first null $\nu = 1/(NT_{\mathrm{R}})$ is also the first *blind velocity*.

For identifying airborne targets whose ranges and velocities are approximately known, the range and Doppler ambiguities may not be problematic. However, for earth mapping, the range and Doppler ambiguities are constraints on the design of the antenna and the PRF of the system.

For a pulse train of chirps, typical values might be

$\delta\tau_{\mathrm{pn}} = 1/B$	2 ns
individual pulse duration T	100 μs
pulse repetition interval T_{R}	1 ms
coherent processing interval (CPI) NT_{R}	20 s

In practice, modern pulsed radar systems do not usually measure the Doppler shift by means of the Doppler filter bank described above; instead they estimate velocity from the phase difference between returns from successive pulses.

Pulse-to-Pulse Velocity Estimation

Most modern radars use a train of high range-resolution waveforms, each pulse of which has poor Doppler resolution. Consequently they make the *start-stop* or *stop-and-shoot* approximation, which assumes that the target is stationary during the time the radar pulse illuminates the target, and moves only between pulses. Because individual pulses are so short and targets of interest are small and move slowly compared to the speed of light, this is almost always a good approximation. Under these circumstances, the velocity can be found by the change in phase of successive returns as follows.

Suppose the target travels as $R(t) = R_0 + vt$; we write $R_n = R(nT_{\mathrm{R}})$.

1. Suppose we transmit $p_n(t) = s(t)e^{-i\omega_0 t}$.
2. From (3.9) we find that the demodulated analytic signal received is $s_n(t) = s(t - 2R_n/c)e^{-i\omega_D(t-R_n/c)}e^{2i\omega_0 R_n/c}$.
3. The output of the correlation receiver is $\eta_n(\tau) = \int s^*(t' - \tau)s_n(t')dt' = \int s^*(t' - \tau)s(t' - 2R_n/c)e^{-i\omega_D(t'-R_n/c)}e^{2i\omega_0 R_n/c}dt'$.
4. At the peak $\tau = 2R_n/c$, the output is $\eta_n(2R_n/c) = \underbrace{\int |s(t' - 2R_n/c)|^2 e^{-i\omega_D t'}dt'}_{\chi(0,\omega_D)} e^{2i\omega_0 R_n/c}$.
5. The phase difference between successive pulses is $2\omega_0[R_0 + v(n+1)T_{\mathrm{R}}]/c - 2\omega_c[R_0 + vnT_{\mathrm{R}}]/c = 2\omega_0 v/c = -\omega_D$.

We note that if the velocity and pulse repetition interval are such that $2vT_{\mathrm{R}}/c$ is an integer, the phase will change by an integer multiple of 2π, and the phase of η_1 and η_2 will be identical. Such speeds are *blind speeds*.

5.4 Application: Range-Doppler Imaging

We saw in the last section that we can estimate range and range-rate from radar returns. In this section we see how we can use this information to form spatial images, provided we know something about the relative motion between the antenna and the target.

5.4.1 Range-Doppler Imaging of Rotating Targets

First we consider a rotating target. Such a target might be positioned on a laboratory turntable, or it might be an airborne target that, as it flies past the radar, appears not only to translate but also to rotate relative to the radar. Here we assume that the translational motion is removed and consider only the rotational motion.

A Point Target

We consider a point target rotating counterclockwise in a geometry in which the antenna is in the plane of rotation. (See Figure 5.4.) We take the origin of coordinates to coincide with the center of rotation; assume that this center of rotation is a large distance R_0 from

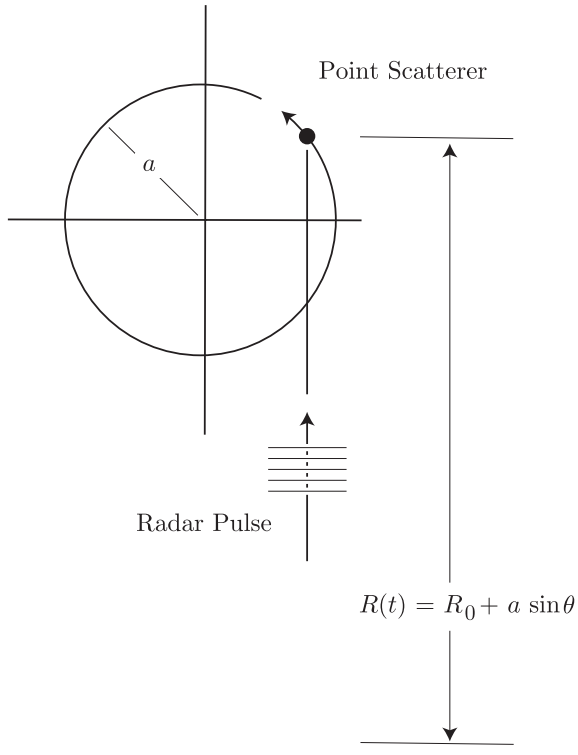

Figure 5.4. *The geometry for locating a point target known to be rotating.*

the antenna. The fact that the range is large means that the incident wave is approximately a plane wave, which means that all horizontal points are (approximately) at the same range. If the target is positioned at $(x, y) = a(\cos\theta, \sin\theta)$, then its range is

$$R = R_0 + y = R_0 + a\sin\theta.$$

If its angular velocity is $\dot{\theta} = d\theta/dt$, then its velocity vector is $a\dot{\theta}(-\sin\theta, \cos\theta)$, its tangential speed is $|v| = a\dot{\theta}$, and the down-range (y) component of the velocity is $\dot{R} = |v|\cos\theta = a\dot{\theta}\cos\theta$. However, since $x = a\cos\theta$, this down-range velocity can be written $\dot{R} = x\dot{\theta}$, where x is the cross-range component of the position. We note that for $x > 0$, the down-range velocity is negative, whereas for $x < 0$, it is positive.

This means that since a radar system can measure range $(R_0 + y)$ and range-rate $(\dot{R} = x\dot{\theta})$, it can determine the (x, y) location of the point in space! In particular, the radar measures the time delay $\tau = 2R/c$ and the Doppler shift

$$\nu_D = -\frac{2\dot{R}}{c}\nu_0 = -\frac{2x\dot{\theta}}{c}\nu_0,$$

which means that the coordinates of the point are given by

$$(x, y) = \left(\frac{-\nu_D}{\nu_0}\frac{c}{2\dot{\theta}},\ \frac{c\tau}{2} - R_0\right).$$

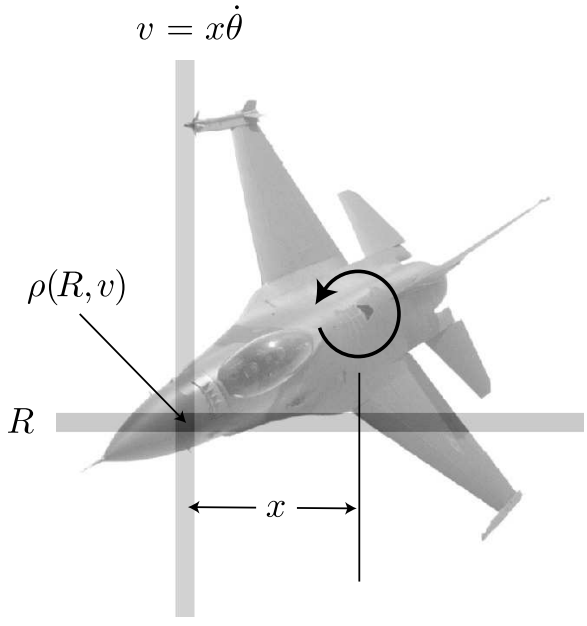

Figure 5.5. *An extended target known to be rotating.*

Extended Targets

Next we suppose that $\tilde{\rho}(x, y)$ represents a distribution of scatterers associated with a single extended target (such as an airplane as in Figure 5.5). Then $\rho(\tau, \nu) = \tilde{\rho}(-\nu c/(2\nu_0\dot{\theta}), (c\tau/2) - R_0)$ is the corresponding distribution of delays and Doppler shifts we expect to see from the target. Consequently from $\rho(\tau, \nu)$, we form a spatial image by

$$\tilde{\rho}(x, y) = \rho(2\dot{\theta}x\nu_0/c, (R_0 + y)c/2).$$

In cases when $\tilde{\rho}(x, y)$ represents a maneuvering aircraft, the rotation rate $\dot{\theta}$ is unknown, and the result is an image in which the cross-range dimension is scaled by the unknown $\dot{\theta}$. However, generally an object can be recognized from such a scaled image.

We recall that $\rho(\tau, \nu)$ is related to the output of the bank of matched filters by (4.11), and the PSF of the imaging system is given by $\chi(\tau, \nu)\exp(2\pi i\nu\tau)$. We have already investigated the resolution determined by the ambiguity function; the results are summarized in Table 5.1.

We note that for individual waveforms, the cross-range resolution is inversely proportional to $\Delta\theta = \dot{\theta}T$, which is the total angular aperture over which we view the target. For pulse trains, the cross-range resolution is inversely proportional to $\Delta\theta = \dot{\theta}NT_{\mathrm{R}}$, which is again the total angular aperture for the full coherent processing interval (CPI).

We see that for imaging an airplane, the resolution of the CW pulse is unacceptable. The single chirp has acceptable range resolution, but the cross-range resolution is still unacceptable. It is only the chirp train that has acceptable resolution. However, this resolution is attained only for long pulse trains, and during a long CPI the target may rotate enough so that the scatterers are in different positions. For example, during one second, an airborne

Table 5.1. *Resolution at X-band.*

$\lambda = 3\text{cm}, \dot{\theta} = 10^\circ/\text{sec} = .16$ radians/sec
$T = 10^{-4}\text{sec}, B = 500\text{MHz}$
$N = 10^3, T_R = 3 \cdot 10^{-4}$ sec $\Rightarrow NT_R = .3\text{sec}$

Waveform	Range resolution δr_{nn}	Velocity resolution δv_{nn}	Cross-range resolution $\delta x = \delta v_{nn}/\dot{\theta}$
CW pulse Duration T	$cT \approx 10^4$ m	$\lambda/T \approx 10^2$ m/sec	$\lambda/(\dot{\theta}T) \approx 1200$ m
Chirp Duration T Bandwidth B	$c/B \approx .6$m	$\lambda/T \approx 10^2$ m/sec	$\lambda/(\dot{\theta}T) \approx 1200$ m
CW pulse train $NT_R = .3$sec	$cT = 10^4$m	$\lambda/(NT_R) \approx .1$m/sec	$\lambda/(\dot{\theta}NT_R) \approx .6$m
Train of N chirps $NT_R = .3$sec	$c/B \approx .6$m	$\lambda/(NT_R) \approx .1$m/sec	$\lambda/(\dot{\theta}NT_R) \approx .6$m

target could easily rotate through .05 radians (10°). If it has a 10-meter radius, then the extreme points on the target move 10m $\times .05$ radians $= .5$ meters, which is more than a resolution cell. Large targets such as ships can move even farther, and the result is a blurred image. Clearly we need an imaging approach that can accommodate target motion during the imaging process. For this, we need a fully three-dimensional scattering model, which we develop in the next chapter.

The Range-Doppler Imaging Projection

Forming an image of any type generally involves a two-dimensional projection of a three-dimensional scene. Optical photography, for example, projects onto a single image point all points lying along a ray through the focal point of the lens. This is the *perspective projection*.

Radar imaging involves a different projection from three dimensions to two dimensions. In a range-Doppler image, all scatterers at the same range and relative velocity appear at the same point in the image. For the case of a far-away target whose axis of rotation is perpendicular to the radar line of sight, this means that all scatterers on a line parallel to the axis of rotation will appear at the same point in the image. This is an *orthographic projection*.

5.4.2 Range-Doppler Synthetic-Aperture Radar

To map the earth, we can mount a radar system on a moving platform such as an airplane or satellite. For simplicity, we assume that the earth is a flat plane and that the platform moves in a straight horizontal line. Then we can use radar as follows to locate a point target on the earth. From the time delay τ of a scattered signal, we know that the target must lie at range $R = c\tau/2$. The *iso-range* surface at range R, which is the set of points at range R

from the platform, is a sphere of radius R, and this sphere intersects the flat earth in a circle. (See Figure 1.6.) Thus the return at time τ must come from a target on this circle. From the Doppler shift ν_D (3.8), we know that the range of the target must change as $\dot{R} = c\nu_D/(2\nu_0)$ as the platform flies past. The down-range component of the velocity is $\dot{R} = \hat{\boldsymbol{R}} \cdot \boldsymbol{v}$, where $\hat{\boldsymbol{R}}$ is a unit vector from the platform to the target, and $\boldsymbol{v}$ is the platform velocity. (Here we take the origin of coordinates at the radar platform.) The set of points $\boldsymbol{R}$ for which $\hat{\boldsymbol{R}} \cdot \boldsymbol{v}$ is constant is a cone whose axis is the vector $\boldsymbol{v}$. (See Figures 5.6 and 5.7.) This cone intersects the earth in a hyperbola. Such a constant-Doppler curve is an *iso-Doppler* curve.

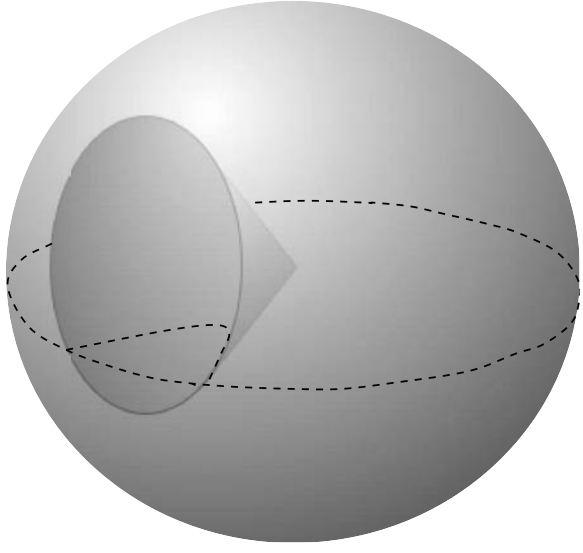

Figure 5.6. *The intersection of the constant-range sphere with the constant-Doppler cone.*

Thus from measuring the range and Doppler shift, we find that the target must lie on the (assumed flat) earth at the intersection of the constant-range circle and the constant-Doppler hyperbola. We note that there are *two* such intersections, one to the left of the platform velocity vector and one to the right. Thus from a given range and Doppler measurement, we cannot determine which of these two points is the scatterer location. This is referred to as the *left-right* ambiguity. To handle this ambiguity, SAR systems use an antenna beam pattern that illuminates only one of these intersections. This is why SAR systems are always side-looking.

For a distribution of scatterers on a flat earth, the output $\eta(\tau, \nu)$ of the filter bank provides an image of the earth. Again the ambiguity function is the PSF for this imaging system.

The image formed in this manner is unfocused, because it does not account for the change in radar position during the time the measurements are taken. Again, in order to account for this effect, we need a full three-dimensional scattering model; this is found in the next chapter. Nevertheless, the basic intuition underlying radar imaging is to locate a target according to its range and Doppler shift.

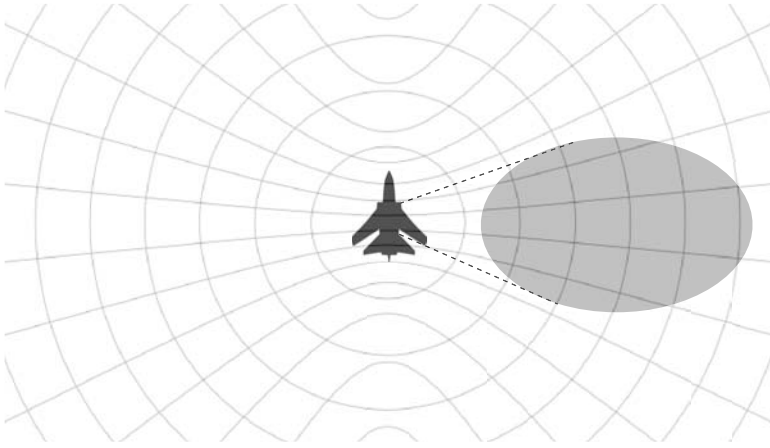

Figure 5.7. *The constant-range circles and constant-Doppler hyperbolas. The grey region shows the antenna beam, which illuminates only one of the two intersections of a given range circle and Doppler hyperbola.*

5.5 Mathematical Issues Related to the Ambiguity Function

We have seen that in the simplest case, the scattered radar signal is a time-delayed, Doppler-shifted version of the transmitted signal. The time delay can be thought of as a temporal translation of the signal, and such translations have a group structure. Similarly, Doppler shifts also have a group structure. Consequently the ambiguity function arises in group representation theory, and the properties of the ambiguity function can be thought of as special cases of certain theorems in group representation theory. For more information about these connections, see [17, 84, 12].

We have seen that for a given signal, we can extract various properties of the corresponding ambiguity function. Even more interesting is the inverse problem, which is to construct a signal with a given ambiguity function. This is addressed in [17].

Some open problems related to the radar ambiguity function are listed in Chapter 11.

Part II

Radar Imaging

Chapter 6

Wave Propagation in Two and Three Dimensions

Throughout the rest of the book, we consider only high-range-resolution pulses and use the start-stop approximation. Thus we consider only scattering from stationary targets.

6.1 Scalar Wave Propagation

Rather than the full Maxwell equations, we use the simplified scalar model

$$\left(\nabla^2 - \frac{1}{c^2(\boldsymbol{x})}\frac{\partial^2}{\partial t^2}\right)\mathcal{E}(t,\boldsymbol{x}) = 0, \tag{6.1}$$

in which we think of $c(\boldsymbol{x})$ as the local propagation speed of electromagnetic waves. We have seen that in free space, where $c(\boldsymbol{x}) = c_0$, this equation is a good model for the propagation of each Cartesian component of the electric field. We will frequently drop the subscript 0 on c_0.

Scattering can be thought of as being due to perturbations in the wave speed, which we write as

$$\frac{1}{c^2(\boldsymbol{x})} = \frac{1}{c_0^2} - V(\boldsymbol{x}), \tag{6.2}$$

where V is the *reflectivity function*. Equations (6.1) and (6.2) do not provide an entirely accurate model for electromagnetic scattering from an object; nevertheless, this is a commonly used model for radar scattering, with the understanding that $V(\boldsymbol{x})$ does not exactly correspond to the perturbation in the electromagnetic wave speed in the material, but rather represents a measure of the radar reflectivity for the polarization measured by the antenna. More accurate scattering models can be found in [19], [62] and references therein.

For a moving target, we use a time-varying reflectivity function $V(\boldsymbol{x}, t)$.

6.2 Basic Facts about the Wave Equation

A *fundamental solution* [132] of the wave equation is a generalized function [54] satisfying

$$\left(\nabla^2 - c_0^{-2}\partial_t^2\right) g(t,\boldsymbol{x}) = -\delta(t)\delta(\boldsymbol{x}). \tag{6.3}$$

The solution[6] of (6.3) that is useful for us is

$$g(t,\boldsymbol{x}) = \frac{\delta(t-|\boldsymbol{x}|/c_0)}{4\pi|\boldsymbol{x}|} = \int \frac{e^{-i\omega(t-|\boldsymbol{x}|/c_0)}}{8\pi^2|\boldsymbol{x}|}d\omega, \tag{6.4}$$

where in the second equality we have used (8). The function $g(t,\boldsymbol{x})$ is the field at $(t,\boldsymbol{x})$ due to a source at the origin at time 0 and is called the *outgoing fundamental solution* or *(outgoing) Green's function* [61] [103].

The Green's function enables us to solve the constant-speed wave equation with *any* source term. In particular, the outgoing solution of

$$\left(\nabla^2 - c_0^{-2}\partial_t^2\right) u(t,\boldsymbol{x}) = j(t,\boldsymbol{x}) \tag{6.5}$$

is

$$u(t,\boldsymbol{x}) = -\int g(t-t',\boldsymbol{x}-\boldsymbol{y})\, j(t',\boldsymbol{y})dt'd\boldsymbol{y}. \tag{6.6}$$

In the frequency domain, the equations corresponding to (6.3) and (6.4) are

$$(\nabla^2 + k^2)G = -\delta \qquad \text{and} \qquad G(\omega,\boldsymbol{x}) = \frac{e^{ik|\boldsymbol{x}|}}{4\pi|\boldsymbol{x}|}, \tag{6.7}$$

where we have written $k = \omega/c_0$.

6.3 Introduction to Scattering Theory

Equation (6.6) tells us how a source j radiates a field into free space. We refer to this field as the *incident* field, because it is incident on the scatterers. In scattering problems, we are interested in how these scatterers cause perturbations in the incident field. One approach to doing this is to simply solve (6.1) directly, using, for example, numerical time-domain techniques. However, for many purposes, it is convenient to reformulate the scattering problem in terms of an integral equation.

6.3.1 The Lippmann–Schwinger Integral Equation

As in Chapter 3, we write $\mathcal{E}^{\text{tot}} = \mathcal{E}^{\text{in}} + \mathcal{E}^{\text{sc}}$, where $\mathcal{E}^{\text{in}}$ satisfies a wave equation in free space. Consequently we compare the full wave propagation problem (6.8) to (6.9) defining the incident field:

$$\left(\nabla^2 - c^{-2}(\boldsymbol{x})\partial_t^2\right)\mathcal{E}^{\text{tot}}(t,\boldsymbol{x}) = j(t,\boldsymbol{x}), \tag{6.8}$$

$$(\nabla^2 - c_0^{-2}\partial_t^2)\mathcal{E}^{\text{in}}(t,\boldsymbol{x}) = j(t,\boldsymbol{x}), \tag{6.9}$$

where the source term j is a model for the source, namely, the current density on the antenna. In (6.8), we use (6.2), and then subtract (6.9) from (6.8). This results in the equation for the scattered field:

$$\left(\nabla^2 - c_0^{-2}\partial_t^2\right)\mathcal{E}^{\text{sc}}(t,\boldsymbol{x}) = -V(\boldsymbol{x})\partial_t^2\mathcal{E}^{\text{tot}}(t,\boldsymbol{x}). \tag{6.10}$$

[6] Verifying that (6.4) satisfies (6.3) away from $(t,\boldsymbol{x}) = (0,\boldsymbol{0})$ is easy, but in a neighborhood of $(0,\boldsymbol{0})$, the machinery of the theory of distributions or generalized functions is needed. Readers unfamiliar with this theory can simply accept (6.4) on faith and proceed.

This equation is of the form (6.5), with $j = -V\partial_t^2\mathcal{E}^{\text{tot}}$. Consequently, we can use (6.6) to express $\mathcal{E}^{\text{sc}}$ in terms of $j = -V\partial_t^2\mathcal{E}^{\text{tot}}$. This results in the *Lippmann–Schwinger* integral equation

$$\boxed{\mathcal{E}^{\text{sc}}(t,\boldsymbol{x}) = \iint g(t-\tau,\boldsymbol{x}-z)V(z)\partial_\tau^2\mathcal{E}^{\text{tot}}(\tau,z)d\tau dz.} \tag{6.11}$$

Since $\mathcal{E}^{\text{tot}} = \mathcal{E}^{\text{in}} + \mathcal{E}^{\text{sc}}$, the scattered field $\mathcal{E}^{\text{sc}}$ appears on both sides of (6.11), which means that this is not simply a formula for $\mathcal{E}^{\text{sc}}$, but an equation that must be solved. With (6.4), (6.11) is

$$\mathcal{E}^{\text{sc}}(t,\boldsymbol{x}) = \iint \frac{\delta(t-\tau-|\boldsymbol{x}-z|/c)}{4\pi|\boldsymbol{x}-z|}V(z)\partial_\tau^2\mathcal{E}^{\text{tot}}(\tau,z)d\tau dz. \tag{6.12}$$

6.3.2 The Lippmann–Schwinger Equation in the Frequency Domain

To write the corresponding equations in the frequency domain, we write

$$E(\omega) = \int e^{i\omega t}\mathcal{E}(t)dt. \tag{6.13}$$

Thus (6.8) and (6.9) become

$$\begin{aligned}\left(\nabla^2 + \frac{\omega^2}{c^2(\boldsymbol{x})}\right)E^{\text{tot}} &= J(\omega,\boldsymbol{x}),\\ \left(\nabla^2 + \frac{\omega^2}{c_0^2}\right)E^{\text{in}} &= J(\omega,\boldsymbol{x}).\end{aligned} \tag{6.14}$$

In the frequency domain, the Lippmann–Schwinger equation (6.11) becomes

$$E^{\text{sc}}(\omega,\boldsymbol{x}) = -\int G(\omega,\boldsymbol{x}-z)V(z)\omega^2E^{\text{tot}}(\omega,z)dz, \tag{6.15}$$

and (6.12) is

$$E^{\text{sc}}(\omega,\boldsymbol{x}) = -\int \frac{e^{ik|\boldsymbol{x}-z|}}{4\pi|\boldsymbol{x}-z|}V(z)\omega^2E^{\text{tot}}(\omega,z)dz. \tag{6.16}$$

6.3.3 The Neumann Series

A natural approach to solving (6.16) follows from rewriting it in operator form as

$$E^{\text{tot}} = E^{\text{in}} - \mathcal{G}\mathcal{V}E^{\text{tot}}, \tag{6.17}$$

where $\mathcal{G}$ denotes the operator of convolution with G and $\mathcal{V}$ denotes the operator of multiplication by $V\omega^2$. We would like to solve (6.17) by $E^{\text{tot}} = (\mathcal{I}+\mathcal{G}\mathcal{V})^{-1}E^{\text{in}}$. If we note the analogy with the geometric series $(1+a)^{-1} = 1 - a + a^2 - a^3 + \cdots$, we could hope to solve (6.17) as

$$E^{\text{tot}} = (I+\mathcal{G}\mathcal{V})^{-1}E^{\text{in}} = E^{\text{in}} - \mathcal{G}\mathcal{V}E^{\text{in}} + (\mathcal{G}\mathcal{V})^2E^{\text{in}} - (\mathcal{G}\mathcal{V})^3E^{\text{in}} + \cdots. \tag{6.18}$$

The expansion (6.18) is called the *Neumann* series, and it can be shown to converge [108, 113] when the operator $\mathcal{G}\mathcal{V}$ is small in some sense, which is a *weak-scattering* assumption.

More explicitly, (6.18) is

$$E^{\text{tot}}(\boldsymbol{x}) = E^{\text{in}}(\boldsymbol{x}) + \int G(\boldsymbol{x}-\boldsymbol{x}')V(\boldsymbol{x}')\omega^2 E^{\text{in}}(\boldsymbol{x}')\,d\boldsymbol{x}' \tag{6.19}$$
$$+ \int G(\boldsymbol{x}-\boldsymbol{x}')V(\boldsymbol{x}')\omega^2 \int G(\boldsymbol{x}'-\boldsymbol{y})V(\boldsymbol{y})\omega^2 E^{\text{in}}(\boldsymbol{y})\,d\boldsymbol{x}'\,d\boldsymbol{y} + \cdots .$$

If we think of G as a *propagator*, so that $G(\boldsymbol{x}-\boldsymbol{x}')$ propagates the field from $\boldsymbol{x}'$ to $\boldsymbol{x}$, then we see that the second term on the right side of (6.19) can be interpreted as the incident wave E^{in} scattering from the scatterer at $\boldsymbol{x}'$ with strength $V(\boldsymbol{x}')\omega^2$ and then being propagated from $\boldsymbol{x}'$ to the measurement location $\boldsymbol{x}$. Similarly, the last term on the right side of (6.19) can be interpreted as the incident wave scattering at $\boldsymbol{y}$ with strength $V(\boldsymbol{y})\omega^2$, propagating from $\boldsymbol{y}$ to $\boldsymbol{x}'$, scattering at $\boldsymbol{x}'$ with strength $V(\boldsymbol{x}')\omega^2$, and propagating to the measurement location $\boldsymbol{x}$. This is illustrated in Figure 6.1.

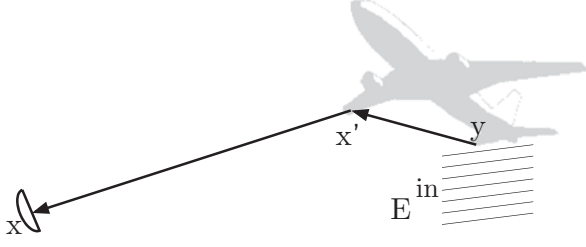

Figure 6.1. *A diagram corresponding to the last term on the right side of* (6.19).

6.4 The Born Approximation

For radar imaging, we measure $\mathcal{E}^{\text{sc}}$ at the antenna, and we would like to determine V. However, both V and $\mathcal{E}^{\text{sc}}$ in the neighborhood of the target V are unknown, and in (6.11) these unknowns are multiplied together. This nonlinearity makes it difficult to solve for V. Consequently, almost all work on radar imaging involves making the *Born* approximation, which is also known as the *weak-scattering* or *single-scattering* approximation. The Born approximation is to drop all the terms of (6.19) involving more than one factor of V. This corresponds to replacing $\mathcal{E}^{\text{tot}}$ on the right side of (6.11) by $\mathcal{E}^{\text{in}}$, which is known. This results in a formula for $\mathcal{E}^{\text{sc}}$ in terms of V:

$$\mathcal{E}^{\text{sc}}(t,\boldsymbol{x}) \approx \mathcal{E}_B^{(t,\boldsymbol{x})} := \iint g(t-\tau,\boldsymbol{x}-\boldsymbol{z})V(\boldsymbol{z})\partial_\tau^2 \mathcal{E}^{\text{in}}(\tau,\boldsymbol{z})d\tau d\boldsymbol{z}. \tag{6.20}$$

In the frequency domain, the Born approximation is

$$E_B^{\text{sc}}(\omega,\boldsymbol{x}) = -\int \frac{e^{ik|\boldsymbol{x}-\boldsymbol{z}|}}{4\pi|\boldsymbol{x}-\boldsymbol{z}|} V(\boldsymbol{z})\omega^2 E^{\text{in}}(\omega,\boldsymbol{z})d\boldsymbol{z}. \tag{6.21}$$

The Born approximation is very useful, because it makes the imaging problem linear. However, it is not necessarily a good approximation, and some images show artifacts due to the neglect of the multiple-scattering terms of (6.18). For example, the vertical streaks near the aircraft tail in Figure 6.2 are due to energy that enters the engine ducts, undergoes multiple scattering, and emerges at a later time. Because the scattered wave returns to the radar later than expected from the single-scattering model, it is interpreted as having come from a structure farther from the radar.

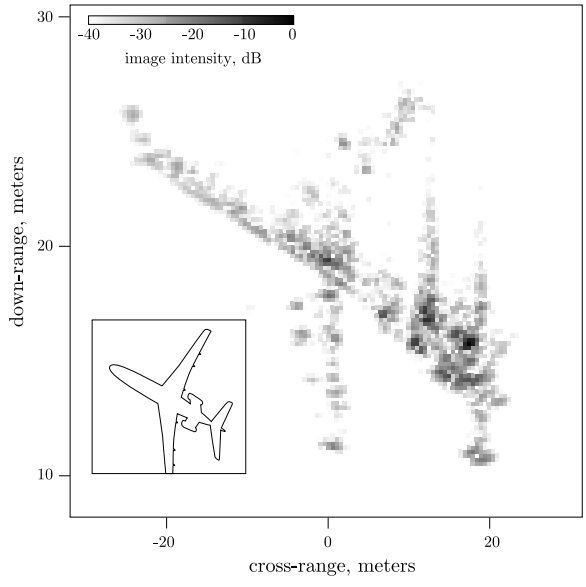

Figure 6.2. *An inverse synthetic aperture radar (ISAR—see chapter 7) image of a Boeing 727 [135] showing artifacts due to multiple scattering.*

Another example of artifacts due to the Born approximation is evident in Figure 6.3. In the rightmost image on the bottom row, we see three gun barrels. The brightest one is from direct scattering; the second is from the round-trip paths involving the radar and one bounce from the ground; the third is from a path that bounces from the ground to the gun barrel and back to the ground before returning to the radar.

6.5 The Incident Field

The incident field $\mathcal{E}^{\text{in}}$ is obtained by solving (6.9). We will consider the incident field in more detail in Chapter 8. For now, we use a simplified point-like antenna model, for which $j(t, \boldsymbol{x}) = p(t)\delta(\boldsymbol{x} - \boldsymbol{x}^0)$, where p is the waveform transmitted by the antenna. In the frequency domain, the corresponding source for (6.14) is $J(\omega, \boldsymbol{x}) = P(\omega)\delta(\boldsymbol{x} - \boldsymbol{x}^0)$, where we write P for the inverse Fourier transform of p:

$$p(t) = \frac{1}{2\pi} \int e^{-i\omega t} P(\omega) d\omega. \tag{6.22}$$

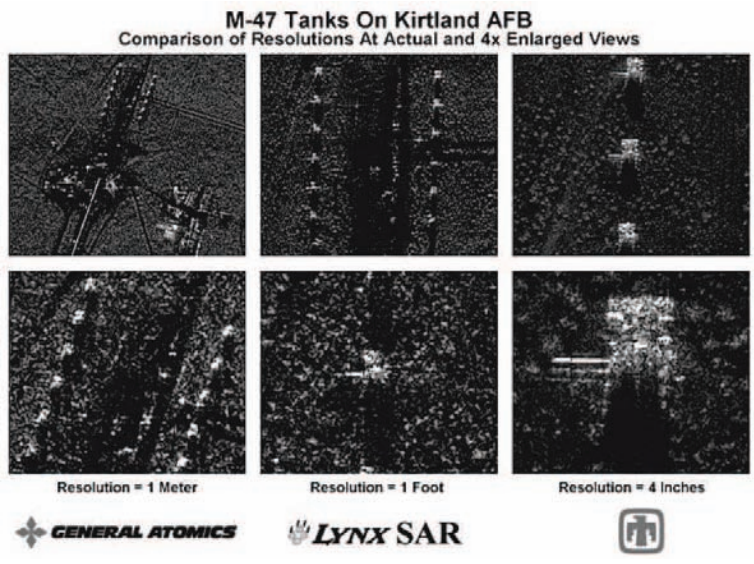

Figure 6.3. *Images from the Lynx SAR system at different resolutions. Here the radar illuminates the scene from the top of the figure. Note the three gun barrels in the bottom right image; this is a multiple scattering artifact (courtesy of Sandia National Laboratories).*

Using (6.7), we find that the incident field in the frequency domain is

$$\begin{aligned} E^{in}(\omega, \boldsymbol{x}) &= -\int G(\omega, \boldsymbol{x} - \boldsymbol{y}) P(\omega) \delta(\boldsymbol{y} - \boldsymbol{x}^0) d\boldsymbol{y} \\ &= -P(\omega) \frac{e^{ik|\boldsymbol{x} - \boldsymbol{x}^0|}}{4\pi |\boldsymbol{x} - \boldsymbol{x}^0|}. \end{aligned} \tag{6.23}$$

6.6 Model for the Scattered Field

Using (6.23) in (6.21), we find that the Born-approximated scattered field back at the transmitter location $\boldsymbol{x}^0$ is

$$E_B^{sc}(\omega, \boldsymbol{x}^0) = P(\omega)\, \omega^2 \int \frac{e^{2ik|\boldsymbol{x}^0 - z|}}{(4\pi)^2 |\boldsymbol{x}^0 - z|^2} V(z) dz. \tag{6.24}$$

We Fourier transform (6.24) to write the time-domain field as

$$\begin{aligned} \mathcal{E}_B^{sc}(t, \boldsymbol{x}^0) &= \iint \frac{e^{-i\omega(t - 2|\boldsymbol{x}^0 - z|/c)}}{2\pi (4\pi |\boldsymbol{x}^0 - z|)^2} k^2 P(\omega) V(z) d\omega dz \\ &= \int \frac{\ddot{p}(t - 2|\boldsymbol{x}^0 - z|/c)}{(4\pi |\boldsymbol{x}^0 - z|)^2} V(z) dz. \end{aligned} \tag{6.25}$$

We note the $1/R^2$ geometrical decay (where $R = |\boldsymbol{x}^0 - \boldsymbol{z}|$), which leads to the $1/R^4$ power decay mentioned in the chapter on matched filtering.

6.7 The Effect of Matched Filtering

The output of the correlation receiver is

$$\begin{aligned}
\eta(t, \boldsymbol{x}^0) &\approx \int p^*(t'-t)\mathcal{E}_B^{sc}(t', \boldsymbol{x}^0)dt' \\
&= \int \left(\frac{1}{2\pi} \int e^{i\omega'(t'-t)} P^*(\omega')d\omega' \right) \\
&\qquad \times \iint \frac{e^{-i\omega(t'-2|\boldsymbol{x}^0-\boldsymbol{z}|/c)}}{2\pi(4\pi|\boldsymbol{x}^0-\boldsymbol{z}|)^2} k^2 P(\omega)V(\boldsymbol{z})d\omega d\boldsymbol{z}\, dt' \\
&= \iiint \underbrace{\frac{1}{2\pi} \int e^{i(\omega'-\omega)t'} dt'}_{\delta(\omega'-\omega)} \frac{e^{-i\omega(t-2|\boldsymbol{x}^0-\boldsymbol{z}|/c)}}{(4\pi|\boldsymbol{x}^0-\boldsymbol{z}|)^2} k^2 P(\omega)P^*(\omega')V(\boldsymbol{z})d\omega' d\omega d\boldsymbol{z} \\
&= \iint \frac{e^{-i\omega(t-2|\boldsymbol{x}^0-\boldsymbol{z}|/c)}}{(4\pi|\boldsymbol{x}^0-\boldsymbol{z}|)^2} k^2 |P(\omega)|^2 V(\boldsymbol{z})d\omega d\boldsymbol{z}. \qquad (6.26)
\end{aligned}$$

Here we do not look for a Doppler shift because we are considering only high-range-resolution pulses. We see that the effect of matched filtering is simply to replace $P(\omega)$ by $2\pi|P(\omega)|^2$.

Chapter 7

Inverse Synthetic-Aperture Radar

In this chapter we consider the case of an isolated airborne target. This enables us to ignore issues related to the antenna beam.

7.1 The Far-Field Approximation

Most radar imaging involves targets that are far from the antenna. In these cases, the following far-field approximation of the Green's function is very useful.

We begin with the *far-field* expansion, which is valid for $|\boldsymbol{x}| \gg |\boldsymbol{y}|$:

$$|\boldsymbol{x}-\boldsymbol{y}| = \sqrt{(\boldsymbol{x}-\boldsymbol{y})\cdot(\boldsymbol{x}-\boldsymbol{y})} = \sqrt{|\boldsymbol{x}|^2 - 2\boldsymbol{x}\cdot\boldsymbol{y} + |\boldsymbol{y}|^2} = |\boldsymbol{x}|\sqrt{1 - \frac{2\hat{\boldsymbol{x}}\cdot\boldsymbol{y}}{|\boldsymbol{x}|} + \frac{|\boldsymbol{y}|^2}{|\boldsymbol{x}|^2}}$$
$$= |\boldsymbol{x}|\left(1 - \frac{\hat{\boldsymbol{x}}\cdot\boldsymbol{y}}{|\boldsymbol{x}|} + O\left(\frac{|\boldsymbol{y}|^2}{|\boldsymbol{x}|^2}\right)\right) = |\boldsymbol{x}| - \hat{\boldsymbol{x}}\cdot\boldsymbol{y} + O\left(\frac{|\boldsymbol{y}|^2}{|\boldsymbol{x}|}\right), \tag{7.1}$$

where we have used the Taylor expansion $\sqrt{1+a} = 1 + a/2 + O(a^2)$ and where we have written $\hat{\boldsymbol{x}} = \boldsymbol{x}/|\boldsymbol{x}|$. Note that this far-field expansion involves an implicit choice of an origin of coordinates.

Figure 7.1. *The far-field expansion* (7.1).

Using (7.1) in the exponential appearing in the Green's function, we have

$$e^{ik|\boldsymbol{x}-\boldsymbol{y}|} = e^{ik|\boldsymbol{x}|}e^{-ik\hat{\boldsymbol{x}}\cdot\boldsymbol{y}}e^{O\left(k|\boldsymbol{y}|^2/|\boldsymbol{x}|\right)} = e^{ik|\boldsymbol{x}|}e^{-ik\hat{\boldsymbol{x}}\cdot\boldsymbol{y}}\left(1 + O\left(\frac{k|\boldsymbol{y}|^2}{|\boldsymbol{x}|}\right)\right), \tag{7.2}$$

where in the last factor of (7.2) we have used the expansion $e^a = 1 + O(a)$.

Similarly we expand $|\boldsymbol{x}-\boldsymbol{y}|^{-1}$ to obtain

$$\frac{1}{|\boldsymbol{x}-\boldsymbol{y}|}=\frac{1}{|\boldsymbol{x}|}\frac{1}{\sqrt{1-\frac{2\hat{\boldsymbol{x}}\cdot\boldsymbol{y}}{|\boldsymbol{x}|}+O\left(\frac{|\boldsymbol{y}|^2}{|\boldsymbol{x}|^2}\right)}}=\frac{1}{|\boldsymbol{x}|}\left(1+O\left(\frac{|\boldsymbol{y}|}{|\boldsymbol{x}|}\right)\right). \tag{7.3}$$

Using this and the expansion $(1+a)^{-1}=1+O(a)$, we obtain the large-$|x|$ expansion of the Green's function

$$G(\boldsymbol{x}-\boldsymbol{y})=\frac{e^{ik|\boldsymbol{x}-\boldsymbol{y}|}}{4\pi|\boldsymbol{x}-\boldsymbol{y}|}=\frac{e^{ik|\boldsymbol{x}|}}{4\pi|\boldsymbol{x}|}e^{-ik\hat{\boldsymbol{x}}\cdot\boldsymbol{y}}\left(1+O\left(\frac{|\boldsymbol{y}|}{|\boldsymbol{x}|}\right)\right)\left(1+O\left(\frac{k|\boldsymbol{y}|^2}{|\boldsymbol{x}|}\right)\right). \tag{7.4}$$

We see that the remainder terms are small if

1. $|\boldsymbol{y}|\ll|\boldsymbol{x}|$ and
2. $k|\boldsymbol{y}|^2\ll|\boldsymbol{x}|$.

7.2 The Far-Field Expansion in the Scalar Wave Born Approximation

Here we assume that the source is a point-like antenna with the time dependence $p(t)$, so that in the frequency domain, the incident wave E^{in} has the form (6.23). For this source, the corresponding Born-approximated scattered field is given by (6.24). The next step is matched filtering, which results in (6.26). In (6.26), we choose the origin of coordinates to be in or near the target and use the far-field expansion (7.4) (with $\boldsymbol{z}$ playing the role of $\boldsymbol{y}$) in (6.26):

$$\eta_B(t)\approx\frac{1}{(4\pi)^2|\boldsymbol{x}^0|^2}\int e^{-i\omega(t-2|\boldsymbol{x}^0|/c+2\hat{\boldsymbol{x}}^0\cdot\boldsymbol{z}/c)}k^2|P(\omega)|^2V(\boldsymbol{z})d\omega d\boldsymbol{z}. \tag{7.5}$$

If we inverse Fourier transform[7] (7.5), in the frequency domain we obtain

$$D_B(\omega)\approx\frac{e^{2ik|\boldsymbol{x}^0|}}{(4\pi)^2|\boldsymbol{x}^0|^2}k^2|P(\omega)|^2\underbrace{\int e^{-2ik\hat{\boldsymbol{x}}^0\cdot\boldsymbol{z}}V(\boldsymbol{z})d\boldsymbol{z}}_{\mathcal{F}[V](2k\hat{\boldsymbol{x}}^0)}. \tag{7.6}$$

7.3 Inverse Synthetic-Aperture Imaging

We see that D_B of (7.6) is proportional to the Fourier transform of V, evaluated at the spatial frequency $2k\hat{\boldsymbol{x}}^0$. Thus if we move our antenna to obtain different views $\hat{\boldsymbol{x}}^0$, we obtain different Fourier components of the target reflectivity function V. The moving antenna is said to sweep out a *synthetic aperture*, and radar imaging based on this scheme is called *Synthetic-Aperture Radar (SAR)*. We will consider this in more detail in Chapter 9.

[7] Here we use convention (3).

7.3.1 ISAR Systems

Moving the antenna to view a fixed target from a different orientation is equivalent to using a fixed antenna to view a rotating target. Radar imaging that uses a fixed antenna and a rotating target is called *Inverse Synthetic-Aperture Radar (ISAR)*. This imaging scheme is typically used for imaging airplanes, spacecraft, and ships. In these cases, the target is relatively small and usually isolated.

Typical ISAR systems transmit a train of HRR pulses. For isolated targets, measurements from the nth pulse normally contain no reflections from earlier pulses, and consequently range ambiguities cause no problems. A typical pulse duration is about 10^{-4} sec, and a typical airborne target rotation rate is $\Omega = 10^\circ/\text{sec} \approx 1/6$ R/sec, so that for a target whose radius is about 100m, the distance traveled by points on the target during the pulse is about 10^{-3} m. This is much smaller than the range resolution of radar systems, and therefore the target can be considered stationary while the electromagnetic pulse interacts with it. On the other hand, to obtain different views of the target from different pulses, we do want to consider the motion of the target from pulse to pulse. Thus we use a model in which we imagine that the target moves only between pulses. This is the *start-stop* or *stop-and-shoot* approximation.

Typical ISAR systems remove the translational motion via tracking and *range alignment*, leaving only rotational motion. The range alignment process is discussed further in section 7.3.8 below.

7.3.2 Modeling Rotating Targets

We denote by q the target scattering density function in its own rest frame. Then the scattering density function seen by the radar is $V(\boldsymbol{x}) = q(\mathcal{O}(\theta_n)\boldsymbol{x})$, where $\mathcal{O}$ is an orthogonal matrix and where θ_n denotes the time at the start of the nth pulse.

For example, if the radar is in the plane perpendicular to the axis of rotation ("turntable geometry"), then the orthogonal matrix $\mathcal{O}$ can be written

$$\mathcal{O}(\theta) = \begin{pmatrix} \cos\theta & -\sin\theta & 0 \\ \sin\theta & \cos\theta & 0 \\ 0 & 0 & 1 \end{pmatrix}, \tag{7.7}$$

and $V(\boldsymbol{x}) = q(x_1\cos\theta - x_2\sin\theta, x_1\sin\theta + x_2\cos\theta, x_3)$.

7.3.3 Radar Data from Rotating Targets

Using $V(\boldsymbol{x}) = q\,(\mathcal{O}(\theta_n)\boldsymbol{x})$ in (7.6), we obtain a model for the data for the nth pulse as

$$D_B(\omega, \theta_n) \approx \frac{e^{2ik|\boldsymbol{x}^0|}}{(4\pi)^2|\boldsymbol{x}^0|^2} k^2 |P(\omega)|^2 \int e^{-2ik\hat{\boldsymbol{x}}^0\cdot\boldsymbol{z}} q(\underbrace{\mathcal{O}(\theta_n)\boldsymbol{z}}_{\boldsymbol{y}}) d\boldsymbol{z}. \tag{7.8}$$

In (7.8), we make the change of variables $\boldsymbol{y} = \mathcal{O}(\theta_n)\boldsymbol{z}$ and use the fact that the inverse of an orthogonal matrix is its transpose, which means that $\boldsymbol{x}^0 \cdot \mathcal{O}^{-1}(\theta_n)\boldsymbol{y} = \mathcal{O}(\theta_n)\boldsymbol{x}^0 \cdot \boldsymbol{y}$ (this might seem more familiar when the inner product is written in the notation $(\cdot,\cdot)$). We thus

obtain (7.8) in the form

$$D_B(\omega,\theta_n) = \frac{e^{2ik|\boldsymbol{x}^0|}}{(4\pi)^2|\boldsymbol{x}^0|^2}k^2|P(\omega)|^2 \underbrace{\int e^{-2ik\mathcal{O}(\theta_n)\hat{\boldsymbol{x}}^0\cdot\boldsymbol{y}}q(\boldsymbol{y})d\boldsymbol{y}}_{\propto\mathcal{F}[q](2k\mathcal{O}(\theta_n)\hat{\boldsymbol{x}}^0}). \tag{7.9}$$

Thus we see that the frequency-domain data are proportional to the inverse Fourier transform of q, evaluated at an angle determined by the target rotation angle.

7.3.4 The Data Collection Manifold

Figures 7.2 and 7.3 show examples of regions in Fourier space corresponding to $2k\mathcal{O}(\theta_n)\hat{\boldsymbol{x}}^0$. The region determined in this manner is called the *data collection manifold*.

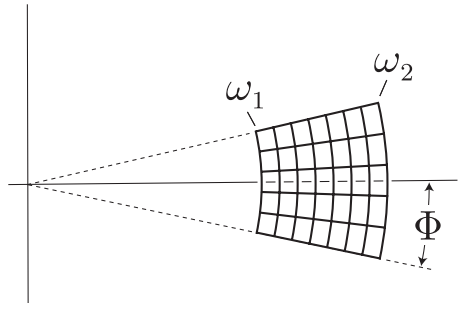

Figure 7.2. *The region Ω for turntable geometry.*

Figure 7.3 corresponds to a data set that was publicly released by the Air Force Research Laboratory (AFRL) for use by researchers testing imaging algorithms. This data set[8] was produced by the code XPATCH simulating radar returns from a backhoe (excavating equipment) floating in free space. The dark slice at the bottom of Figure 7.3 shows data from the turntable geometry. The dark bands within the slice show data that might be available if the transmit spectrum is restricted. The dark curve to the left of the center is an example of a curve over which an airborne platform might collect data. The research community is challenged to produce the best possible images from these data sets.

7.3.5 The Polar Format Algorithm (PFA)

For narrow-aperture, turntable-geometry data, such as shown in Figure 7.2, the Polar Format Algorithm (PFA) is commonly used. The PFA consists of the following steps, applied to frequency-domain data.

1. Interpolate from a polar grid to a rectangular grid (see Figure 7.4).
2. Use the two-dimensional fast (inverse) Fourier transform to form an image of q.

Alternatively, algorithms for computing the Fourier transform directly from a nonuniform grid can be used [59, 77, 106].

[8] available from https://www.sdms.afrl.af.mil/main.php.

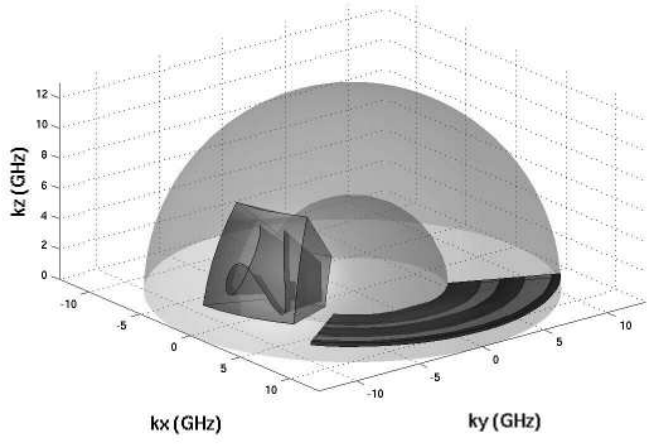

Figure 7.3. *This shows regions in Fourier space corresponding to the backhoe scattering data sets released by the Air Force Research Laboratory (courtesy of Air Force Research Laboratory Sensors Directorate).*

Examples of ISAR images are shown in Figures 7.5 and 7.6.

7.3.6 ISAR Resolution

To determine the resolution of an ISAR image, we analyze the relationship between the image and the target.

We consider the turntable geometry, for which we use (7.7). We take $\boldsymbol{x}^0 = (1, 0, 0)$ and write $\hat{\boldsymbol{e}}_\theta = \mathcal{O}(\theta)\boldsymbol{x}^0$ and $\tilde{k} = 2k$. Then (7.9) is proportional to

$$\begin{aligned}\tilde{D}(\tilde{k}, \theta) &= \int e^{-i\tilde{k}\hat{\boldsymbol{e}}_\theta \cdot \boldsymbol{y}} q(\boldsymbol{y}) d\boldsymbol{y} \\ &= \int e^{-i\tilde{k}(y_1 \cos\theta + y_2 \sin\theta)} \underbrace{\int q(y_1, y_2, y_3) dy_3}_{\tilde{q}(y_1, y_2)} dy_1 dy_2. \end{aligned} \tag{7.10}$$

We see that the data depend only on the quantity $\tilde{q}(y_1, y_2) = \int q(y_1, y_2, y_3) dy_3$, which is a projection of the target onto the plane orthogonal to the axis of rotation. In other words, in the turntable geometry, the radar imaging projection is the projection onto the horizontal plane. We write $\mathbf{y} = (y_1, y_2)$, so that $\boldsymbol{y} = (\mathbf{y}, y_3)$, and we note that in this geometry, $\hat{\boldsymbol{e}}_\theta \cdot \boldsymbol{y} = (\mathcal{P}\hat{\boldsymbol{e}}_\theta) \cdot \mathbf{y}$, where $\mathcal{P} : \mathbb{R}^3 \to \mathbb{R}^2$ denotes the projection onto the first two components of a three-dimensional vector.

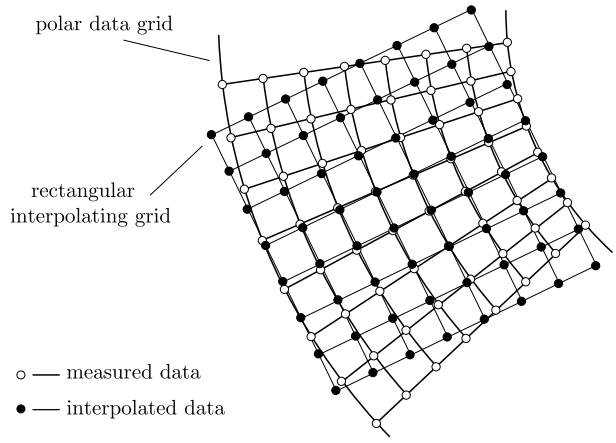

Figure 7.4. *This shows the process of interpolating from a polar grid to a rectangular grid.*

For resolution analysis, we consider the data corresponding to the set $\Omega = \{\tilde{k}\hat{\boldsymbol{e}}_\theta : \omega_1 < \omega < \omega_2 \text{ and } |\theta| < \Phi\}$, as shown in Figure 7.2. Then we can write (7.10) as

$$\tilde{D}(\tilde{k}, \theta) = \chi_\Omega(\tilde{k}\hat{\boldsymbol{e}}_\theta)\mathcal{F}[\tilde{q}](\tilde{k}\hat{\boldsymbol{e}}_\theta), \tag{7.11}$$

where $\chi_\Omega(\tilde{k}\hat{\boldsymbol{e}}_\theta)$ denotes the function that is 1 if $\tilde{k}\hat{\boldsymbol{e}}_\theta \in \Omega$ and 0 otherwise.

To form the image, we take the two-dimensional inverse Fourier transform of (7.11):

$$\begin{aligned} I(\mathbf{x}) = \int e^{i\mathbf{x}\cdot\tilde{k}(\mathcal{P}\hat{\boldsymbol{e}}_\theta)}\tilde{D}(\tilde{k},\theta)\tilde{k}d\tilde{k}d\theta \propto \int_\Omega e^{i\mathbf{x}\cdot\tilde{k}(\mathcal{P}\hat{\boldsymbol{e}}_\theta)} \int e^{-i\mathbf{y}\cdot\tilde{k}(\mathcal{P}\hat{\boldsymbol{e}}_\theta)}\tilde{q}(\mathbf{y})d\mathbf{y}\tilde{k}d\tilde{k}d\theta \\ = \int \underbrace{\int_\Omega e^{i(\mathbf{x}-\mathbf{y})\cdot\tilde{k}(\mathcal{P}\hat{\boldsymbol{e}}_\theta)}\tilde{k}d\tilde{k}d\theta}_{K(\mathbf{x}-\mathbf{y})}\,\tilde{q}(\mathbf{y})d\mathbf{y}. \end{aligned} \tag{7.12}$$

The function K is the *point-spread function (PSF)*; it is also called the *imaging kernel*, *impulse response*, or sometimes *ambiguity function*. The PSF can be written

$$K(\mathbf{x}) \propto \int_\Omega e^{i\mathbf{x}\cdot\tilde{k}(\mathcal{P}\hat{\boldsymbol{e}}_\theta)}\tilde{k}d\tilde{k}d\theta = \int_{|\boldsymbol{\xi}|=\tilde{k}_1}^{|\boldsymbol{\xi}|=\tilde{k}_2} \int_{-\Phi}^{\Phi} e^{i\mathbf{x}\cdot\tilde{k}(\mathcal{P}\hat{\boldsymbol{e}}_\theta)}\tilde{k}\,d\tilde{k}\,d\theta. \tag{7.13}$$

It can be calculated by writing

$$\mathbf{x} = r(\cos\psi, \sin\psi) \quad \text{and} \quad (\mathcal{P}\hat{\boldsymbol{e}}_\theta) = (\cos\phi, \sin\phi), \tag{7.14}$$

so that $\mathbf{x}\cdot(\mathcal{P}\hat{\boldsymbol{e}}_\theta) = r\cos(\phi - \psi)$. The "down-range" direction corresponds to $\psi = 0$, and "cross-range" corresponds to $\psi = \pi/2$.

Below we use the peak-to-null definition of resolution.

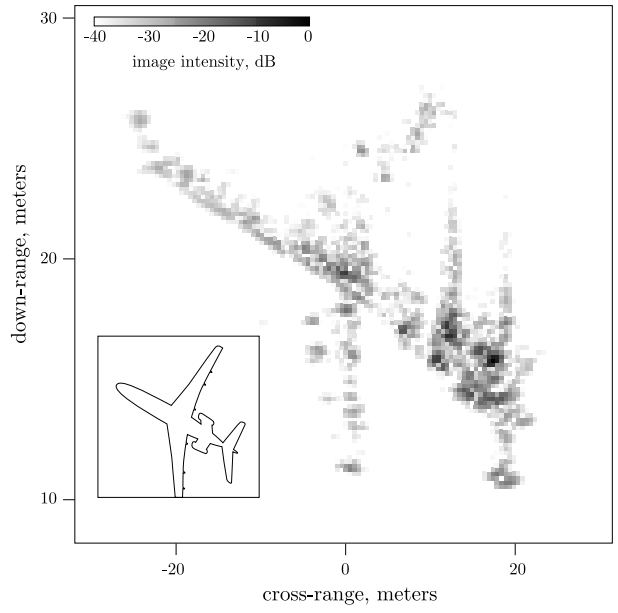

Figure 7.5. *An ISAR image of a Boeing 727 [135].*

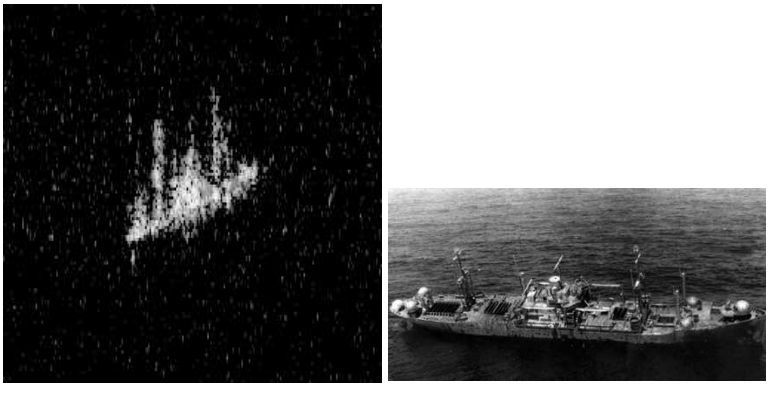

Figure 7.6. *On the left is an ISAR image of a ship; on the right is an optical image of the same ship (courtesy of Naval Research Laboratory).*

Down-range resolution in the small-angle case

For many radar applications, the target is viewed from only a small range of aspects $\hat{\boldsymbol{e}}_\theta$; in this case, we can use the small-angle approximations $\cos\phi \approx 1$ and $\sin\phi \approx \phi$.

In the down-range direction ($\psi = 0$), under the small-angle approximation, we obtain for (7.13)

$$\begin{aligned} K(r,0) &\approx \int_{\tilde{k}_1}^{\tilde{k}_2} \tilde{k} \int_{-\Phi}^{\Phi} e^{i\tilde{k}r}\, d\phi\, d\tilde{k} \\ &= 2\Phi \int_{\tilde{k}_1}^{\tilde{k}_2} \tilde{k} e^{i\tilde{k}r}\, d\tilde{k} = \frac{2\Phi}{i}\frac{d}{dr}\int_{\tilde{k}_1}^{\tilde{k}_2} e^{i\tilde{k}r}\, d\tilde{k} \\ &= \frac{2\Phi}{i}\frac{d}{dr}\left[e^{i\tilde{k}_0 r}\frac{b}{2}\mathrm{sinc}\frac{br}{2}\right], \end{aligned} \tag{7.15}$$

where $b = \tilde{k}_2 - \tilde{k}_1 = 4\pi B/c$, where B is the bandwidth in Hertz and $\tilde{k}_0 = (\tilde{k}_1 + \tilde{k}_2)/2 = 2\pi(\nu_1 + \nu_2) = 2\pi\nu_0$, where ν_0 is the center frequency in Hertz.

Since $\tilde{k}_0 \gg b$, the leading order term of (7.15) is obtained by differentiating the exponential:

$$K(r,0) \approx b\tilde{k}_0\Phi\, e^{i\tilde{k}_0 r}\mathrm{sinc}\frac{1}{2}br\,, \tag{7.16}$$

yielding peak-to-null down-range resolution $2\pi/b = c/(2B)$, which is the same as the resolution we obtained for the chirp in section 5.3.1. Here it is the sinc function that governs the resolution.

Cross-range resolution in the small-angle case

In the cross-range direction ($\psi = \pi/2$), we have $\cos(\phi - \psi) = \sin\phi$, which, under the small-angle approximation, is approximately ϕ. With this approximation, the computation of (7.13) is

$$\begin{aligned} K(0,r) &\approx \int_{\tilde{k}_1}^{\tilde{k}_2} \tilde{k} \int_{-\Phi}^{\Phi} e^{i\tilde{k}r\phi}\, d\phi\, d\tilde{k} \\ &= \int_{\tilde{k}_1}^{\tilde{k}_2} \tilde{k}\frac{e^{i\tilde{k}r\Phi} - e^{-i\tilde{k}r\Phi}}{i\tilde{k}r}\, d\tilde{k} \\ &= \frac{1}{ir}\left[e^{i\tilde{k}_0 r\Phi} b\mathrm{sinc}\left(\tfrac{1}{2}br\Phi\right) - e^{-i\tilde{k}_0 r\Phi} b\mathrm{sinc}\left(\tfrac{1}{2}br\Phi\right)\right] \\ &= 2b\tilde{k}_0\Phi\mathrm{sinc}\left(\tfrac{1}{2}br\Phi\right)\mathrm{sinc}(\tilde{k}_0 r\Phi)\,. \end{aligned} \tag{7.17}$$

Since $\tilde{k}_0 \gg b$, we have

$$K(0,r) \approx 2b\tilde{k}_0\Phi\mathrm{sinc}(\tilde{k}_0 r\Phi). \tag{7.18}$$

Thus we have peak-to-null cross-range resolution $\pi/(\tilde{k}_0\Phi) = c/(4\nu_0\Phi) = \lambda_0/(4\Phi)$. Since our angular aperture is 2Φ, this is consistent with our earlier observation in section 5.4.1 that cross-range resolution is λ_0 divided by twice the angular aperture. We note that it is precisely the oscillatory factor $\exp(i\tilde{k}_0 r)$ which is responsible for good cross-range resolution.

Example. Figure 7.7 shows a numerical calculation of K for $\phi = 12°$, and two different frequency bands: $[\tilde{k}_1, \tilde{k}_2] = [200, 300]$ (i.e., $b = 100$ and $\tilde{k}_0 = 250$) and $[\tilde{k}_1, \tilde{k}_2] = [0, 300]$ (i.e, $b = 300$ and $\tilde{k}_0 = 150$). The second case is not relevant for most radar systems, which do not transmit frequencies near zero, but is relevant for other imaging systems, such as X-ray tomography. These results are plotted in Figure 7.7.

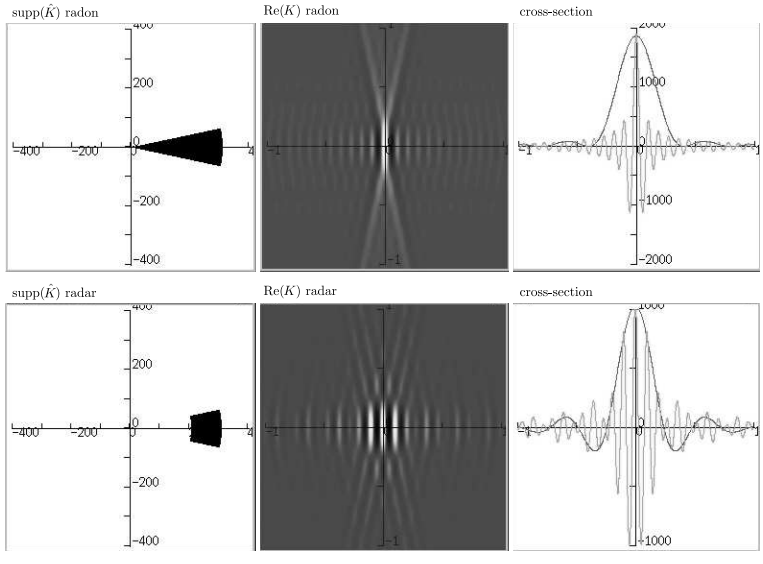

Figure 7.7. *From left to right: The data collection manifold, the real part of K, cross sections (horizontal is rapidly oscillating; vertical is slowly oscillating) through the real part of K for the two cases. Down-range is horizontal (reprinted with permission of the Institute of Physics from [88]).*

7.3.7 ISAR in the Time Domain

We Fourier transform (7.9) into the time domain, obtaining

$$\eta_B(t, \theta_n) \propto \int\int e^{-i\omega(t-2|\boldsymbol{x}^0|/c+2\mathcal{O}(\theta_n)\hat{\boldsymbol{x}}^0\cdot\boldsymbol{y}/c)}\omega^2|P(\omega)|^2 d\omega\, q(\boldsymbol{y})d\boldsymbol{y}. \tag{7.19}$$

If we evaluate η_B at a shifted time, we obtain the simpler expression

$$\eta_B\left(t + \frac{2|\boldsymbol{x}^0|}{c}, \theta_n\right) = \int\int e^{-i\omega(t+2\mathcal{O}(\theta_n)\hat{\boldsymbol{x}}^0\cdot\boldsymbol{y}/c)}\omega^2|P(\omega)|^2 d\omega\, q(\boldsymbol{y})d\boldsymbol{y}. \tag{7.20}$$

We temporarily write $\tau = -2\mathcal{O}(\theta_n)\boldsymbol{x}^0 \cdot \boldsymbol{y}/c$ and write the ω integral on the right side of (7.20) as

$$\int e^{-i\omega(t-\tau)}\omega^2|P(\omega)|^2 d\omega = \int \delta(s-\tau)\beta(t-s)\,ds, \tag{7.21}$$

where

$$\beta(t-s) = \int e^{-i\omega(t-s)}\omega^2|P(\omega)|^2 d\omega.$$

With (7.21), we can write η_B as

$$\begin{aligned}\eta_B\left(t + \frac{2|\boldsymbol{x}^0|}{c}, \theta_n\right) &= \int \beta(t-s)\int \delta\left(s + \frac{2\mathcal{O}(\theta_n)\hat{\boldsymbol{x}}^0}{c}\cdot \boldsymbol{y}\right) q(\boldsymbol{y})d\boldsymbol{y}\,ds \\ &= \beta * \mathcal{R}[q]\left(\frac{-2\mathcal{O}(\theta_n)\hat{\boldsymbol{x}}^0}{c}\right),\end{aligned}$$

where

$$\mathcal{R}[q](s, \widehat{\boldsymbol{\mu}}) = \int \delta(s - \widehat{\boldsymbol{\mu}}\cdot \boldsymbol{y})q(\boldsymbol{y})d\boldsymbol{y} \tag{7.22}$$

is the *Radon transform*. Here $\widehat{\boldsymbol{\mu}}$ denotes a unit vector. In other words, the Radon transform of q is defined as the integral of q over the plane $s = \hat{\boldsymbol{\mu}}\cdot \boldsymbol{y}$.

ISAR systems typically use a high-range-resolution waveform, so that $\beta \approx \delta$. Thus ISAR imaging from time-domain data becomes a problem of inverting the Radon transform.

The Radon transform

Because the Radon transform arises in X-ray tomography, it has been thoroughly studied [87, 89]. We write $\mathcal{R}_{\widehat{\boldsymbol{\mu}}}[q](s) = \mathcal{R}[q](s, \widehat{\boldsymbol{\mu}})$.

Some of the main properties of the Radon transform are as follows.

- **The Projection-Slice Theorem**:

$$\mathcal{F}_{s\to\sigma}(\mathcal{R}_{\widehat{\boldsymbol{\mu}}}[f])(\sigma) = (2\pi)^{1-n}\mathcal{F}_n[f](\sigma\widehat{\boldsymbol{\mu}}), \tag{7.23}$$

  where $\mathcal{F}$ on the left side denotes a one-dimensional Fourier transform in the s variable and where $\mathcal{F}$ on the right side denotes an n-dimensional Fourier transform.[9] The result (7.23) follows from the calculation

$$\begin{aligned}\mathcal{F}_{s\to\sigma}(\mathcal{R}_{\widehat{\boldsymbol{\mu}}}[f])(\sigma) &= \frac{1}{2\pi}\int e^{-is\sigma}(\mathcal{R}_{\widehat{\boldsymbol{\mu}}}[f])(s)ds \\ &= \frac{1}{2\pi}\int e^{-is\sigma}\int\left(\frac{1}{2\pi}\int e^{-i\omega(s-\widehat{\boldsymbol{\mu}}\cdot\boldsymbol{x})}d\omega\right) f(\boldsymbol{x})d\boldsymbol{x}ds \\ &= \frac{1}{2\pi}\int \delta(\omega-\sigma)e^{-i\omega\widehat{\boldsymbol{\mu}}\cdot\boldsymbol{x}} f(\boldsymbol{x})d\boldsymbol{x}d\omega \\ &= \frac{1}{2\pi}\int e^{-i\sigma\widehat{\boldsymbol{\mu}}\cdot\boldsymbol{x}} f(\boldsymbol{x})d\boldsymbol{x} = \frac{1}{(2\pi)^{n-1}}\mathcal{F}_n[f](\sigma\widehat{\boldsymbol{\mu}}),\end{aligned} \tag{7.24}$$

  where we have again used (8) in the second and third lines.

[9] Here we use convention (6).

- **Inversion by Filtered Backprojection**: For the n-dimensional Radon transform, one of the many inversion formulas [87, 89] is

$$f = \frac{1}{2(2\pi)^{n-1}} \mathcal{R}^\dagger \mathcal{I}^{1-n} \left(\mathcal{R}[f]\right), \tag{7.25}$$

where $\mathcal{I}^{1-n}$ is the filter (2.12) operating on the s variable and the operator $\mathcal{R}^\dagger$ is the formal[10] adjoint of $\mathcal{R}$. The adjoint is defined by the relation

$$\langle \mathcal{R}f, h\rangle_{s,\widehat{\boldsymbol{\mu}}} = \langle f, \mathcal{R}^\dagger h\rangle_{\boldsymbol{x}}, \tag{7.26}$$

where

$$\langle \mathcal{R}f, h\rangle_{s,\widehat{\boldsymbol{\mu}}} = \iint \mathcal{R}(s, \widehat{\boldsymbol{\mu}}) h^*(s, \widehat{\boldsymbol{u}}) ds d\widehat{\boldsymbol{\mu}} \tag{7.27}$$

and

$$\langle f, \mathcal{R}^\dagger h\rangle_{\boldsymbol{x}} = \int f(\boldsymbol{x})[\mathcal{R}^\dagger h]^*(\boldsymbol{x}) d\boldsymbol{x}.$$

Using (7.22) in (7.27) and interchanging the order of integration shows that the adjoint $\mathcal{R}^\dagger$ operates on $h(s, \boldsymbol{\mu})$ via

$$(R^\dagger h)(\boldsymbol{x}) = \int_{S^{n-1}} h(\boldsymbol{x} \cdot \widehat{\boldsymbol{\mu}}, \widehat{\boldsymbol{\mu}}) d\widehat{\boldsymbol{\mu}}. \tag{7.28}$$

Here $\mathcal{R}^\dagger$ integrates over the part of h corresponding to all planes ($n = 3$) or lines ($n = 2$) through $\boldsymbol{x}$. When it operates on Radon data, $\mathcal{R}^\dagger$ has the physical interpretation of *backprojection*. To understand this, we consider the case where h represents Radon data from a point-like target. First, we note that, for a fixed direction $\hat{\boldsymbol{\mu}}$, the quantity $h(\boldsymbol{x} \cdot \widehat{\boldsymbol{\mu}}, \widehat{\boldsymbol{\mu}})$, as a function of $\boldsymbol{x}$, is constant along each plane (or line if $n = 2$) $\boldsymbol{x} \cdot \hat{\boldsymbol{\mu}} =$ constant. Thus, at each $\hat{\boldsymbol{\mu}}$, the function $h(\boldsymbol{x} \cdot \widehat{\boldsymbol{\mu}}, \widehat{\boldsymbol{\mu}})$ can be thought of as an image in which the data h for direction $\hat{\boldsymbol{u}}$ is backprojected (smeared) onto all points $\boldsymbol{x}$ that could have produced the data for that direction. The integral in (7.28) then sums the contributions from all the possible directions. (See Figure 7.8.) The inversion formula (7.25) is thus a *filtered backprojection* formula.

7.3.8 Range Alignment

We have seen that ISAR imaging relies on target/radar relative motion. From elementary physics we know that rigid body motion[11] can always be separated into a rotation about the body's center of mass and a translation of that center of mass. Backprojection shows us how the rotation part of the relative radar/target motion can be used to reconstruct a two-dimensional image of the target in ISAR and spotlight SAR. But, usually while the target is rotating and we are collecting our data, *it will also be translating*—and we haven't accounted for that in our imaging algorithm.

[10] Here the term "formal" means that we do not worry about convergence of the integrals; we consider only functions that decay sufficiently rapidly so that the integrals converge.

[11] We have implicitly assumed throughout that the target moves as a rigid body—an assumption that ignores the flexing of aircraft lift and control surfaces, or the motion of vehicle treads.

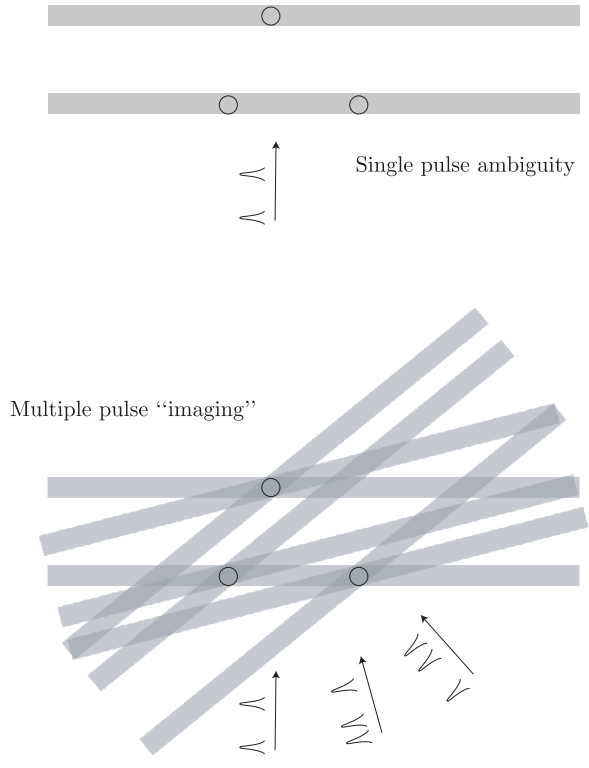

Figure 7.8. *This illustrates the process of backprojection. The small blips suggest the time delays that would result from an interrogating radar pulse incident from the indicated direction. Note that scatterers that lie at the same range from one view do* not *lie at the same range from other views.*

Typically the radar data are preprocessed to subtract the effects of target translation before the imaging step is performed. Under the start-stop approximation we can consider our range profile data $\eta_B(t, \theta_n)$ to be approximately a shifted version of the range profile at the previous pulse. Thus $\eta_B(t, \theta_{n+1}) \approx \eta_B(t + \Delta t_n, \theta_n)$, where Δt_n is a range offset that is determined by target motion between pulses.

The collected range profiles can be shifted to a common origin if we can determine Δt_n for each θ_n. One method to accomplish this is to assume that one of the peaks in each of the range profiles (for example, the strongest peak) is always due to the *same* target feature and so provides a convenient origin. This correction method is known as "range alignment" and must be very accurate in order to correct the offset error to within a fraction of a wavelength.[12] Typically, $\eta_B(t + \Delta t_n, \theta_n)$ is correlated with $\eta_B(t, \theta_{n+1})$, and the correlation

[12]Note that the wavelength in question is that of the signal output by the correlation receiver (see Figure 2.2) and not the wavelength of the transmitted waveform. In HRR systems, however, this wavelength can still be quite small.

maximum is taken to indicate the size of the shift Δt_n. This idea is illustrated in Figure 7.9, which displays a collection of properly aligned range profiles.

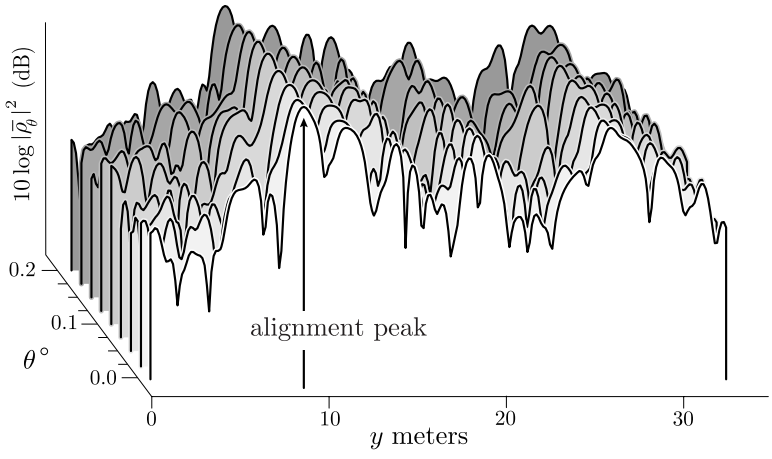

Figure 7.9. *Range alignment preprocessing in synthetic aperture imaging. The effects of target translation must be removed before backprojection can be applied.*

Chapter 8

Antennas

For imaging objects on the earth, we need to understand how an antenna radiates and how it can form a beam.

8.1 Examples

There are many different types and shapes of antennas; see Figures 8.1–8.18.

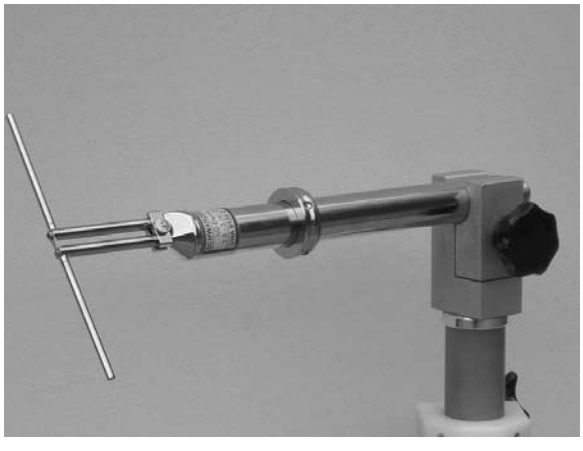

Figure 8.1. *A dipole antenna. The radiating element is at the left; the structures on the right couple the antenna to the transmitter. A dipole antenna is one of the simplest to analyze (courtesy of Schwarzbeck Mess-Elektronik).*

Antennas tend to radiate efficiently at frequencies for which the wavelength is on the same order as the dimensions of the antenna. Many antennas are designed with complicated shapes in an attempt to make them radiate in roughly the same way over a broad band of frequencies.

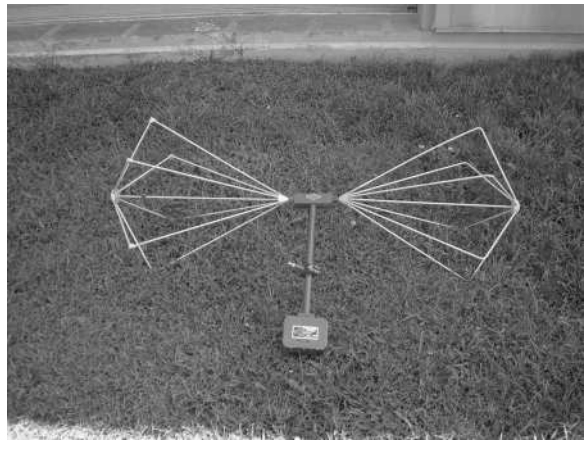

Figure 8.2. *A biconical antenna (courtesy of Air Force Research Laboratory Sensors Directorate).*

Figure 8.3. *A loop antenna (courtesy of Air Force Research Laboratory Sensors Directorate).*

Fractal antennas, for example, are of great interest because the range of length scales tends to give rise to a broadband antenna. In addition, designing antennas as space-filling curves may allow antennas to be small in overall size yet behave electrically as if they are large.

8.2 Scalar and Vector Potentials

To understand the radiation from an antenna, it is helpful to use a somewhat different formulation of Maxwell's equations. This is the formulation in terms of vector and scalar potentials.

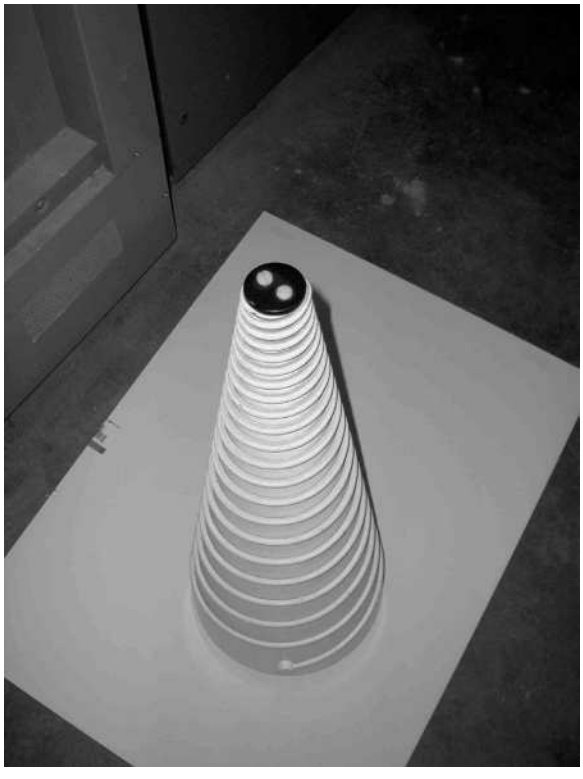

Figure 8.4. *A conical spiral antenna (courtesy of Air Force Research Laboratory Sensors Directorate).*

Figure 8.5. *A spiral antenna (courtesy of North American Astronomical Observatory).*

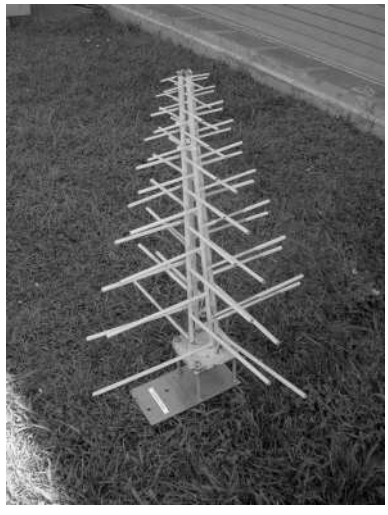

Figure 8.6. *A dual-polarized log-periodic antenna (courtesy of Air Force Research Laboratory Sensors Directorate).*

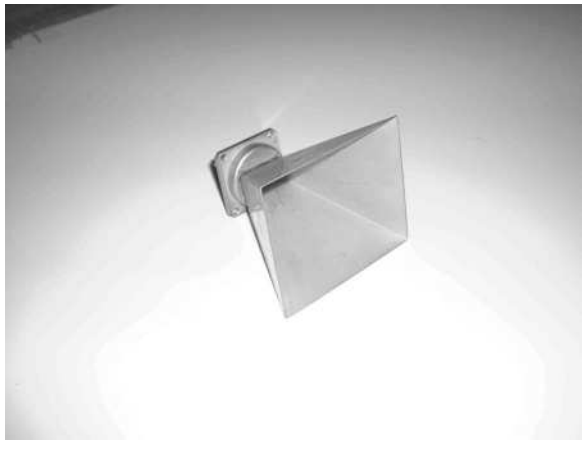

Figure 8.7. *A horn antenna (courtesy of Air Force Research Laboratory Sensors Directorate).*

In the frequency domain, Maxwell's equations are

$$\nabla \times \boldsymbol{E}(\omega, \boldsymbol{x}) = i\omega \boldsymbol{B}(\omega, \boldsymbol{x}), \tag{8.1}$$

$$\nabla \times \boldsymbol{H}(\omega, \boldsymbol{x}) = \boldsymbol{J}(\omega, \boldsymbol{x}) - i\omega \boldsymbol{D}(\omega, \boldsymbol{x}), \tag{8.2}$$

$$\nabla \cdot \boldsymbol{D}(\omega, \boldsymbol{x}) = \rho(\omega, \boldsymbol{x}), \tag{8.3}$$

$$\nabla \cdot \boldsymbol{B}(\omega, \boldsymbol{x}) = 0. \tag{8.4}$$

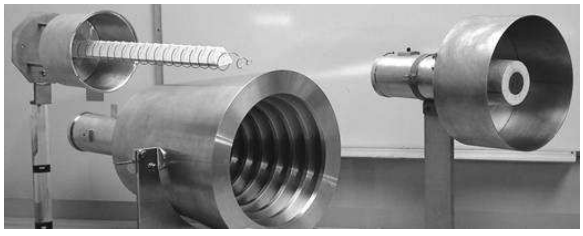

Figure 8.8. *Prototype antennas designed, developed, and measured at the NASA Glenn Research Center. From left: Helix antenna, corrugated horn antenna, and waveguide-excited short backfire antenna (courtesy of NASA Glenn Research Center).*

Figure 8.9. *An L-band reflector antenna (courtesy of Air Force Research Laboratory Sensors Directorate).*

Since a vector field whose divergence is zero can be written as the curl of another vector field, we see that the no-magnetic-monopole law (8.4) implies that the magnetic induction field can be written as the curl of another field $\boldsymbol{A}$ called the *vector potential*:

$$\boldsymbol{B} = \nabla \times \boldsymbol{A}. \tag{8.5}$$

With this notation we can write Faraday's law (8.1) as

$$\nabla \times \boldsymbol{E} - i\omega \nabla \times \boldsymbol{A} = 0. \tag{8.6}$$

This equation says that the curl of the quantity $\boldsymbol{E} - i\omega \boldsymbol{A}$ is zero. But a vector field whose curl is zero can be written as the gradient of a potential. Thus there is some scalar field Φ called the *scalar potential* for which[13]

$$\boldsymbol{E} - i\omega \boldsymbol{A} = -\nabla \Phi. \tag{8.7}$$

[13]Here the minus sign is merely a convention.

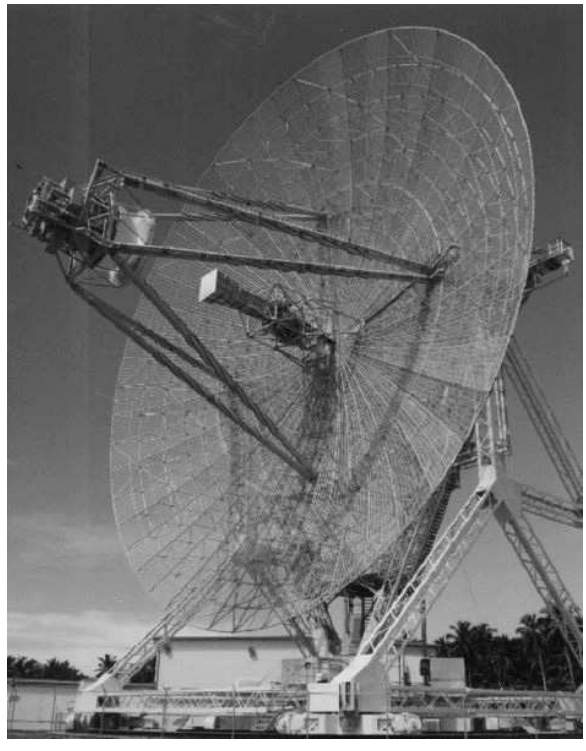

Figure 8.10. *A Cassegrain reflector antenna. A Cassegrain antenna involves a feed (the rectangular horn in the center) aimed at a secondary convex reflector (at the left in the image) and a concave main reflector. This antenna is part of the ARPA Long-Range Tracking and Instrumentation Radar (ALTAIR) located in the Kwajalein atoll on the island of Roi-Namur (courtesy of U.S. Department of Defense).*

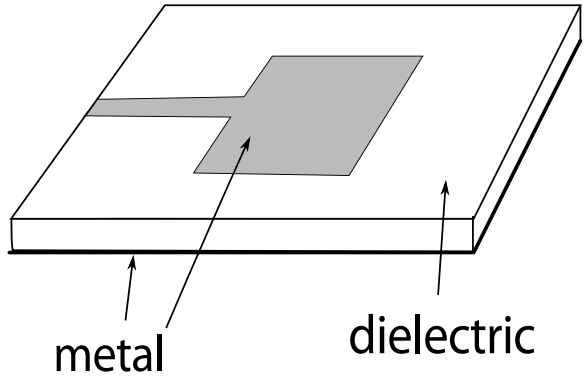

Figure 8.11. *A diagram of a microstrip antenna.*

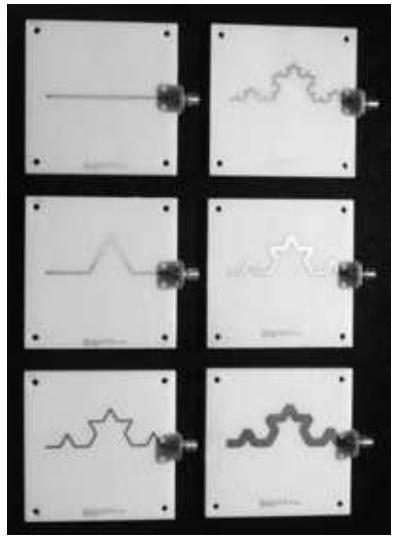

Figure 8.12. *Microstrip antennas with the shape of successive steps in the construction of a Koch curve (courtesy of LEMA-EPFL Switzerland).*

This equation can be solved for $\boldsymbol{E}$, and the resulting expression can be used in (8.2) and (8.3) to obtain one vector equation and one scalar equation for the vector and scalar potentials. This is a system of four scalar equations in four unknowns, which seems significantly simpler than the original Maxwell's equations. For the case of a source in free space, where we use (1.5), these four scalar equations are

$$\nabla \times \left(\mu_0^{-1} \nabla \times \boldsymbol{A}\right) = \boldsymbol{J} - i\omega\epsilon_0 \left(i\omega \boldsymbol{A} - \nabla\Phi\right), \tag{8.8}$$

$$\epsilon_0 \nabla \cdot \left(i\omega \boldsymbol{A} - \nabla\Phi\right) = \rho. \tag{8.9}$$

However, there is a complication. Adding the gradient of any scalar vector field ψ to the vector potential $\boldsymbol{A}$ leaves the physical magnetic induction field $\boldsymbol{B}$ unchanged (because the curl of a gradient is always zero). If, in addition, $i\omega\psi$ is also added to the scalar potential Φ, then the electric field $\boldsymbol{E}$ is left unchanged, as can be seen easily from (8.7). Thus the transformation

$$\begin{aligned} \boldsymbol{A} &\rightarrow A + \nabla\psi, \\ \Phi &\rightarrow \Phi + i\omega\psi \end{aligned} \tag{8.10}$$

leaves the physical fields unchanged. Such a transformation is called a *gauge transformation*.

There are two gauges that are frequently used for solving problems in free space:

- The Coulomb gauge, in which we use the added condition $\nabla \cdot \boldsymbol{A} = 0$.

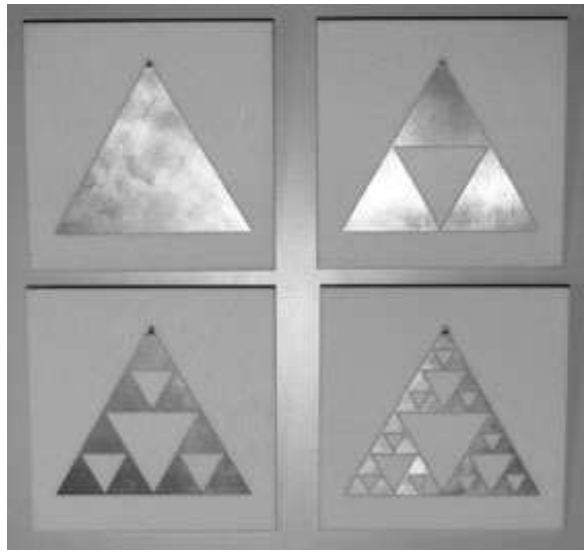

Figure 8.13. *Microstrip antennas in the form of a Sierpinski gasket (courtesy of LEMA-EPFL Switzerland).*

Figure 8.14. *An array antenna (courtesy of Air Force Research Laboratory, Sensors Directorate).*

- The Lorenz[14] gauge, in which we use the added condition

$$\nabla \cdot \boldsymbol{A} - i\omega\epsilon_0\mu_0\Phi = 0. \tag{8.11}$$

For radiation from an antenna, we use the Lorenz gauge.

[14]Danish physicist Ludvig Valentin Lorenz formulated this condition in 1867. The Dutch physicist Hendrik Antoon Lorentz also discovered the same condition at a later date [10].

Figure 8.15. *The PAVE PAWS antenna, part of the Ballistic Missile Early Warning System in Alaska (courtesy of U.S. Department of Defense).*

Figure 8.16. *A microstrip antenna that fits into an aerodynamic structure. Such antennas are called* conformal *antennas (courtesy of Ball Aerospace).*

In (8.8) we use (9) and collect the gradient terms on the right side. This gives us

$$\nabla^2 \boldsymbol{A} + k^2 \boldsymbol{A} = -\mu_0 \boldsymbol{J} + \nabla(\nabla \cdot \boldsymbol{A} - i\omega\epsilon_0\mu_0\Phi), \tag{8.12}$$

where $k^2 = \omega^2\mu_0\epsilon_0$. But the term in parentheses on the right side is precisely the expression (8.11) defining the Lorenz gauge, and is zero. Thus, for a source in free space, Ampère's law reduces to three uncoupled scalar wave equations with source terms:

$$\boxed{\nabla^2 \boldsymbol{A} + k^2 \boldsymbol{A} = -\mu_0 \boldsymbol{J}.} \tag{8.13}$$

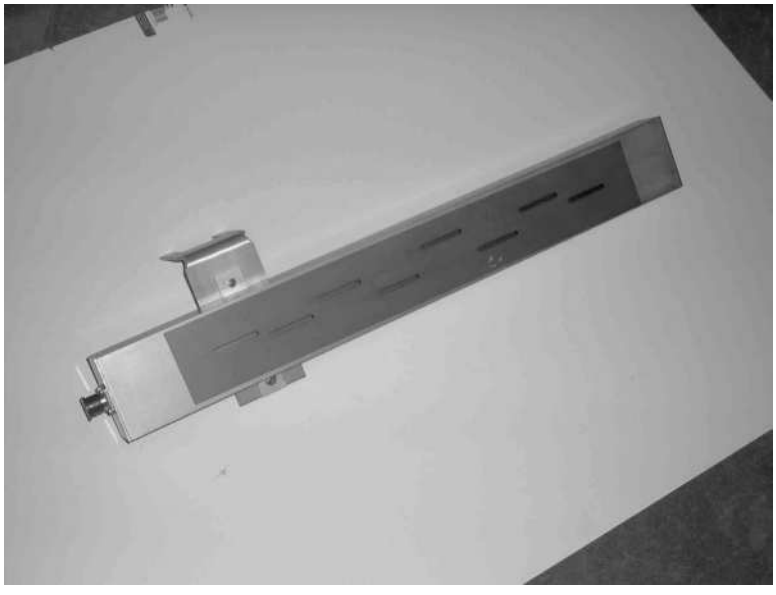

Figure 8.17. *A slotted waveguide antenna. An electromagnetic field in a cavity under the metal plate escapes through the slots to radiate (courtesy of Air Force Research Laboratory Sensors Directorate).*

If we use (8.11) to eliminate $\boldsymbol{A}$ in (8.9), we obtain

$$\boxed{\nabla^2\Phi + k^2\Phi = -\rho/\epsilon_0.} \tag{8.14}$$

Thus, in the Lorenz gauge, the free-space Maxwell's equations reduce to the set (8.13), (8.14) of uncoupled Helmholtz equations with source terms.

From section 6.2, we know how to solve Helmholtz equations with source terms! The outgoing solutions of (8.13), (8.14) are

$$\boldsymbol{A}(k, \boldsymbol{x}) = \mu_0 \int \frac{e^{ik|\boldsymbol{x}-\boldsymbol{y}|}}{4\pi|\boldsymbol{x}-\boldsymbol{y}|} \boldsymbol{J}(\boldsymbol{\omega}, \boldsymbol{y}) d\boldsymbol{y}, \tag{8.15}$$

$$\Phi(k, \boldsymbol{x}) = \frac{1}{\epsilon_0} \int \frac{e^{ik|\boldsymbol{x}-\boldsymbol{y}|}}{4\pi|\boldsymbol{x}-\boldsymbol{y}|} \rho(\omega, \boldsymbol{y}) d\boldsymbol{y}. \tag{8.16}$$

8.3 Fields Far from the Antenna

The strategy for analysis of the radiation from an antenna is as follows.

1. We model the antenna as a current density $\boldsymbol{J}$. Even for antennas such as horns and slotted waveguides, where it might seem more natural to use the electric field, we convert the field to an *effective* current density on the relevant aperture.

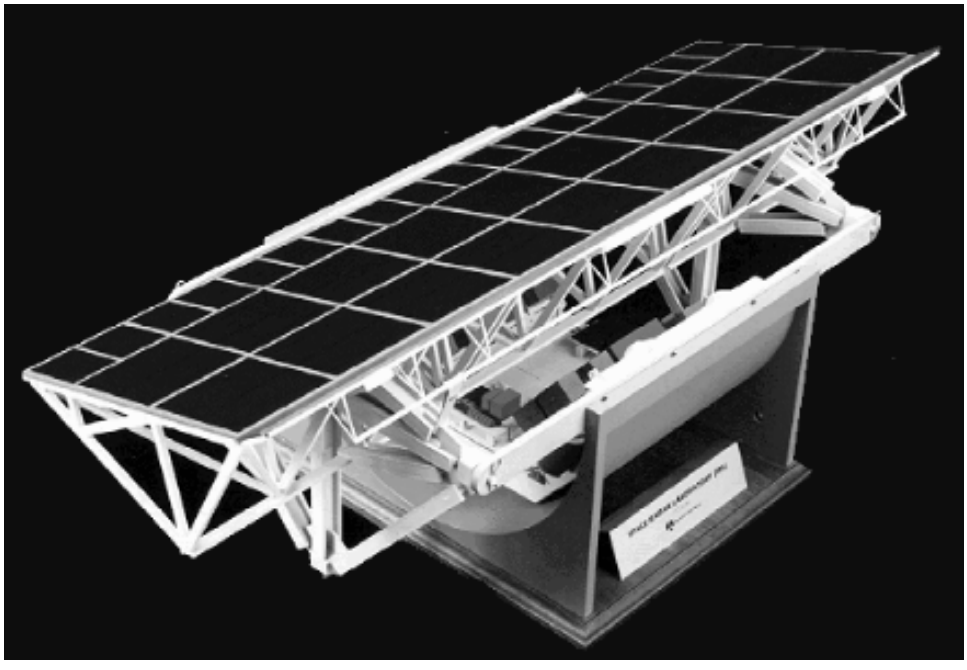

Figure 8.18. *The antenna on NASA's Spaceborne Imaging Radar-C/X-band Synthetic Aperture Radar mission. It consists of three antennas, one operating at L band, one at C band, and one at X band. The X-band antenna is a slotted waveguide array; the others are microstrip arrays. The X-band antenna must be tilted to change its direction; the L- and C-band antennas can be steered electronically (courtesy of NASA/JPL-Caltech).*

2. We solve solve (8.13) for $\boldsymbol{A}$, obtaining (8.15), and then use the far-field expansion (7.1), taking the origin of coordinates to be on or near the antenna. We obtain

$$\begin{aligned}\boldsymbol{A}(k,\boldsymbol{x}) &= \int \frac{e^{ik|\boldsymbol{x}-\boldsymbol{y}|}}{4\pi|\boldsymbol{x}-\boldsymbol{y}|}\mu_0 \boldsymbol{J}(\omega,\boldsymbol{y})d\boldsymbol{y} \\ &\approx \frac{e^{ik|\boldsymbol{x}|}}{4\pi|\boldsymbol{x}|}\mu_0 \underbrace{\int e^{-ik\widehat{\boldsymbol{x}}\cdot\boldsymbol{y}}\boldsymbol{J}(\omega,\boldsymbol{y})d\boldsymbol{y}}_{\boldsymbol{F}(k,\widehat{\boldsymbol{x}})=\mathcal{F}[\boldsymbol{J}](k,\widehat{\boldsymbol{x}})} = \frac{e^{ik|\boldsymbol{x}|}}{4\pi|\boldsymbol{x}|}\mu_0 \boldsymbol{F}(k,\widehat{\boldsymbol{x}}),\end{aligned} \tag{8.17}$$

where $\boldsymbol{F}$ is the *radiation vector*. We note that it is the Fourier transform of the current density.

3. We obtain $\boldsymbol{H}$ from $\boldsymbol{A}$ via (8.5) and (1.5).

4. To obtain $\boldsymbol{E}$ from $\boldsymbol{A}$, we solve (8.11) for Φ and use the result in (8.7), thus obtaining

$$\boldsymbol{E} = i\omega\left[\boldsymbol{A} + k^{-2}\nabla(\nabla\cdot\boldsymbol{A})\right]. \tag{8.18}$$

5. We express the gradient operator in spherical coordinates:

$$\nabla = \widehat{\boldsymbol{r}}\frac{\partial}{\partial r} + \widehat{\boldsymbol{\theta}}\frac{1}{r}\frac{\partial}{\partial \theta} + \widehat{\boldsymbol{\phi}}\frac{1}{r\sin\theta}\frac{\partial}{\partial \phi}, \tag{8.19}$$

where $r = |\boldsymbol{x}|$ and $\widehat{\boldsymbol{r}} = \widehat{\boldsymbol{x}}$. We note that the angular derivatives involve an extra factor of $1/r = 1/|\boldsymbol{x}|$ and therefore can be neglected in the leading-order large-$|\boldsymbol{x}|$ expression; the same holds for the curl operator and divergence operator. In particular, we have

$$\begin{aligned}\nabla \cdot \left[\frac{e^{ik|\boldsymbol{x}|}}{k|\boldsymbol{x}|}\boldsymbol{F}(k,\widehat{\boldsymbol{x}})\right] &= \boldsymbol{F}(k,\widehat{\boldsymbol{x}}) \cdot \nabla\left(\frac{e^{ik|\boldsymbol{x}|}}{k|\boldsymbol{x}|}\right) \\ &= ik\widehat{\boldsymbol{x}} \cdot \boldsymbol{F}(k,\widehat{\boldsymbol{x}})\frac{e^{ik|\boldsymbol{x}|}}{k|\boldsymbol{x}|}\left[1 + \mathcal{O}\left(\frac{1}{k|\boldsymbol{x}|}\right)\right]\end{aligned} \tag{8.20}$$

and

$$\begin{aligned}\nabla\left[\nabla \cdot \left(\frac{e^{ik|\boldsymbol{x}|}}{k|\boldsymbol{x}|}\boldsymbol{F}(k,\widehat{\boldsymbol{x}})\right)\right] &= \nabla\left[ik\widehat{\boldsymbol{x}} \cdot \boldsymbol{F}(k,\widehat{\boldsymbol{x}})\frac{e^{ik|\boldsymbol{x}|}}{k|\boldsymbol{x}|}\left[1 + \mathcal{O}\left(\frac{1}{k|\boldsymbol{x}|}\right)\right]\right] \\ &= ik\widehat{\boldsymbol{x}}\,(ik\widehat{\boldsymbol{x}} \cdot \boldsymbol{F}(k,\widehat{\boldsymbol{x}}))\,\frac{e^{ik|\boldsymbol{x}|}}{k|\boldsymbol{x}|}\left[1 + \mathcal{O}\left(\frac{1}{k|\boldsymbol{x}|}\right)\right].\end{aligned} \tag{8.21}$$

We see that we simply replace ∇ in (8.5) and (8.18) by $ik\widehat{\boldsymbol{x}}$ to obtain the leading-order terms in the far field.

6. We obtain the leading-order large-$|\boldsymbol{x}|$ term from (8.18) and (8.17):

$$\boxed{\boldsymbol{E}_{\text{rad}}(\omega,\boldsymbol{x}) = i\omega\mu_0\frac{e^{ik|\boldsymbol{x}|}}{4\pi|\boldsymbol{x}|}\left[\boldsymbol{F} - \widehat{\boldsymbol{x}}(\widehat{\boldsymbol{x}} \cdot \boldsymbol{F})\right], = i\omega\mu_0\frac{e^{ik|\boldsymbol{x}|}}{4\pi|\boldsymbol{x}|}\left[\widehat{\boldsymbol{x}} \times (\widehat{\boldsymbol{x}} \times \boldsymbol{F})\right],} \tag{8.22}$$

where we have used the "BAC-CAB" vector identity (10), together with $k^2 = \omega^2/c_0^2 = \mu_0\epsilon_0\omega^2$. We see that one effect of going to the far field is that the longitudinal component of $\boldsymbol{E}$ is removed, so that $\boldsymbol{E}$ is perpendicular to $\widehat{\boldsymbol{x}}$, which as we saw in (1.8), must be true for a plane wave propagating in direction $\widehat{\boldsymbol{x}}$.

Thus the end result is

$$\boldsymbol{H}_{\text{rad}} = i\frac{e^{ik|\boldsymbol{x}|}}{4\pi|\boldsymbol{x}|}(k\widehat{\boldsymbol{x}} \times \boldsymbol{F}) \quad \text{and} \quad \boldsymbol{E}_{\text{rad}} = i\omega\mu_0\frac{e^{ik|\boldsymbol{x}|}}{4\pi|\boldsymbol{x}|}\widehat{\boldsymbol{x}} \times (\widehat{\boldsymbol{x}} \times \boldsymbol{F}). \tag{8.23}$$

We note that obtaining expression (8.22) required *three* far-field conditions:

1. $|\boldsymbol{x}| \gg L$,
2. $|\boldsymbol{x}| \gg kL^2$, and
3. $|\boldsymbol{x}| \gg 1/k$,

where L denotes the maximum magnitude of a point $\boldsymbol{y}$ on the antenna. The third condition is needed only in the vector case.

8.4 Examples

8.4.1 A Short Linear Antenna

For an antenna consisting of a wire that is short relative to the wavelength, the current density is approximately constant along the antenna. If we consider the antenna to be a line in space, say, the set of points $\boldsymbol{x}(s) = s\widehat{\boldsymbol{e}}$ with $-L/2 \le s \le L/2$, and denote the current density by the constant vector $I\widehat{\boldsymbol{e}}$, then the radiation vector is

$$\begin{aligned}\boldsymbol{F}(k,\widehat{\boldsymbol{x}}) &= \int_{-L/2}^{L/2} e^{-ik\widehat{\boldsymbol{x}}\cdot(s\widehat{\boldsymbol{e}})} I\widehat{\boldsymbol{e}}\,ds = I\widehat{\boldsymbol{e}}\frac{e^{-ikL\widehat{\boldsymbol{x}}\cdot\widehat{\boldsymbol{e}}/2} - e^{ikL\widehat{\boldsymbol{x}}\cdot\widehat{\boldsymbol{e}}/2}}{ik\widehat{\boldsymbol{x}}\cdot\widehat{\boldsymbol{e}}} \\ &= -I\widehat{\boldsymbol{e}}\frac{2i\sin(kL\widehat{\boldsymbol{x}}\cdot\widehat{\boldsymbol{e}}/2)}{ik\widehat{\boldsymbol{x}}\cdot\widehat{\boldsymbol{e}}} = -LI\widehat{\boldsymbol{e}}\,\mathrm{sinc}(kL\widehat{\boldsymbol{x}}\cdot\widehat{\boldsymbol{e}}/2). \end{aligned} \tag{8.24}$$

Because the first zero of the sinc function occurs when the argument is equal to π, half the width of the main lobe of the radiation vector is obtained from $kL\widehat{\boldsymbol{x}}\cdot\widehat{\boldsymbol{e}}/2 = \pi$. It is conventional to write $\widehat{\boldsymbol{x}}\cdot\widehat{\boldsymbol{e}} = \sin\theta$, where θ is measured from the normal. For a narrow beam, we can use the approximation $\sin\theta \approx \theta$, and obtain an expression for half the beamwidth as

$$\theta \approx \frac{2\pi}{kL} = \frac{2\pi}{(2\pi/\lambda)L} = \frac{\lambda}{L} = \frac{1}{\text{number of wavelengths that fit on antenna}}, \tag{8.25}$$

where we have used $k = 2\pi/\lambda$. The full beamwidth is twice (8.25):

$$\boxed{\text{beamwidth} = \frac{2\lambda}{L}.} \tag{8.26}$$

Thus we see that a shorter wavelength compared to the size of the antenna gives rise to a narrower beam.

Once $\boldsymbol{F}$ is known, it is used in (8.22) to obtain the electric field in the far-field. The polarization $\hat{\boldsymbol{E}}$ of the resulting electric field depends on the viewing direction $\hat{\boldsymbol{x}}$ as $\hat{\boldsymbol{E}} = \hat{\boldsymbol{x}} \times (\hat{\boldsymbol{x}} \times \hat{\boldsymbol{e}}) \propto \hat{\boldsymbol{e}} - (\hat{\boldsymbol{e}}\cdot\hat{\boldsymbol{x}})\hat{\boldsymbol{x}}$.

8.4.2 Radiation from an Aperture

In the case of radiation from an aperture such as a horn or an opening in a waveguide, there is no current flowing on the aperture. Rather, in the aperture there is an electromagnetic field, which has propagated from the waveguide attached to the horn to the horn opening. A common practice of antenna design engineers is to replace the distribution of fields over the aperture with an "equivalent current distribution" derived from the frequency-domain version of (1.9), namely,

$$\boldsymbol{J}_{\text{equiv}}(\omega,\boldsymbol{x}) \equiv \widehat{\boldsymbol{n}} \times \boldsymbol{H}(\omega,\boldsymbol{x}),$$

where $\widehat{\boldsymbol{n}}$ is normal to the (nonexistent) aperture surface and directed toward the radiated field. Then we can make use of all the previously developed machinery for radiation from a current density. This approach is called the "field equivalence principle."

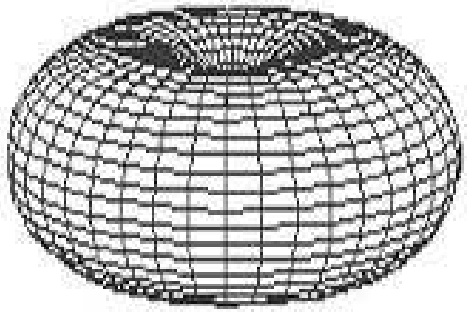

Figure 8.19. *The radiation pattern $|\boldsymbol{E}|$ for a short linear antenna.*

The standard approximation in this calculation is that the aperture field *is the same as the one that would exist if the opening in the waveguide did not exist.* This means that once the fields in the waveguide or horn are determined, the radiated field can be calculated in a straightforward manner.

In the case in which the field $\boldsymbol{H}$ is constant over an aperture $[-a, a] \times [-b, b]$ in the plane formed by $\widehat{\boldsymbol{e}_1}$ and $\widehat{\boldsymbol{e}_2}$, the equivalent current density is also a constant, which we denote by $\boldsymbol{I}$, and we have

$$\begin{aligned}\boldsymbol{F}(k, \widehat{\boldsymbol{x}}) &= \int_{-a}^{a}\int_{-b}^{b} e^{-ik\widehat{\boldsymbol{x}}\cdot(s_1\widehat{\boldsymbol{e}_1}+s_2\widehat{\boldsymbol{e}_2})}\boldsymbol{I}\, ds_1 ds_2 \\ &= \boldsymbol{I}\,(2b\ \mathrm{sinc}(kb\widehat{\boldsymbol{x}}\cdot\widehat{\boldsymbol{e}_1}))\,(2a\ \mathrm{sinc}(ka\widehat{\boldsymbol{x}}\cdot\widehat{\boldsymbol{e}_2}))\,. \end{aligned} \tag{8.27}$$

We follow the same procedure as above to determine the beamwidth, and obtain the same result, with L replaced by a in the $\hat{\boldsymbol{e}}_2$ direction and by b in the $\hat{\boldsymbol{e}}_2$ direction. Again this is used in (8.22) to obtain the electric field.

8.4.3 A Linear Array of Short Linear Antennas

We consider the case of N short antennas each pointing in direction $\widehat{\boldsymbol{e}}$, each of length $2a$, each carrying the constant current $\boldsymbol{I} = I\widehat{\boldsymbol{e}}$, and positioned a distance d apart in the $\widehat{\boldsymbol{e}}_\perp$ direction. Then the radiation vector is

$$\begin{aligned}\boldsymbol{F}(k, \widehat{\boldsymbol{x}}) &= \boldsymbol{I}\sum_{n=0}^{N-1}\int e^{-ik\widehat{\boldsymbol{x}}\cdot(\widehat{\boldsymbol{e}}s+nd\widehat{\boldsymbol{e}}_\perp)}\, ds \\ &= -2a\boldsymbol{I}\ \mathrm{sinc}(ka\widehat{\boldsymbol{x}}\cdot\widehat{\boldsymbol{e}})\sum_{n=0}^{N-1} e^{-ik\widehat{\boldsymbol{x}}\cdot\widehat{\boldsymbol{e}}_\perp dn} = \boldsymbol{F}_1(k, \widehat{\boldsymbol{x}})\ A(k, \widehat{\boldsymbol{x}}), \end{aligned} \tag{8.28}$$

where $\boldsymbol{F}_1$ denotes the *element factor*, which is the single-element radiation vector (in this case $-2a\boldsymbol{I}\ \mathrm{sinc}(ka\widehat{\boldsymbol{x}}\cdot\widehat{\boldsymbol{e}})$), and where A is the *array factor*

$$A(k,\widehat{\boldsymbol{x}}) = \sum_{n=0}^{N-1} e^{-ik\widehat{\boldsymbol{x}}\cdot\widehat{\boldsymbol{e}}_\perp dn} = \frac{1-e^{ikdN\widehat{\boldsymbol{x}}\cdot\widehat{\boldsymbol{e}}_\perp}}{1-e^{ikd\widehat{\boldsymbol{x}}\cdot\widehat{\boldsymbol{e}}_\perp}} = \underbrace{\frac{e^{ikdN\widehat{\boldsymbol{x}}\cdot\widehat{\boldsymbol{e}}_\perp/2}}{e^{ikd\widehat{\boldsymbol{x}}\cdot\widehat{\boldsymbol{e}}_\perp/2}}}_{\text{phase factor}} \underbrace{\left[\frac{\sin(kd\widehat{\boldsymbol{x}}\cdot\widehat{\boldsymbol{e}}_\perp N/2)}{\sin(kd\widehat{\boldsymbol{x}}\cdot\widehat{\boldsymbol{e}}_\perp/2}\right]}_{\text{magnitude}}. \quad (8.29)$$

We note that the magnitude of the array factor is periodic with period defined by $kd\widehat{\boldsymbol{x}}\cdot\widehat{\boldsymbol{e}} = 2\pi$. This means that when kd is sufficiently big, the array has extra main lobes, called *grating lobes*.

Consequently, so long as the array is made up of copies of the same elements, the analysis of phased arrays reduces to the following:

1. Calculation of the radiation vector for a single element.
2. Calculation of the array factor A.

8.4.4 Array Steering

In the above example, the current on each antenna element was assumed to be the same. We could, of course, drive them with complex-valued voltages (i.e., with amplitude and phase): If we replace $\boldsymbol{I}$ in (8.28) by $\boldsymbol{I}\exp(ikjd\cos\phi_0)$, then the array factor becomes

$$A(k,\widehat{\boldsymbol{x}}) = \sum_{j=0}^{N} e^{ikjd\cos\phi_0} e^{-ikjd\widehat{\boldsymbol{x}}\cdot\widehat{\boldsymbol{e}}_\perp} = \sum_{j=0}^{N} \boldsymbol{I}_j e^{-ikjd(\widehat{\boldsymbol{x}}\cdot\widehat{\boldsymbol{e}}_\perp - \cos\phi_0)}.$$

In this case, the maximum of the array factor now occurs when $\widehat{\boldsymbol{x}}\cdot\widehat{\boldsymbol{e}}_\perp - \cos\phi_0 = 0$. Consequently, the beam pattern will be rotated, even though the antenna itself remains fixed. When the array pattern is shifted in this manner, the array is said to be an *electronically steered array* (ESA). It is also referred to as a *phased array*.

8.5 Antenna Properties

In our analysis above we have assumed that the current density on the antenna is known. This current density depends on the antenna geometry and on how the antenna is fed, and calculating this current density is the most difficult part of antenna design. In general, the current density must be computed numerically.

Antennas can have a variety of properties that are important in practice. We summarize some of them below [125].

8.5.1 Beamwidth

We have seen above that the beamwidth is no narrower than twice the ratio of wavelength to antenna size. This holds even in the case when the current density is not constant over the antenna. Tapering the current density to zero near the edges of the antenna reduces the (undesirable) sidelobes, at the expense of broadening the main beam slightly [99].

8.5.2 Directivity

Most SAR antennas radiate the bulk of their energy in a narrow beam. The antenna characteristic that describes how well the antenna concentrates energy in certain directions is the antenna *directivity*. The directivity $D(\widehat{\boldsymbol{e}})$ in direction $\widehat{\boldsymbol{e}}$ is defined as

$$D(\widehat{\boldsymbol{e}}) = \frac{\text{radiation intensity in direction } \widehat{\boldsymbol{e}}}{\text{average radiation intensity}} = \frac{U(\widehat{\boldsymbol{e}})}{\frac{1}{4\pi}\int_{S^2} U(\widehat{\boldsymbol{e}})dS}, \tag{8.30}$$

where S^2 denotes the unit sphere (i.e., the spherical shell of radius 1) and where the radiation intensity U in direction $\widehat{\boldsymbol{e}}$ is given by [62]

$$U(\widehat{\boldsymbol{e}}) = \frac{r^2}{2}\widehat{\boldsymbol{e}} \cdot \text{Re}\left[\boldsymbol{E}(r\widehat{\boldsymbol{e}}) \times \boldsymbol{H}^*(r\widehat{\boldsymbol{e}})\right]. \tag{8.31}$$

The fact that (8.31) is positive and independent of r follows from (8.23).

8.5.3 Gain

Antenna *gain* describes how well the antenna transforms input power into radiation intensity in a certain direction:

$$\text{Gain}(\widehat{\boldsymbol{e}}) = \frac{4\pi U(\widehat{\boldsymbol{e}})}{\text{input power}}. \tag{8.32}$$

8.5.4 Radiation Efficiency

The *radiation efficiency* e_r of an antenna is the ratio of the total radiated power to the input power:

$$e_r = \frac{\int_{S^2} U(\widehat{\boldsymbol{e}})dS}{\text{input power}}. \tag{8.33}$$

Thus we have $\text{Gain}(\widehat{\boldsymbol{e}}) = e_r D(\widehat{\boldsymbol{e}})$.

Many antennas have radiation efficiency approaching 100%; however, as the antenna size decreases (relative to the wavelength), the radiation efficiency usually becomes very low.

8.5.5 Phase Center

In our derivation of the radiation fields, we took the origin at a point near the antenna and carried out a far-field expansion relative to this point. If, when we do this, we obtain a radiation vector $\boldsymbol{F}$ with constant phase (in the neighborhood of a direction of interest), then we say that the origin is the antenna *phase center*. In other words, if we rotate the antenna about its phase center, then the phase of $\boldsymbol{F}$ does not change.

An antenna's phase center can be determined in practice by finding a far-field surface of constant phase, approximating the surface as necessary by a sphere, and determining the sphere's center.

8.6 Antennas in Imaging

In *real-aperture* imaging, we use a big antenna or high frequencies to obtain a narrow beamwidth; consequently the antenna footprint on the ground is fairly small. We scan this footprint over the ground (perhaps using an ESA). For each spot position on a map, we assign a color corresponding to the amplitude of the received energy.

In *synthetic-aperture* imaging, we use a smaller antenna with a wide beam that moves along a flight path. We illuminate the same region from different antenna locations and use mathematics to form a high-resolution image.

8.6.1 Field from Antenna not at the Origin

The analysis above assumes the antenna is located at the origin. If, instead, the antenna is located at $\boldsymbol{x}^0$, we write the current density on the antenna as $\boldsymbol{J}(\omega, \boldsymbol{x} - \boldsymbol{x}^0)$. The vector potential is then

$$\boldsymbol{A}(k, \boldsymbol{x}) = \int \frac{e^{ik|\boldsymbol{x}-\boldsymbol{y}|}}{4\pi|\boldsymbol{x}-\boldsymbol{y}|} \boldsymbol{J}(\omega, \boldsymbol{y} - \boldsymbol{x}^0)\, d\boldsymbol{y}. \tag{8.34}$$

We now write

$$|\boldsymbol{x} - \boldsymbol{y}| = |\boldsymbol{x} - \boldsymbol{x}^0 + \boldsymbol{x}^0 - \boldsymbol{y}|,$$

and the far-field assumptions take the form $|\boldsymbol{x} - \boldsymbol{x}^0| \gg |\boldsymbol{x}^0 - \boldsymbol{y}|$ and $|\boldsymbol{x} - \boldsymbol{x}^0| \gg k|\boldsymbol{x}^0 - \boldsymbol{y}|^2$, which give rise to the approximation

$$|\boldsymbol{x} - \boldsymbol{y}| = |\boldsymbol{x} - \boldsymbol{x}^0| - \widehat{\boldsymbol{x} - \boldsymbol{x}^0} \cdot (\boldsymbol{x}^0 - \boldsymbol{y}) + \cdots. \tag{8.35}$$

The analysis of section 8.3 now applies with $\boldsymbol{x}$ replaced by $\boldsymbol{x} - \boldsymbol{x}^0$ and with $\boldsymbol{y}$ replaced by $\boldsymbol{y} - \boldsymbol{x}^0$. This results in the far-field expression for the vector potential

$$\boldsymbol{A}(k, \boldsymbol{x}) \approx \frac{e^{ik|\boldsymbol{x}-\boldsymbol{x}^0|}}{4\pi|\boldsymbol{x}-\boldsymbol{x}^0|} \mathcal{F}[\boldsymbol{J}](\omega, \widehat{\boldsymbol{x} - \boldsymbol{x}^0}). \tag{8.36}$$

8.6.2 The Scalar Antenna Model

A typical SAR antenna transmits a single polarization on each pulse, and the measured voltages correspond to receiving a single polarization. In the case when the antenna is highly directional, there are only two possible polarizations, namely, those perpendicular to the beam direction. These two polarizations are denoted H for "horizontal" and V for "vertical" (with respect to the horizon). Thus a typical narrow-beam radar system has four possible polarization "channels," namely, HH, HV, VH, and VV, where the first letter in the sequence denotes the transmit polarization and the second letter denotes the receive polarization. (In most cases, the VH and HV channels are the same.)

We do not have a mathematical model for polarimetric scattering that is tractable for imaging. Consequently, images are made from each polarization channel separately, and for each channel we use a scalar model for the electromagnetic signal.

In particular, we use a scalar model for radiation from an antenna. Table 8.1 shows the correspondence between the true vector model on the left and our scalar model on the right. In the right column we use a subscript l as a reminder that the scalar model should be

Table 8.1. *Comparison of the vector and scalar antenna models.*

Vector model	Scalar model
$\nabla^2 \boldsymbol{\mathcal{A}} - \mu_0\epsilon_0\partial_t^2 \boldsymbol{\mathcal{A}} = -\mu_0 \boldsymbol{\mathcal{J}}$ $\nabla^2 \boldsymbol{A} + k^2 \boldsymbol{A} = -\mu_0 \boldsymbol{J}$	$\nabla^2 \mathcal{E}_l - \mu_0\epsilon_0\partial_t^2 \mathcal{E}_l = \mu_0 \partial_t \mathcal{J}_l$ $\nabla^2 E_l + k^2 E_l = -i\omega\mu_0 J_l$
$\boldsymbol{A}(\omega, \boldsymbol{x}) = \int \frac{e^{ik\lvert\boldsymbol{x}-\boldsymbol{y}\rvert}}{4\pi\lvert\boldsymbol{x}-\boldsymbol{y}\rvert} \mu_0 \boldsymbol{J}(\omega, \boldsymbol{y}) d\boldsymbol{y}$ $\boldsymbol{E} = i\omega \left[\boldsymbol{A} + k^{-2}\nabla(\nabla \cdot \boldsymbol{A})\right]$	$E_l(\omega, \boldsymbol{x}) = \int \frac{e^{ik\lvert\boldsymbol{x}-\boldsymbol{y}\rvert}}{4\pi\lvert\boldsymbol{x}-\boldsymbol{y}\rvert} (i\omega\mu_0) J_l(\omega, \boldsymbol{y}) d\boldsymbol{y}$
$\boldsymbol{E}(\boldsymbol{x}) \approx i\omega\mu_0 \frac{e^{ik\lvert\boldsymbol{x}\rvert}}{4\pi\lvert\boldsymbol{x}\rvert} [\boldsymbol{F} - \widehat{\boldsymbol{x}}(\widehat{\boldsymbol{x}} \cdot \boldsymbol{F})]$	$E_l(\boldsymbol{x}) \approx i\omega\mu_0 \frac{e^{ik\lvert\boldsymbol{x}\rvert}}{4\pi\lvert\boldsymbol{x}\rvert} F_l$
$\boldsymbol{F}(k, \widehat{\boldsymbol{x}}) = \int e^{-ik\widehat{\boldsymbol{x}}\cdot\boldsymbol{y}} \boldsymbol{J}(\omega, \boldsymbol{y}) d\boldsymbol{y}$	$F_l(k, \widehat{\boldsymbol{x}}) = \int e^{-ik\widehat{\boldsymbol{x}}\cdot\boldsymbol{y}} J_l(\omega, \boldsymbol{y}) d\boldsymbol{y}$

thought of as corresponding roughly to a single Cartesian component of the corresponding vector quantity. In the rest of the book we drop the subscript l; note that $\mathcal{E}$ or E thus denotes *a single Cartestian component* of $\boldsymbol{\mathcal{E}}$ or $\boldsymbol{E}$ and *not* the magnitude of $\boldsymbol{\mathcal{E}}$ or $\boldsymbol{E}$. In general the scalar model is adequate for narrow beams and polarizations roughly perpendicular to the beam direction.

8.6.3 Antenna Reception

When an electromagnetic wave impinges on an antenna, it induces currents on the antenna that can be measured; these measurements are the received signal [116].

The reception process is easiest to imagine if one thinks of an array antenna, centered around $\boldsymbol{x}^0$, in which the effect from each element is to multiply each frequency by a weighting function W that depends on position $\boldsymbol{z}$ on the antenna:

$$S_{\text{rec}}(\omega) \propto \int_{\boldsymbol{z} \in \text{antenna at } \boldsymbol{x}^0} E^{\text{sc}}(\omega, \boldsymbol{z}) W(\omega, \boldsymbol{z})\, d\boldsymbol{z}. \tag{8.37}$$

We then insert expression (6.16) for the scattered field to obtain

$$\begin{aligned} S_{\text{rec}} &= \int_{\text{antenna}} \int \frac{e^{ik\lvert\boldsymbol{z}-\boldsymbol{y}\rvert}}{4\pi\lvert\boldsymbol{z}-\boldsymbol{y}\rvert} k^2 V(\boldsymbol{y}) E^{\text{tot}}(\boldsymbol{y})\, d\boldsymbol{y} W(\omega, \boldsymbol{z})\, d\boldsymbol{z} \\ &\propto \int \frac{e^{ik\lvert\boldsymbol{y}-\boldsymbol{x}^0\rvert}}{4\pi\lvert\boldsymbol{y}-\boldsymbol{x}^0\rvert} k^2 V(\boldsymbol{y}) E(\boldsymbol{y}) \underbrace{\int e^{-ik(\widehat{\boldsymbol{y}-\boldsymbol{x}^0})\cdot(\boldsymbol{z}-\boldsymbol{x}^0)} W(\omega, \boldsymbol{z})\, d\boldsymbol{z}}_{F_{\text{rec}} \propto \mathcal{F}[W]}\, d\boldsymbol{y}, \end{aligned} \tag{8.38}$$

where in the second line we have used the far-field expansion (8.35) with $\lvert\boldsymbol{y}-\boldsymbol{x}^0\rvert \gg \lvert\boldsymbol{x}^0-\boldsymbol{z}\rvert$. Thus we see that the effect of antenna reception is to include a second factor corresponding to the antenna beam pattern. Typically, when the same antenna is used for transmission and reception, the antenna beam patterns for transmission and reception are the same.

Chapter 9

Synthetic-Aperture Radar

With better models for the field radiated from an antenna, we now return to (6.21), where for E^{in} we use the scalar model

$$\left(\nabla^2 + k^2\right) E^{\text{in}} = J,$$

where $k = \omega/c$, and where J is proportional to the effective current density on the antenna. As listed in Table 8.1, we obtain

$$E^{\text{in}}(\omega, \boldsymbol{x}) = \int G(\omega, \boldsymbol{x} - \boldsymbol{y}) J(\omega, \boldsymbol{y}) d\boldsymbol{y} \approx \frac{e^{ik|\boldsymbol{x}-\boldsymbol{x}^0|}}{4\pi|\boldsymbol{x} - \boldsymbol{x}^0|} F\left(k, \widehat{\boldsymbol{x} - \boldsymbol{x}^0}\right), \tag{9.1}$$

where we have used the far-field approximation and we have used $\boldsymbol{x}^0$ as the antenna center. Here F is the scalar analogue of the radiation vector, listed on the bottom line of Table 8.1. The function F includes the transmitted waveform.

Consequently the Born-approximated scattered field is

$$\begin{aligned} E_B^{\text{sc}}(\omega, \boldsymbol{x}) &= \int G(\omega, \boldsymbol{x} - \boldsymbol{y}) k^2 V(\boldsymbol{y}) E^{\text{in}}(\omega, \boldsymbol{y})\, d\boldsymbol{y} \\ &= \int \frac{e^{ik|\boldsymbol{x}-\boldsymbol{y}|}}{4\pi|\boldsymbol{x} - \boldsymbol{y}|} k^2 V(\boldsymbol{y}) \frac{e^{ik|\boldsymbol{y}-\boldsymbol{x}^0|}}{4\pi|\boldsymbol{y} - \boldsymbol{x}^0|} F\left(k, \widehat{\boldsymbol{y} - \boldsymbol{x}^0}\right) d\boldsymbol{y}. \end{aligned} \tag{9.2}$$

If we assume that the receiving antenna is at the same location as the transmitting antenna, and that the reception pattern is denoted by F_{rec}, then from the same computation used to obtain (8.38), we find that the scalar Born model for the received signal is

$$S_B(\omega) = \int e^{2ik|\boldsymbol{x}^0-\boldsymbol{y}|} A(\omega, \boldsymbol{x}^0, \boldsymbol{y}) V(\boldsymbol{y})\, d\boldsymbol{y}, \tag{9.3}$$

where A incorporates the geometrical spreading factors, transmitted waveform, and antenna beam patterns:

$$A(k, \boldsymbol{x}^0, \boldsymbol{y}) = \frac{k^2 F\left(k, \widehat{\boldsymbol{y} - \boldsymbol{x}^0}\right) F_{\text{rec}}\left(k, \widehat{\boldsymbol{y} - \boldsymbol{x}^0}\right)}{(4\pi|\boldsymbol{x}^0 - \boldsymbol{y}|)^2}. \tag{9.4}$$

We can also include the effect of matched filtering into A.

Synthetic-aperture imaging involves a moving platform, and usually the antenna is pointed toward the earth. We denote by $\boldsymbol{\gamma}$ the antenna path. For a pulsed system, we assume that pulses are transmitted at times t_n and that the antenna position at time t_n is $\boldsymbol{\gamma}(t_n)$. Because the time scale on which the antenna moves is much slower than the time scale on which the electromagnetic waves propagate, we separate the time scales into a *slow time* s, which corresponds to the n of t_n, and a *fast time* t. Using a continuum model for the slow time makes some of the analysis simpler but also leaves out some important effects that we will consider in section 9.4 below.

Using the continuum model for slow time, in (9.3) we replace the antenna position $\boldsymbol{x}^0$ by $\boldsymbol{\gamma}(s)$:

$$D(\omega, s) = F[V](\omega, s) := \int e^{2ik|\boldsymbol{\gamma}(s)-\boldsymbol{y}|} A(\omega, s, \boldsymbol{y}) V(\boldsymbol{y})\, d\boldsymbol{y}, \tag{9.5}$$

where with a slight abuse of notation we have replaced the $\boldsymbol{x}^0$ in the argument of A by s. This notation also allows for the possibility that the waveform and antenna beam pattern could be different at different points along the flight path. The time-domain version of (9.5) is

$$d(t, s) = \int e^{-i\omega[t-2|\boldsymbol{\gamma}(s)-\boldsymbol{y}|/c]} A(\omega, s, \boldsymbol{y}) V(\boldsymbol{y})\, d\boldsymbol{y}. \tag{9.6}$$

The goal of SAR is to determine V from the data d.

As in the case of ISAR, assuming that $\boldsymbol{\gamma}$ and A are known, the data depend on two variables, so we expect to form a two-dimensional image. For typical radar frequencies, since most of the scattering takes place in a thin layer at the surface, we assume that the ground reflectivity function V is supported on a known surface. For simplicity we take this surface to be a flat plane, so that $V(\boldsymbol{x}) = V(\mathbf{x})\delta(x_3)$, where $\mathbf{x} = (x_1, x_2)$.

SAR imaging comes in two basic varieties: *spotlight* SAR and *stripmap* SAR.

9.1 Spotlight SAR

Spotlight SAR is illustrated in Figure 9.1. Here the moving radar system stares at a specific location (usually on the ground) so that at each point in the flight path the same target is illuminated from a different direction. When the ground is assumed to be a horizontal plane, the iso-range curves are large circles whose centers are directly below the antenna at $\boldsymbol{\gamma}(s)$. If the radar antenna beamwidth is narrow and the antenna footprint is sufficiently far away, then the circular arcs within the footprint can be approximated as lines. Consequently, the imaging method is mathematically the same as that used in ISAR.

In particular, we put the origin of coordinates in the footprint, use the far-field expansion, and obtain for the matched-filtered frequency-domain data

$$D(\omega, s) = e^{2ik|\boldsymbol{\gamma}(s)|} \int e^{2ik\widehat{\boldsymbol{\gamma}}(s)\cdot\boldsymbol{y}} V(\boldsymbol{y}) A(\omega, s, \boldsymbol{y})\, d\boldsymbol{y}. \tag{9.7}$$

We approximate A within the footprint as a product of a function of (ω, s) and a function of $\boldsymbol{y}$. The function of (ω, s) can be taken outside the integral; the function of $\boldsymbol{y}$ can be divided out after inverse Fourier transforming.

As in the ISAR case, the time-domain formulation of spotlight SAR leads to a problem of inverting the Radon transform.

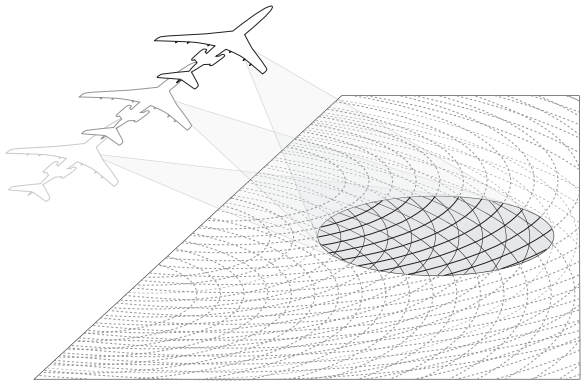

Figure 9.1. *In spotlight SAR the radar is trained on a particular location as the radar platform moves. In this figure the equirange circles (dotted lines) are formed from the intersection of the radiated spherical wavefront and the surface of a (flat) earth.*

9.2 Stripmap SAR

Stripmap SAR sweeps the radar beam along with the platform without staring at a particular location on the ground (Figure 9.2).The equirange curves are still circles, but the data no longer depend only on the direction from the antenna to the scene. Moreover, because the radar doesn't stare at the same location, there is no natural origin of coordinates for which the far-field expansion is valid.

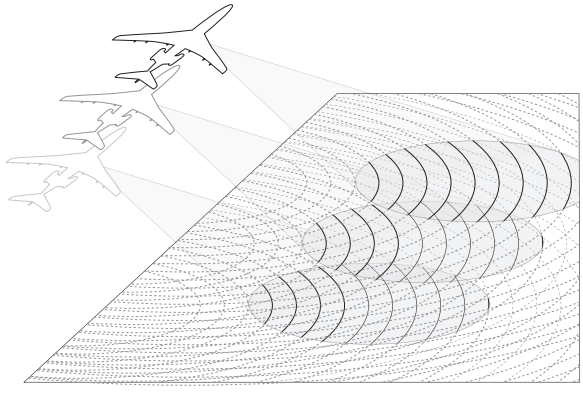

Figure 9.2. *Stripmap SAR acquires data without staring. The radar typically has fixed orientation with respect to the platform, and the data are acquired as the beam footprint sweeps over the ground.*

To form a stripmap SAR image, we want to invert (9.5) without the help of the far-field approximation. Our strategy is to use a filtered adjoint of the forward map F. Use of the adjoint is natural for a number of reasons. First, in the far-field (ISAR) case, inversion is done by means of the inverse Fourier transform, and the inverse Fourier transform is precisely

the adjoint of the forward Fourier transform. Second, in the time-domain formulation of ISAR, inversion is done by inverting the Radon transform, and this inverse is again a filtered version of the adjoint of the forward transform (see (7.25)). Third, the adjoint is natural because it maps functions of frequency and slow time to functions of position. Thus it is natural to attempt to construct the inverse from a modified version of the adjoint. In particular, our modification takes the form of a filter, which we choose so that the resulting imaging method has a desirable PSF.

The Formal Adjoint of F

The adjoint $F^\dagger$ is an operator such that

$$\langle f, Fg\rangle_{\omega,s} = \langle F^\dagger f, g\rangle_{\boldsymbol{x}}, \tag{9.8}$$

or, more specifically,

$$\int f(\omega, s)\,(Fg)^*(\omega, s)\,d\omega\,ds = \int (F^\dagger f)(\boldsymbol{x}) g^*(\boldsymbol{x})\,d\boldsymbol{x}. \tag{9.9}$$

Using (9.5) in (9.9) and interchanging the order of integration, we find that

$$F^\dagger f(\boldsymbol{x}) = \int e^{-2ik|\boldsymbol{\gamma}(s)-\boldsymbol{x}|} A(\omega, s, \boldsymbol{x}) f(\omega, s)\,d\omega\,ds. \tag{9.10}$$

The Imaging Operator

Thus we look for an imaging operator of the form

$$I(\mathbf{z}) = B[D](\mathbf{z}) := \int e^{-2ik|\boldsymbol{\gamma}(s)-\boldsymbol{z}_T|} Q(\omega, s, \mathbf{z}) D(\omega, s)\,d\omega\,ds, \tag{9.11}$$

where $\boldsymbol{z}_T = (\mathbf{z}, 0)$ and where Q is a filter to be determined below. The time-domain version is

$$I(\mathbf{z}) = \mathcal{B}[d](\mathbf{z}); = \int e^{i\omega(t-2|\boldsymbol{\gamma}(s)-\boldsymbol{z}_T|/c)} Q(\omega, s, \mathbf{z})\,d\omega d(t, s)\,ds\,dt. \tag{9.12}$$

If we were to choose the filter Q to be identically 1, then, because of (8), the time-domain inversion would have the form

$$\begin{aligned} I(\mathbf{z}) &= \int \delta(t - 2|\boldsymbol{\gamma}(s) - \boldsymbol{z}_T|/c) d(t, s)\,ds\,dt \\ &= \int d(2|\boldsymbol{\gamma}(s) - \boldsymbol{z}_T|/c, s)\,ds, \end{aligned} \tag{9.13}$$

which can be interpreted as follows: At each antenna position s, we backproject the data to all the locations $\mathbf{z}$ that are at the correct travel time $2|\boldsymbol{\gamma}(s) - \boldsymbol{z}_T|/c$ from the antenna location $\boldsymbol{\gamma}(s)$. Then we sum all the contributions coherently (i.e., including the phase). Figure 9.3 shows the partial sums over s as the antenna (white triangle) moves along a straight flight path from bottom to top.

An alternative interpretation is that to form the image at the reconstruction point $\mathbf{z}$, we coherently sum all the contributions from the data at all points (t, s) for which $t = 2|\boldsymbol{\gamma}(s) - \boldsymbol{z}_T|/c$.

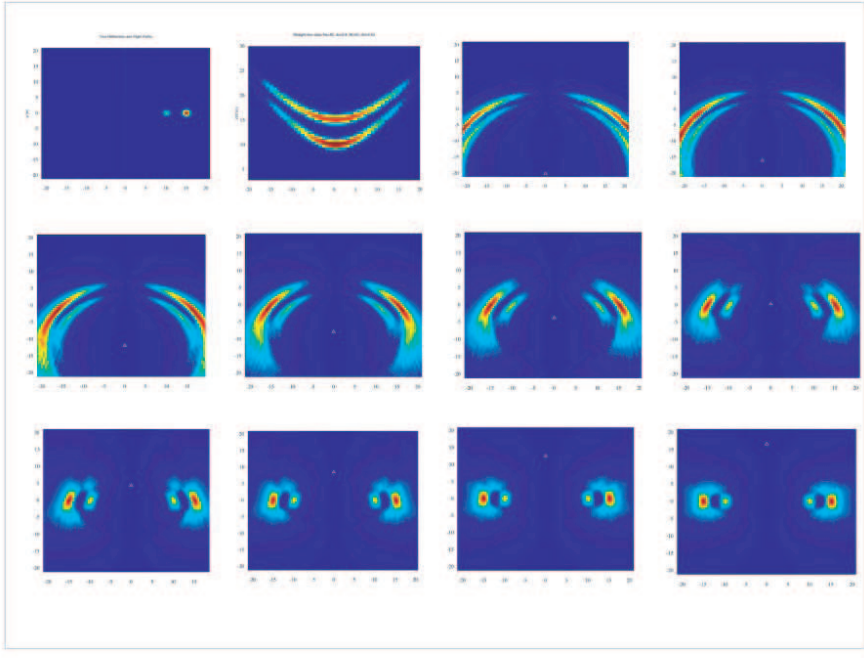

Figure 9.3. *This shows successive steps in the backprojection procedure for a straight flight path and an isotropic antenna. The first image is the true scene; the second is the magnitude of the data. The successive images show the image when the antenna is at the location indicated by the small triangle.*

Note the similarity between (9.13) and (7.28): (7.28) backprojects over lines or planes, whereas (9.13) backprojects over circles. The inversion (9.12) first applies the filter Q and then backprojects.

9.2.1 The Stripmap SAR Point-Spread Function

We substitute (9.5) into (9.11) to obtain

$$I(\mathbf{z}) = \int \underbrace{\int e^{i2k(|\boldsymbol{R}_{s,\mathbf{z}}|-|\boldsymbol{R}_{s,\mathbf{x}}|)} QA(\ldots)\, d\omega ds}_{K(\mathbf{z},\mathbf{x})}\, V(\mathbf{x}) d\mathbf{x},$$

where we have written $\boldsymbol{R}_{s,\mathbf{z}} = \boldsymbol{z}_T - \boldsymbol{\gamma}(s)$. The PSF K is

$$K(\mathbf{z}, \mathbf{x}) = \int e^{i2k(|\boldsymbol{R}_{s,\mathbf{z}}|-|\boldsymbol{R}_{s,\mathbf{x}}|)} QA(\ldots) d\omega ds. \tag{9.14}$$

We would like the PSF K to look like a delta function

$$\delta(\mathbf{z}-\mathbf{x}) \propto \int e^{i(\mathbf{z}-\mathbf{x})\cdot\boldsymbol{\xi}} d\boldsymbol{\xi}, \tag{9.15}$$

because this would imply that the image I would be identical to the reflectivity function V.

To determine how close K is to (9.15), we analyze K by the method of stationary phase.

The Stationary Phase Theorem

The stationary phase theorem [16, 61, 42, 130, 133] gives us an approximate formula for the large-β behavior of oscillatory integrals of the form $\int \exp[i\beta\phi(\boldsymbol{x})]a(\boldsymbol{x})d^n\boldsymbol{x}$. The idea is that as β becomes large, the oscillations of the exponential become more and more rapid (see Figure 9.4). Such an integral experiences a great deal of cancellation, so that the result is very small. Thus the main contribution to the integral comes from the parts of the phase with the fewest oscillations, namely, the part where the phase has a maximum or minimum.

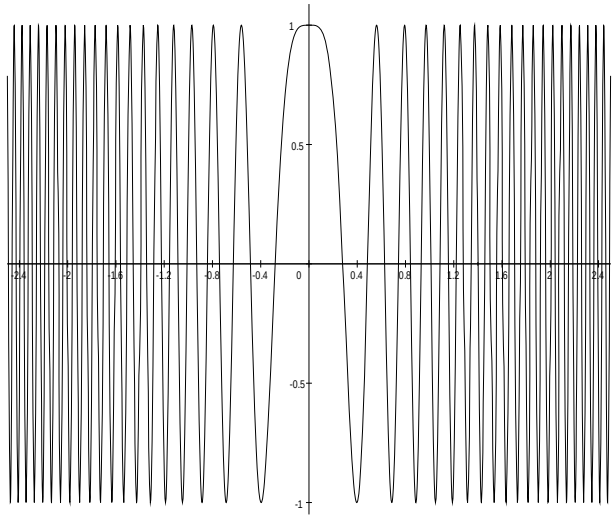

Figure 9.4. *This shows the real part of* $\exp(i\beta x^2)$. *Clearly most of the contribution to* $\int \exp(i\beta x^2)\,dx$ *comes from the region near the origin.*

We assume that (i) a is a smooth function of compact support and (ii) ϕ has only nondegenerate critical points (i.e., wherever $\nabla\phi = 0$, we also have that the Hessian $D^2\phi$, which is the matrix of second derivatives of ϕ, is nonsingular). Then as $\beta \to \infty$,

$$\int e^{i\beta\phi(\boldsymbol{x})} a(\boldsymbol{x}) d^n\boldsymbol{x} \tag{9.16}$$

$$= \sum_{\{\boldsymbol{x}^0:\nabla\phi(\boldsymbol{x}^0)=\mathbf{0}\}} \left(\frac{2\pi}{\beta}\right)^{n/2} a(\boldsymbol{x}^0) \frac{e^{i\beta\phi(\boldsymbol{x}^0)} e^{i(\pi/4)\operatorname{sgn} D^2\phi(\boldsymbol{x}^0)}}{\sqrt{|\det D^2\phi(\boldsymbol{x}^0)|}} + O(\beta^{-n/2-1}).$$

Here sgn denotes the signature, which is defined as the number of positive eigenvalues minus the number of negative eigenvalues.

The SAR Critical Points

We apply the stationary phase theorem to (9.14) in the ω and s variables. To introduce a large parameter, we make the change of variables $k = \beta k'$ (i.e., $\omega = \beta\omega'$). This converts (9.14) to

$$K(\mathbf{z}, \mathbf{x}) = \int e^{2i\beta k'(|\boldsymbol{R}_{s,\mathbf{z}}| - |\boldsymbol{R}_{s,\mathbf{x}}|)} Q A(\ldots) \frac{d\omega'}{\beta} ds, \tag{9.17}$$

where the phase is $\phi = 2k'(|\boldsymbol{R}_{s,\mathbf{z}}| - |\boldsymbol{R}_{s,\mathbf{x}}|)$. We find that the main contribution for large β comes from the critical points, which are found as values of s and ω that satisfy

$$\begin{aligned} 0 &= \frac{\partial \phi}{\partial \omega'} \propto |\boldsymbol{R}_{s,\mathbf{z}}| - |\boldsymbol{R}_{s,\mathbf{x}}|, \\ 0 &= \frac{\partial \phi}{\partial s} \propto \widehat{\boldsymbol{R}}_{s,\mathbf{z}} \cdot \dot{\boldsymbol{\gamma}}(s) - \widehat{\boldsymbol{R}}_{s,\mathbf{x}} \cdot \dot{\boldsymbol{\gamma}}(s). \end{aligned} \tag{9.18}$$

The first equation of (9.18) says that the distance (range) from $\boldsymbol{\gamma}(s)$ to $\boldsymbol{z}_T$ must be the same as to $\boldsymbol{x}_T$; the second equation says that the down-range velocity (which gives rise to the Doppler shift) must be the same for $\boldsymbol{z}_T$ and $\boldsymbol{x}_T$. The set of points $\boldsymbol{z}_T$ for which solutions of (9.18) are possible is shown in Figure 9.5. We note that this is exactly the same diagram we used in our discussion of the ambiguity function! Thus the start-stop approximation, together with a full three-dimensional treatment of wave propagation, gives rise to the same intuitive notion of locating a scatterer from its range and Doppler shift.

If K is to look like (9.15), we should have critical points only when $\mathbf{z} = \mathbf{x}$. We see from Figure 5.6 that when V is supported on a flat plane, there are *two* points $\mathbf{z}$ that satisfy (9.18)—one to the left of the flight path and one to the right. This is why SAR systems always use side-looking antennas, so that A is zero for one of these points and consequently only one of these points contributes to the image.

The Critical Point $\mathbf{z} = \mathbf{x}$

In a neighborhood of the critical point $\mathbf{z} = \mathbf{x}$, we force the phase of the PSF to look like the phase of (9.15) (namely, $(\mathbf{z} - \mathbf{x}) \cdot \boldsymbol{\xi}$) by doing a Taylor expansion followed by a change of variables. Specifically, we use the formula

$$f(\mathbf{z}) - f(\mathbf{x}) = \int_0^1 \frac{d}{d\mu} f(\mathbf{x} + \mu(\mathbf{z} - \mathbf{x}))\, d\mu = (\mathbf{z} - \mathbf{x}) \cdot \int_0^1 \nabla f|_{\mathbf{x}+\mu(\mathbf{z}-\mathbf{x})}\, d\mu, \tag{9.19}$$

with $f(\mathbf{x}) = 2k|\boldsymbol{R}_{s,\mathbf{x}}|$ to write

$$2k(|\boldsymbol{R}_{s,\mathbf{z}}| - |\boldsymbol{R}_{s,\mathbf{x}}|) = (\mathbf{z} - \mathbf{x}) \cdot \Xi(\mathbf{x}, \mathbf{z}, s, \omega),$$

where

$$\Xi = \int_0^1 \nabla f|_{\mathbf{x}+\mu(\mathbf{z}-\mathbf{x})}\, d\mu.$$

Near $\mathbf{z} = \mathbf{x}$, we have $\Xi(\mathbf{x}, \mathbf{z}, s, \omega) \approx 2k\mathcal{P}[\widehat{\boldsymbol{R}}_{s,\mathbf{z}}]$, where the operator $\mathcal{P}$ projects a vector onto its first two components.

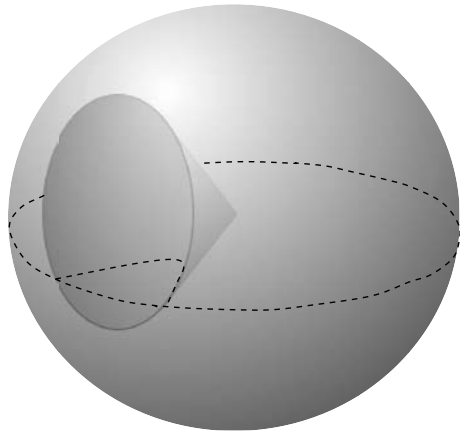

Figure 9.5. *The critical set (9.18).*

We then make the (Stolt) change of variables [123]

$$(s, \omega) \to \boldsymbol{\xi} = \Xi(\mathbf{x}, \mathbf{z}, s, \omega),$$

which converts (9.14) into

$$K(\mathbf{z}, \mathbf{x}) = \int e^{i(\mathbf{z}-\mathbf{x})\cdot\boldsymbol{\xi}} Q(\boldsymbol{\xi}, \mathbf{z}) A(\omega(\boldsymbol{\xi}), s(\boldsymbol{\xi}), \mathbf{x}) \left| \frac{\partial(s, \omega)}{\partial \boldsymbol{\xi}} \right| d\boldsymbol{\xi}. \tag{9.20}$$

Comparing (9.20) with (9.15), clearly we should take $Q = \chi/(A\ |\partial(s, \omega)/\partial\boldsymbol{\xi}|)$, where χ is a smooth cutoff function that prevents division by zero. (Another approach for choosing Q, involving statistical considerations, is given in [152].) The quantity $|\partial(s, \omega)/\partial\boldsymbol{\xi}|$ is sometimes called the *Beylkin determinant* [15].

Note that there are indeed large regions where the amplitude A is zero, including frequencies out of the frequency band of the radar and angles that are out of the antenna beam. Thus the $\boldsymbol{\xi}$ integral in (9.20) extends over only a certain set, which we call the *data collection manifold*.

We note also that Q can depend only on $\mathbf{z}$, and not on $\mathbf{x}$, whereas A can depend only on $\mathbf{x}$ and not on $\mathbf{z}$. Thus it seems unclear how we can define $Q \propto 1/A$. However, the leading-order contribution to the integral (9.20) is at $\mathbf{z} = \mathbf{x}$.[15] Consequently we simply evaluate A and $|\partial(s, \omega)/\partial\boldsymbol{\xi}|$ at $\mathbf{x} = \mathbf{z}$ to obtain

$$Q(\omega, s, \mathbf{z}) = \frac{\chi(\omega, s, \mathbf{z}) \left| \frac{\partial \boldsymbol{\xi}}{\partial(s,\omega)} \right|}{A(\omega, s, \mathbf{z})} = \frac{\chi(\omega, s, \mathbf{z}) A^*(\omega, s, \mathbf{z}) \left| \frac{\partial \boldsymbol{\xi}}{\partial(s,\omega)} \right|}{|A(\omega, s, \mathbf{z})|^2}. \tag{9.21}$$

We see from the rightmost term of (9.21) that we can think of the filter as automatically including the correlation reception.

[15] Note that we cannot apply the stationary phase theorem to $\int \exp[i(\mathbf{z} - \mathbf{x}) \cdot \boldsymbol{\xi}] d\boldsymbol{\xi}$, because the Hessian of the phase is zero at the critical point. Instead we consider $\int \exp[i(\mathbf{z} - \mathbf{x}) \cdot \boldsymbol{\xi}] d\boldsymbol{\xi}\, f(\mathbf{x}) d\mathbf{x} = \iint \exp[i(\mathbf{z} - \mathbf{x}) \cdot \boldsymbol{\xi}] d\boldsymbol{\xi} \int \exp(i\mathbf{x} \cdot \boldsymbol{\eta}) F(\boldsymbol{\eta}) d\boldsymbol{\eta} d\mathbf{x}$ and apply the stationary phase theorem in the *pair* of variables $\mathbf{x}$ and $\boldsymbol{\xi}$.

Summary for Single Critical Point at z = x

- We form the image by

$$I(\mathbf{z}) = \int e^{-ik2|\boldsymbol{R}_{s,\mathbf{z}}|} Q(\mathbf{z}, s, \omega)\ D(\omega, s) ds d\omega,$$

  where Q is given by (9.21) and $\boldsymbol{\xi} = 2k\mathcal{P}\widehat{\boldsymbol{R}}_{s,\mathbf{z}}$.

- If the antenna illuminates only the critical point $\mathbf{z} = \mathbf{x}$, then, to leading order, the PSF is

$$K(\mathbf{z}, \mathbf{x}) \sim \int_{\text{data manifold}} e^{i(\mathbf{z}-\mathbf{x})\cdot\boldsymbol{\xi}} d^2\boldsymbol{\xi}. \tag{9.22}$$

We see in section 9.3.4 below that the form of the PSF K has the following implications:

1. The visible edges in the scene, which correspond to jump singularities in the reflectivity function, appear in the correct location, with the correct orientation.

2. Resolution is determined by the data collection manifold, which in turn is determined by the bandwidth, antenna pattern, and flight path.

Examples of SAR images are shown in Figures 1.7, 6.3, 9.6, 9.10, 9.11, 9.12, 9.13, 10.2, and 11.1.

9.2.2 Resolution

SAR resolution is determined by the data collection manifold, which is the region in $\boldsymbol{\xi}$-space where we have data. We can determine this region by recalling that $\boldsymbol{\xi} \approx 2k\mathcal{P}\hat{\boldsymbol{R}}_{s,\mathbf{z}}$. In general, the PSF is the function (9.22), and this determines the properties of the image. In some cases, however, we can say more.

For a straight flight path and flat earth, the data collection manifold consists of a sector of an annulus, as shown in Figure 7.2. For the narrow angular apertures relevant for satellite-borne systems and other systems with a narrow antenna beam, the annular sector is close to being a rectangle. In that case, if coordinates are chosen appropriately, (9.22) can be (approximately) factored:

$$K(\mathbf{z}, \mathbf{x}) \sim \int_{\text{data manifold}} e^{i(\mathbf{z}-\mathbf{x})\cdot\boldsymbol{\xi}} d^2\boldsymbol{\xi} \approx \int e^{i(z_1-x_1)\xi_1}\, d\xi_1 \int e^{i(z_2-x_2)\xi_2}\, d\xi_2, \tag{9.23}$$

and we can analyze the two factors separately.

For this discussion, we use the convention that the interval $[-b, b]$ in Fourier space corresponds to resolution $2\pi/b$. Thus we use the full width of the main lobe of the sinc function obtained by

$$\int_{-b}^{b} e^{i\rho r} d\rho = \frac{2\sin br}{r} = 2b\text{sinc}(br). \tag{9.24}$$

Figure 9.6. *Example SAR image from Global Hawk imaging radar (courtesy of U.S. Department of Defense).*

Along-Track Resolution

To analyze the resolution in the along-track direction, we consider a rectangular antenna of length L moving along a straight flight path $\boldsymbol{\gamma}(s) = (0, s, h)$ (see Figure 9.7). To determine the resolution in the along-track or *azimuthal* direction, we consider two points on the earth whose coordinates differ only in the second coordinate, so that $\boldsymbol{z} - \boldsymbol{x} = (0, z_2 - x_2)$. The phase of (9.20) is then $(\mathbf{z} - \mathbf{x}) \cdot \boldsymbol{\xi} = (0, z_2 - x_2, 0) \cdot \boldsymbol{\xi} = (z_2 - x_2)\xi_2$, which shows that we need to consider only the second coordinate of the vector $\boldsymbol{\xi} \approx 2k\mathcal{P}\hat{\boldsymbol{R}}_{s,\boldsymbol{z}}$. This second coordinate is $\xi_2 \approx 2k\frac{x_2 - \gamma(s)_2}{R} = \frac{k}{R}\,2(x_2 - s)$, where $R = |\boldsymbol{x}_T - \gamma(s)|$.

However, whether $\xi_2 \approx \frac{k}{R}\,2(x_2 - s)$ is in the data collection manifold depends on the bandwidth of the radar system and the antenna beam pattern. In particular, the interval of s values over which x_2 is in the antenna beam pattern is $2\max|x_2 - s|$, precisely the width of the footprint, which, from (8.26), is $R(2\lambda/L)$. This is the *effective length of the synthetic aperture*. Multiplying this by the k/R in the expression for ξ_2, we obtain

$$\max|\xi_2| \approx \frac{k}{R}\,\frac{2\lambda R}{L} = \frac{4\pi}{L}, \tag{9.25}$$

where we have used $k = 2\pi/\lambda$. From (9.25) and (9.24), we conclude that the resolution in the along-track direction is $\frac{2\pi}{4\pi/L} = \frac{L}{2}$.

The fact that the along-track resolution is $L/2$ is surprising: it is (a) independent of range, (b) independent of λ, and (c) better for small antennas! All these facts are contrary to

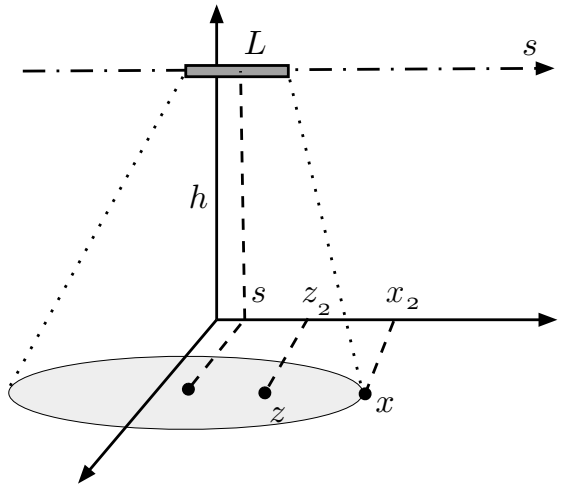

Figure 9.7. *Diagram for analysis of along-track resolution.*

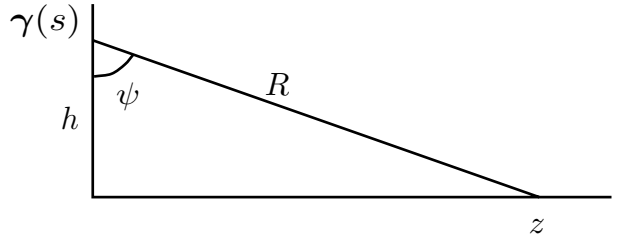

Figure 9.8. *This shows the angle ψ.*

the intuition that researchers had built from their understanding of antenna beam patterns. Consequently the SAR resolution results were not initially believed. However, these results were verified by field tests, and they are now understood to be due to the fact that a wider antenna footprint results in a larger *synthetic* aperture.

Range Resolution

The range direction, in the coordinate system shown in Figure 9.7, is the x_1 direction. The integral $\int e^{i(z_1-x_1)\xi_1}\,d\xi_1$ has upper and lower limits that are given by the maximum and minimum values of $2k(\boldsymbol{z}_T - \boldsymbol{\gamma}(s))_1/R$, namely, $2k_{\max}z_1/R$ and $2k_{\min}z_1/R$, where R is the *slant range* $\sqrt{z_1^2 + H^2}$. We write $\sin\psi = z_1/R$, where ψ is the angle shown in Figure 9.8. Then

$$\int_{2k_{\min}z_1/R}^{2k_{\max}z_1/R} e^{i(z_1-x_1)\xi_1}\,d\xi_1 = \frac{e^{2ik_{\max}(z_1-x_1)\sin\psi} - e^{-2ik_{\min}(z_1-x_1)\sin\psi}}{i(z_1-x_1)}$$
$$\propto e^{2ik_0(z_1-x_1)\sin\psi}\,\mathrm{sinc}\left((z_1-x_1)\Delta k\sin\psi\right), \qquad (9.26)$$

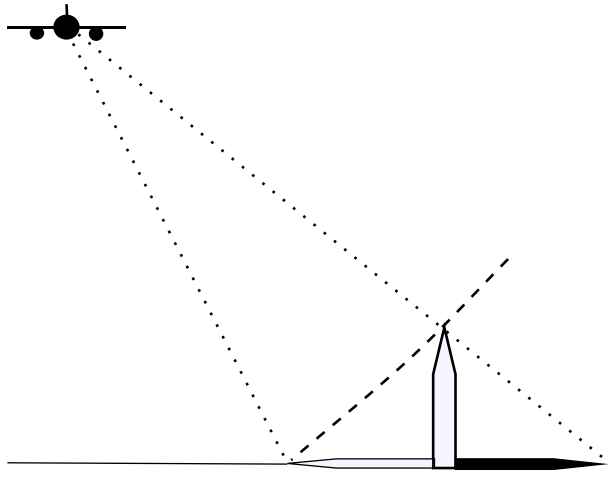

Figure 9.9. *Radar layover and shadow. When an image is formed with the assumption that objects lie on a horizontal plane, objects above the plane appear "laid over" in the direction of the antenna position. The radar shadow of the object appears on the other side.*

where $k_0 = (k_{\max} + k_{\min})/2$ and $\Delta k = k_{\max} - k_{\min}$. This gives us a peak-to-null resolution of $\pi/(\Delta k \sin \psi)$ and a null-to-null resolution of $2\pi/(\Delta k \sin \psi)$. We obtain better resolution for large bandwidth and ψ close to $\pi/2$. Note that ψ close to $\pi/2$ corresponds to a larger range! Thus range resolution is *better* at larger distances, because the projection of the range vector is longer.

9.3 Understanding SAR Images

Because radar images involve a projection that is different from the one involved in optical images, and because we are more accustomed to optical images, radar images often appear to be distorted.

9.3.1 The Radar Projection

Scatterers on the circle formed by the intersection of the constant-range sphere and the iso-Doppler cone will appear at the same point in the image. (This intersection is a vertical circle for the case in which the flight path is horizontal, as shown in Figure 9.5.)

9.3.2 Shadows and Layover

We can often determine the radar trajectory from an image by looking at the shadows in the image. Typically radar images are displayed so that the flight path is across the top of the image. In this orientation, the illuminated portion of an object appears above its shadow, and this is how we are used to seeing optical images. See Figures 9.9, 9.10, and 9.11.

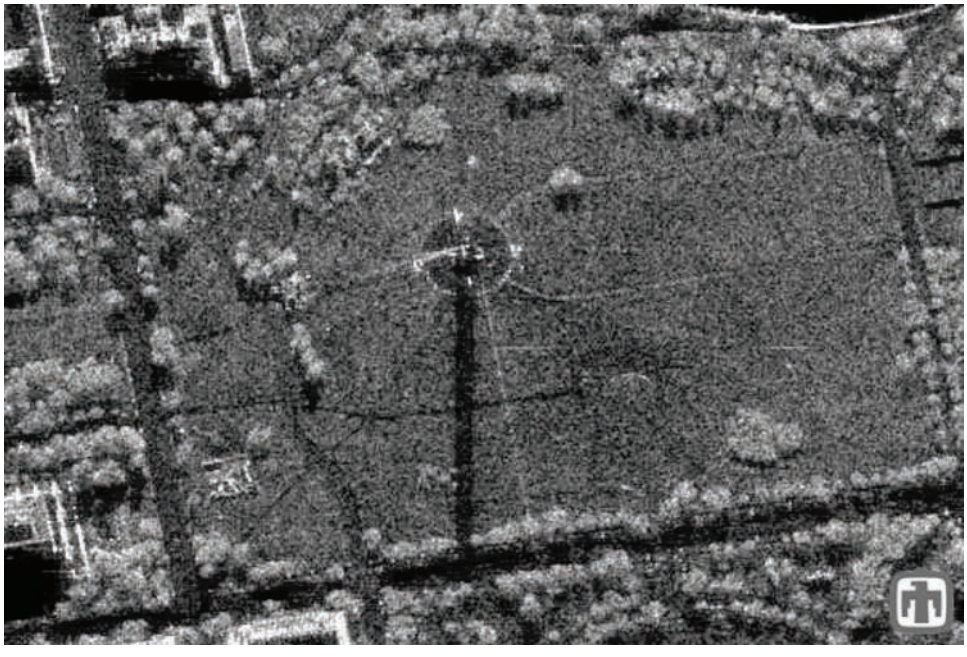

Figure 9.10. *An image of the Washington Monument. The radar antenna flew along the top, as can be seen from the radar shadow of the monument. The top of the monument appears as a bright spot much closer to the radar (courtesy of Sandia National Laboratories).*

Figure 9.11. *The U.S. capitol building in Washington, D.C. Notice the shadows under the trees at the bottom and the layover effect in the image of the dome (courtesy of Sandia National Laboratories).*

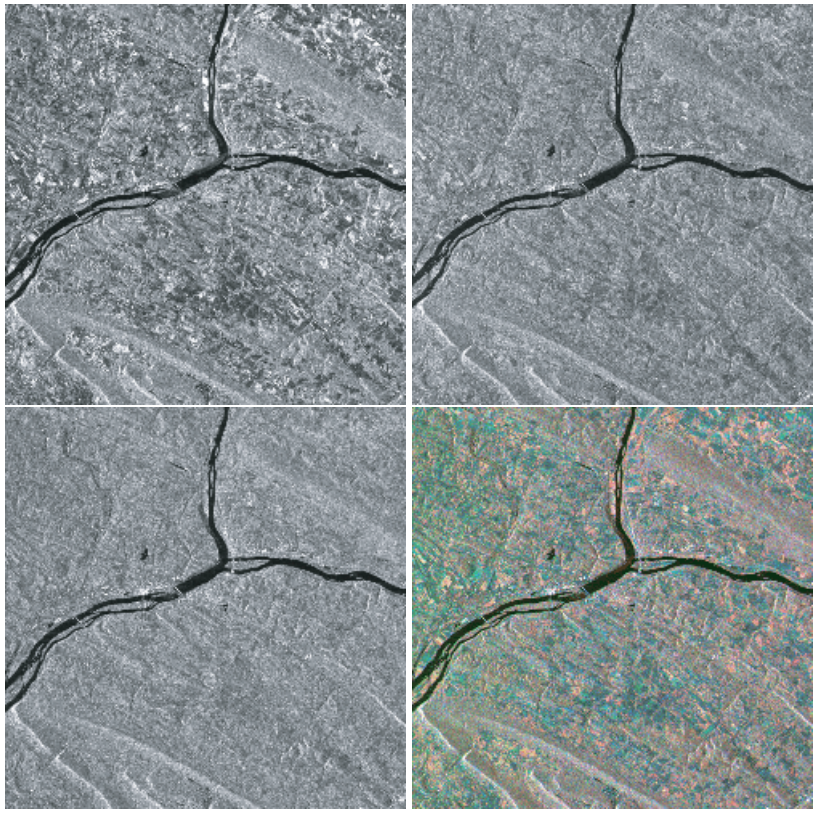

Figure 9.12. *Images at three different frequency bands combined to form a false-color composite image. The top left figure is an L-band image; it is assigned the color red. The top right figure is C-band; it is assigned green; the bottom left is X-band; it is assigned blue. The resulting false-color composite image is at the bottom right (courtesy of NASA/JPL-Caltech).*

Shadows in images often contain more useful information than the illuminated part. An open problem is how to exploit radar shadows to obtain three-dimensional object information [44].

A common distortion is the phenomenon of *layover*, which is the mispositioning of the top of a tall object due to the fact that the top is closer to the radar than the base. See Figures 9.9, 9.10, and 9.11.

9.3.3 Color in SAR Imagery

There is no natural color to SAR imagery. However, false-color SAR images can be produced by combining three channels, typically either three different frequency bands or three polarization channels (HH, VV, and $HV = VH$). One channel is assigned to red, one to green, and one to blue, and the three images are added together. Examples are shown in Figures 9.12, 9.13, and 9.14.

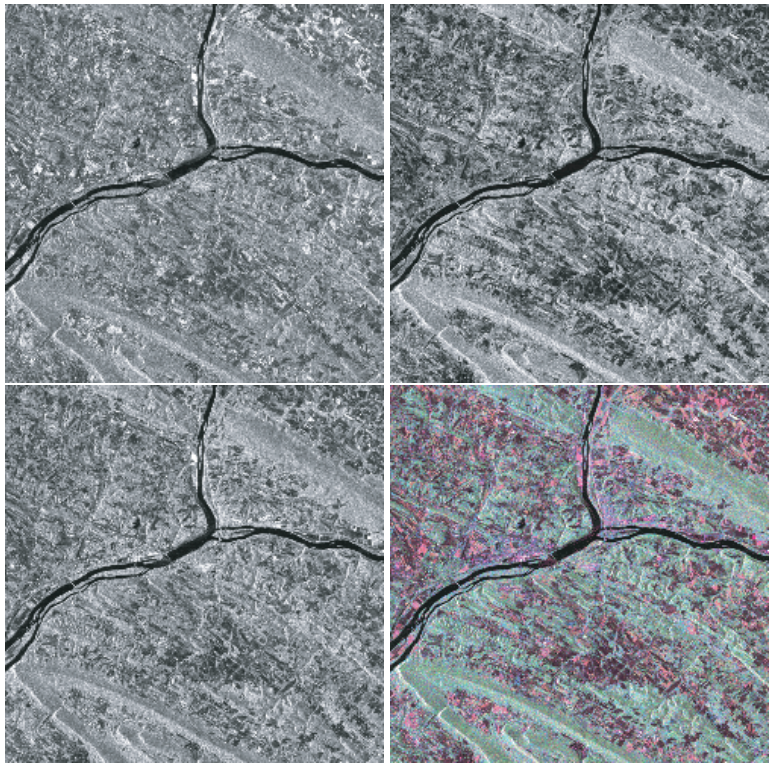

Figure 9.13. *Images from three different polarizations combined to form a false-color composite image. The top left figure is a VV image (i.e., transmit a vertically polarized electric field and measure the scattered vertically polarized electric field); it is assigned the color red. The top right figure is HV; it is assigned green; the bottom left is HH; it is assigned blue. The resulting false-color composite image is at the bottom right (courtesy of NASA/JPL-Caltech).*

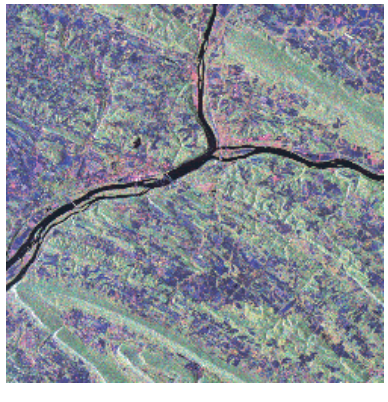

Figure 9.14. *A false-color image obtained by assigning red to the L-band HH image, green to the L-band HV image, and blue to the C-band VV image (courtesy of NASA/JPL-Caltech).*

9.3.4 Singularities and Edges

To understand why singularities appear in the image with the correct location and correct orientation, we need a little microlocal analysis.

For objects in space, their shape is determined by the boundaries between different materials (like air and metal). At these boundaries, we expect the reflectivity function V to have a jump discontinuity, which is a type of singularity.

In images, we are interested in edges, which again is a type of discontinuity or singularity. In particular, we want edges in the image to correspond to boundaries of the object in space.

Characterizing Singularities

Singularities (such as jump discontinuities along a surface or curve) have both a location and a direction. In the case of a jump discontinuity along a surface, the direction is the normal to the surface. This notion is formalized in the following definition.

Definition 9.1. *The point* $(\boldsymbol{x}^0, \boldsymbol{\xi})$ *is* not *in the* wavefront set *of* f *(denoted* $WF(f)$*) if for some smooth cutoff function* ϕ *with* $\phi(\boldsymbol{x}^0) \neq 0$ *the Fourier transform*

$$\int f(\boldsymbol{x})\phi(\boldsymbol{x})e^{i\boldsymbol{\xi}\cdot\boldsymbol{x}}d\boldsymbol{x}$$

decays rapidly in a neighborhood of the direction $\boldsymbol{\xi}$.

In other words, to determine whether $(\boldsymbol{x}^0, \boldsymbol{\xi})$ is in the wavefront set we carry out the following procedure:

1. localize around $\boldsymbol{x}^0$,
2. Fourier transform, and
3. look at decay in direction $\boldsymbol{\xi}$.

Example: A small "point" scatterer $V(\boldsymbol{x}) = \delta(\boldsymbol{x})$. To determine the wavefront set of δ, we localize around various points. If we localize around any $\boldsymbol{x} \neq \boldsymbol{0}$, then ϕV is identically zero, and the function that is identically zero certainly decays rapidly at infinity. Thus for $\boldsymbol{x} \neq \boldsymbol{0}$, $(\boldsymbol{x}, \boldsymbol{\xi}) \notin WF(\delta)$.

If, on the other hand, we localize around $\boldsymbol{x} = \boldsymbol{0}$, then $\phi V = \delta$, and by (8) the Fourier transform of the delta function is a constant. A constant does not decay in any direction. Consequently, all directions are in the wavefront set at the origin. Thus $WF(\delta) = \{(\boldsymbol{0}, \boldsymbol{\xi}) : \text{all } \boldsymbol{\xi} \neq \boldsymbol{0}\}$.

Example: A wall. Another important example is the case of an edge (see Figure 9.15), for which we can use the simple model $V(\boldsymbol{x}) = \delta(\boldsymbol{x} \cdot \hat{\boldsymbol{v}}) \propto \int e^{i\boldsymbol{x}\cdot\hat{\boldsymbol{v}}\rho}d\rho$, where we have used (8). Clearly if we localize around any point for which $\boldsymbol{x} \cdot \hat{\boldsymbol{v}} \neq 0$, the resulting function is

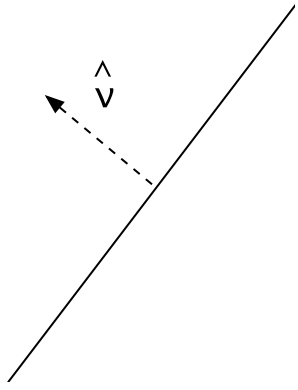

Figure 9.15. *This shows the line where the delta function $\delta(\boldsymbol{x} \cdot \hat{\boldsymbol{v}})$ is supported.*

identically zero, which decays rapidly. On the other hand, if we localize around a point in the support of the delta function, then we discover that the Fourier transform of the result is

$$\mathcal{F}V(\boldsymbol{\xi}) \propto \int \delta(\boldsymbol{\xi} - \hat{\boldsymbol{v}}\rho) d\rho = \begin{cases} 1 & \boldsymbol{\xi} \propto \hat{\boldsymbol{v}}, \\ 0 & \text{otherwise.} \end{cases}$$

Clearly the Fourier transform does not decay rapidly in direction $\hat{\boldsymbol{v}}$. Thus for points satisfying $\boldsymbol{x} \cdot \hat{\boldsymbol{v}} = 0$, the direction of the singularity is $\hat{\boldsymbol{v}}$. This means that the wavefront set is $\mathrm{WF}(\delta(\boldsymbol{x} \cdot \hat{\boldsymbol{v}})) = \{(\boldsymbol{x}, \hat{\boldsymbol{v}}) : \boldsymbol{x} \cdot \hat{\boldsymbol{v}} = 0\}$.

Pseudodifferential Operators

We recall that the SAR image I is related to the ground reflectivity function V by

$$I(\mathbf{z}) = \int K(\mathbf{z}, \mathbf{x})\ V(\mathbf{x}) d\mathbf{x},$$

where K is the PSF (9.22). The right side of (9.22) is the kernel of a *pseudodifferential operator*, which is an operator whose kernel can be written in the form

$$K(\mathbf{z}, \mathbf{x}) = \int e^{i(\mathbf{x}-\mathbf{z})\cdot\boldsymbol{\xi}} a(\mathbf{x}, \mathbf{z}, \boldsymbol{\xi})\, d\boldsymbol{\xi}, \tag{9.27}$$

where the amplitude (filter) a satisfies certain estimates [42, 61, 132].

Example: Differential operators. Taking the amplitude a to be a polynomial gives us a differential operator:

$$\frac{\partial}{\partial z_j} f(\boldsymbol{z}) = -\iint e^{i(\boldsymbol{x}-\boldsymbol{z})\cdot\boldsymbol{\xi}} (i\xi_j)\, d\boldsymbol{\xi}\ f(\boldsymbol{x}) d\boldsymbol{x}, \tag{9.28}$$

$$\nabla^2 f(\boldsymbol{z}) = -\iint e^{i(\boldsymbol{x}-\boldsymbol{z})\cdot\boldsymbol{\xi}} |\boldsymbol{\xi}|^2\, d\boldsymbol{\xi}\ f(\boldsymbol{x}) d\boldsymbol{x}. \tag{9.29}$$

The *order* of a pseudodifferential operator is characterized [42, 61, 132] by the large-$\boldsymbol{\xi}$ behavior of the filter a; for example, (9.28) is of order 1 and (9.29) is of order 2. Smoothing operators have negative orders.

Example: Filters. Most of the filters introduced in section 2.2.2 are examples of pseudodifferential operators in which the amplitude a of (9.27) depends only on $\boldsymbol{\xi}$. For a filter to qualify as a pseudodifferential operator, its transfer function H must satisfy the necessary estimates [42, 61, 132].

Every pseduodifferential operator $\mathcal{K}$ has the *pseudolocal* property, which means that $WF(\mathcal{K}u) \subseteq WF(u)$. We demonstrate that this is the case for (9.22) by means of an example.

The Pseudolocal Property

We consider the example

$$V(\mathbf{x}) = \delta(\mathbf{x}\cdot\hat{\boldsymbol{\nu}}) \propto \int e^{i\mathbf{x}\cdot\hat{\boldsymbol{\nu}}\rho} d\rho. \tag{9.30}$$

In this case, the pseudodifferential operator K operates on V as

$$\begin{aligned}\int K(\mathbf{z},\mathbf{x})\delta(\mathbf{x}\cdot\hat{\boldsymbol{\nu}})d\mathbf{x} &\propto \iint K(\mathbf{z},\mathbf{x})e^{i\mathbf{x}\cdot\rho\hat{\boldsymbol{\nu}}}d\rho d\mathbf{x}\\ &= \iiint e^{i(\mathbf{z}-\mathbf{x})\cdot\boldsymbol{\xi}}\chi(\mathbf{z},\mathbf{x},\boldsymbol{\xi})e^{i\mathbf{x}\cdot\rho\hat{\boldsymbol{\nu}}}\, d\boldsymbol{\xi}d\mathbf{x}d\rho.\end{aligned}$$

We now change variables $\boldsymbol{\xi} \to \rho\tilde{\boldsymbol{\xi}}$ and apply the large-ρ stationary phase theorem to the $\mathbf{x}$ and $\tilde{\boldsymbol{\xi}}$ integrals. The phase is

$$\phi = \rho[(\mathbf{z}-\mathbf{x})\cdot\tilde{\boldsymbol{\xi}} + \mathbf{x}\cdot\hat{\boldsymbol{\nu}}],$$

and for large $\rho = |\boldsymbol{\xi}|$, the leading-order contribution comes from the critical points

$$0 = \nabla_{\tilde{\boldsymbol{\xi}}}\phi \propto (\mathbf{z}-\mathbf{x}), \qquad 0 = \nabla_{\mathbf{x}}\phi \propto (\tilde{\boldsymbol{\xi}} - \hat{\boldsymbol{\nu}}). \tag{9.31}$$

The first of these critical conditions tells us that the point $\mathbf{x}$ appears in the correct location $\mathbf{z} = \mathbf{x}$ in the image, and the second critical condition tells us that the singularity at $\mathbf{x}$ has the correct orientation $\tilde{\boldsymbol{\xi}} = \hat{\boldsymbol{\nu}}$. (Note that the Hessian is nonsingular at the critical point.) Consequently the SAR image of $V(\mathbf{x}) = \delta(\mathbf{x}\cdot\hat{\boldsymbol{\nu}})$ has the form

$$\int K(\mathbf{z},\mathbf{x})\delta(\mathbf{x}\cdot\hat{\boldsymbol{\nu}})d\mathbf{x} \propto \int e^{i\mathbf{z}\cdot\rho\hat{\boldsymbol{\nu}}}\left(\chi(\mathbf{z},\mathbf{z},\rho\hat{\boldsymbol{\nu}}) + \mathcal{O}(\rho^{-1})\right)d\rho.$$

The terms with more rapid decay in ρ, when Fourier transformed, are smoother. Thus we can write

$$\int K(\mathbf{z},\mathbf{x})\delta(\mathbf{x}\cdot\hat{\boldsymbol{\nu}})d\mathbf{x} \propto \int e^{i\mathbf{z}\cdot\rho\hat{\boldsymbol{\nu}}}\chi(\mathbf{z},\mathbf{z},\rho\hat{\boldsymbol{\nu}})d\rho + \text{smoother terms}.$$

Implications for SAR

The fact that the PSF can be written in the form (9.22) tells us that the SAR imaging process has the following properties:

- From the pseudolocal property of pseudodifferential operators, we see that the back-projection operator (9.12) results in an image in which the singularities are in the correct location. We note that it is the *phase* of (9.12) that accomplishes this.
- The imaging operation does not change the orientation of singularities.
- However, singularities *can* disappear if they are not visible from the SAR flight path. This corresponds to the fact that some locations and orientations belong to the set of points $(\boldsymbol{x}, \hat{\boldsymbol{v}})$ where χ is zero. In terms of the stationary phase calculation above, some critical points might lie outside the data collection manifold, in which case they do not contribute to the leading-order behavior of the integral.
- We see from (9.31) that a singularity $(\mathbf{x}, \hat{\mathbf{v}})$ is visible in the image if $\hat{\mathbf{v}}$ is in the data collection manifold at $\mathbf{x}$. Since the data collection manifold consists of vectors $\boldsymbol{\xi} \propto \mathcal{P}\hat{\boldsymbol{R}}_{s,\mathbf{x}}$, this implies that a singularity is visible if $\mathcal{P}\hat{\boldsymbol{R}}_{s,\mathbf{x}} \propto \hat{\mathbf{v}}$, i.e., if the target wavefront set at $\mathbf{x}$ contains a direction that points along the radar line of sight at some point along the flight path.
- The filter Q, which can be computationally expensive to implement, does not affect the location of singularities, but it affects their order and magnitude. In particular, the filter Q determines whether an edge will appear smoothed, and it affects the magnitude of the change in the image across the edge.
  - The dependence of Q on $\mathbf{z}$ (the main computational expense) affects mainly the strength or magnitude of the singularities.
  - The dependence of Q on ω affects the *order* of the singularities in the image. In particular, if Q does not grow sufficiently rapidly with ω, edges in the image will be smoothed. The issue here is the same as that encountered in X-ray computed tomography [87].

9.4 The Effects of Discrete Slow Time

A shortcoming of the continuum model above (in which we use a continuous slow time scale) is that the issues of range ambiguities and Doppler ambiguities are not evident.

To model the transmission of a sequence of pulses, we write the source $j(t, \boldsymbol{y})$ in the form

$$j(t, \boldsymbol{y}) = \sum_n j_n(t - t_n, \boldsymbol{y}) = \sum_n \int e^{-i\omega(t-t_n)} J_n(\omega, \boldsymbol{y}) d\omega, \tag{9.32}$$

where the sum is over n such that $t_n < t$. The transmitted (incident) field (6.9) is then

$$\mathcal{E}^{\text{in}}(t, \boldsymbol{x}, \boldsymbol{y}) \approx \sum_n \int \frac{e^{-i\omega(t-t_n-|\boldsymbol{x}-\boldsymbol{y}|/c)}}{4\pi|\boldsymbol{x}-\boldsymbol{y}|} F_n(\omega, \widehat{\boldsymbol{x}-\boldsymbol{y}}) d\omega, \tag{9.33}$$

where we have used (9.1).

9.4.1 The Received Signal

The field scattered from the reflectivity distribution $V(\boldsymbol{z})$ due to the transmitted sequence (9.33) is obtained by using (9.33) in (6.20):

$$\mathcal{E}_B^{\mathrm{sc}}(t, \boldsymbol{x}, \boldsymbol{y}) \approx -\sum_n \int \frac{e^{-i\omega(t-t_n-(|\boldsymbol{x}-\boldsymbol{z}_T|+|\boldsymbol{z}_T-\boldsymbol{y}|)/c)}}{(4\pi)^2|\boldsymbol{x}-\boldsymbol{z}_T||\boldsymbol{z}_T-\boldsymbol{y}|} V(\mathbf{z}) F_n(\omega, \widehat{\boldsymbol{z}_T-\boldsymbol{y}})\, \omega^2 d\omega d\mathbf{z}. \tag{9.34}$$

The signal received by the antenna located at position $\boldsymbol{\gamma}_n$ is, under the start-stop approximation,

$$d(t) = \int e^{-i\omega t} \sum_n e^{i\omega[t_n+2R_n(\mathbf{z})/c]} A_n(\omega, \mathbf{z}) V(\mathbf{z}) d\omega d\mathbf{z}, \tag{9.35}$$

with $\boldsymbol{R}_n(\mathbf{z}) = \boldsymbol{z}_T - \boldsymbol{\gamma}_n$ and $R_n = |\boldsymbol{R}_n|$ and

$$A_n(\omega, \mathbf{z}) = \frac{\omega^2 F_{\mathrm{rec}}(\omega, \widehat{\boldsymbol{R}}_n(\mathbf{z})) F_n(\omega, \widehat{\boldsymbol{R}}_n(\mathbf{z}))}{(4\pi)^2 [R_n(\mathbf{z})]^2}, \tag{9.36}$$

where F_{rec} denotes the antenna reception pattern.

Thus we see that the scattered field involves a sum over n.

9.4.2 Image Formation

We form the image I as a filtered adjoint applied to the data:

$$I(\mathbf{x}) = \int\int e^{i\omega t} \sum_m e^{-i\omega[t_m+2R_m(\mathbf{x})/c]} Q_m(\omega, \mathbf{x}) d\omega d(t) dt, \tag{9.37}$$

where Q_m is generally taken to be $Q_m = A_m^*$.

Analysis of the Image

Substituting (9.35) into (9.37), we obtain the PSF

$$K(\mathbf{x}, \mathbf{z}) = \sum_{m,n} \int e^{i\omega(t_m-t_n+2[R_m(\mathbf{x})-R_n(\mathbf{z})]/c)} Q_m(\omega, \mathbf{x}) A_n(\omega, \mathbf{z}) d\omega. \tag{9.38}$$

Ambiguities

Assuming that Q_m and A_n are smooth [42, 61, 132], we can analyze (9.38) by the method of stationary phase. The leading-order contributions to (9.38) come from the critical points of the phase

$$\phi(\omega, t_n, t_m) = \omega\left(t_m - t_n + \frac{2}{c}(|\boldsymbol{\gamma}_m - \boldsymbol{x}| - |\boldsymbol{\gamma}_n - \boldsymbol{z}|)\right), \tag{9.39}$$

and are thus obtained as solutions to

$$0 = \partial_\omega \phi = t_m - t_n + \frac{2}{c}(|\boldsymbol{\gamma}_m - \boldsymbol{x}| - |\boldsymbol{\gamma}_n - \boldsymbol{z}|). \tag{9.40}$$

Equation (9.40) shows the presence of range ambiguities: $\boldsymbol{x}$ need not be on the same travel-time sphere about $\boldsymbol{\gamma}_m$ as $\boldsymbol{z}$ is. The sums over n and m in (9.38) are discrete Fourier series and are thus periodic and can exhibit aliasing effects; this gives rise to Doppler ambiguities.

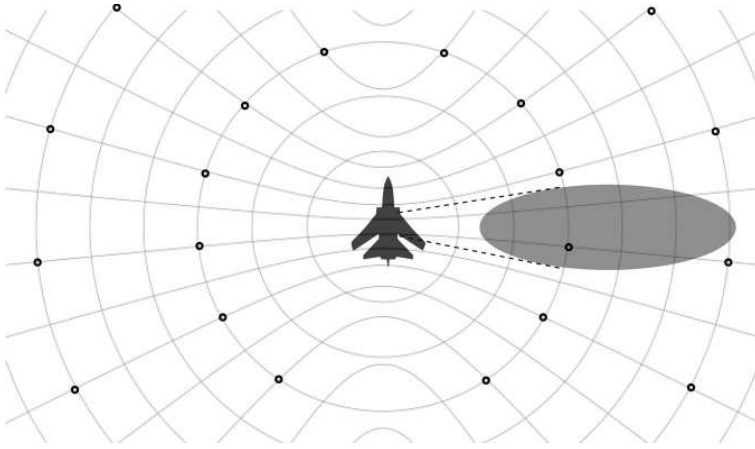

Figure 9.16. *The black dots show SAR ambiguities. The range ambiguities occur at multiples of c/ PRF, where PRF is the pulse repetition frequency. The Doppler ambiguities occur at multiples of the PRF.*

Figure 9.16 shows an example of range, Doppler, and left-right ambiguities in SAR imaging. As the PRF is increased, the system has fewer Doppler ambiguities but more range ambiguities. It is the job of the system designer to find a PRF and antenna beam pattern so that the antenna footprint does not contain ambiguities.

9.5 Other Imaging Algorithms

The image formation algorithm we have discussed here is filtered backprojection. This algorithm has many advantages, one of which is great flexibility. This algorithm can be used for any antenna beam pattern, for any flight path, and for any waveform; a straightfoward extension [91] can be used in the case when the topography is not flat.

Nevertheless, there are various other algorithms that can be used in special cases, for example, if the flight path is straight, if the antenna beam is narrow, or if a chirp waveform is used. Discussions of these algorithms can be found in the many excellent radar imaging books such as [39, 53, 27, 63, 118] that are written for an engineering audience. It is hoped that mathematical readers, having reached this point in the present monograph, are now armed with sufficient background that they will not turn away from discussions that begin, say, with the phase of (9.6) as a starting point.

Chapter 10

Related Techniques

Many of the very challenging problems connected with radar imaging have already been solved, at least in the case when narrow antenna beams can be used. In this chapter, we look briefly at some of the techniques that have been developed.

10.1 Motion Compensation

One of the challenges for airborne systems is atmospheric turbulence, which produces unpredictable variations in the platform location. These variations cause unpredictable changes in the distance between the antenna and the scatterer, which in turn result in unpredictable variations in the phase of the received signal. However, we have seen that this phase is crucial for forming SAR images. Consequently, formation of SAR images from airborne platforms requires *motion compensation*, which is accurate estimation of the antenna position. Currently the antenna position is estimated by (a) using Global Positioning System (GPS) signals to estimate the platform location, then (b) using inertial measurements to correct the GPS estimate, and finally (c) using mathematical algorithms called *autofocus* algorithms [63] to estimate the antenna location directly from the radar data. (see Figure 10.1.) Autofocus algorithms optimize the antenna position so that a quantity such as image contrast is maximized.

10.2 Moving Target Indicator (MTI) Images

In forming SAR images, we assumed that the scene is not moving. Motion in the scene gives rise to mispositioning or streaking (see Figure 10.2). This effect is analyzed in [52].

However, it is of great interest to use radar to identify moving objects; systems that can do this are called *moving target indicator* (MTI) systems or *ground moving target indicator* (GMTI) systems. Such systems are often real-aperture imaging systems. (See Figure 10.3.)

Typically, to obtain information about moving objects, a radar system filters out returns from objects that are not moving. This can be done, for example, by having two antennas on the radar platform, located so that as the platform moves along its trajectory, the second antenna arrives at the same position where the first antenna was located a moment earlier.

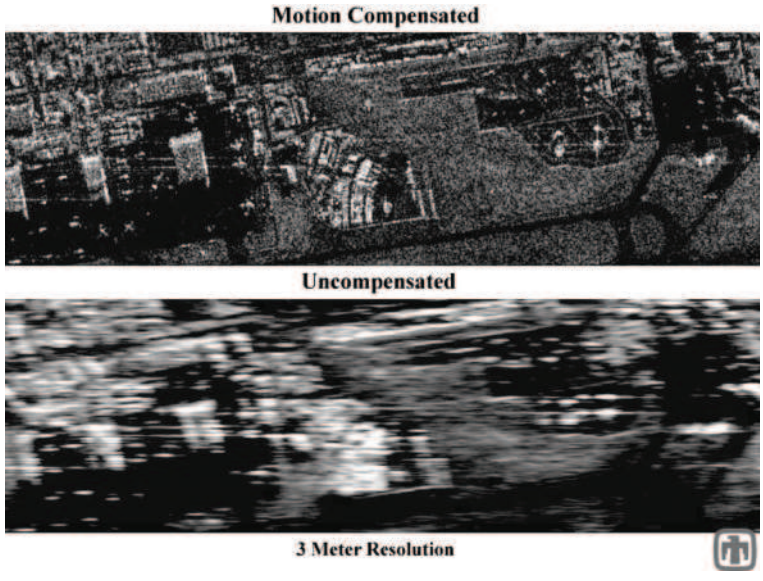

Figure 10.1. *The effect of motion compensation in a Ku-band image (courtesy of Sandia National Laboratories).*

Thus the system collects data from the same antenna position at two slightly different times. Data from the two different times is subtracted, so that what remains are radar returns only from objects that changed during this time. This method is known as the displaced phase center antenna (DPCA) method.

Another approach to moving targets is space-time adaptive processing (STAP) [69], which uses an array of antennas positioned along the azimuthal direction (i.e., along the direction of the flight path). Each antenna produces a range-Doppler plot; these plots are stacked together to create a data cube whose coordinates are range, Doppler, and antenna number. Data from different antennas can be combined with different phases so that the effective beam from the array of antennas is steered to different directions (see section 8.4.4). The radar return from the stationary ground ("ground clutter") appears along a certain ridge in range-Doppler-direction space, and moving targets appear off this ridge.

10.3 Interferometric SAR

Interferometric SAR (IFSAR or InSAR) uses either two antennas on a single platform to obtain topographic information (see Figure 10.4) or two flight passes at different times to assess changes that have taken place during the intervening time [53]. The latter approach is typically used with satellite systems to measure, for example, the flow of a glacier (see Figure 10.5), the earth's movement due to an earthquake (see Figure 10.5), or the swelling of a volcano.

Figure 10.2. *A Ku-band image showing streaking due to objects moving in the scene (courtesy of Sandia National Laboratories and SPIE).*

To explain how SAR interferometry can be used to find ground topography, first we discuss the technique of *stereometry* [53], which is the same principle our brains use to assess distance from the visual information obtained by our two eyes.

10.3.1 Stereometry

Suppose the first flight track is flown at height H, and the second is flown at a distance b and angle of elevation β from the first. (See Figure 10.6.) If the same object can be identified in both images, then its distances (ranges) R_1 and R_2 from the first and second flight track, respectively, can be determined.

From R_1, R_2, b, and β, we can determine the angle of elevation θ from the law of cosines:

$$\begin{aligned} R_2^2 &= R_1^2 + b^2 - 2bR_1 \cos\left(\beta + \frac{\pi}{2} - \theta\right) \\ &= R_1^2 + b^2 + 2bR_1 \sin(\theta - \beta). \end{aligned} \tag{10.1}$$

From knowledge of θ, the object's elevation h can be determined from $h = H - R_1 \cos\theta$.

The difficulty with this method is twofold. First, it requires that common objects be identified in both images; this often requires human intervention. Second, the process is

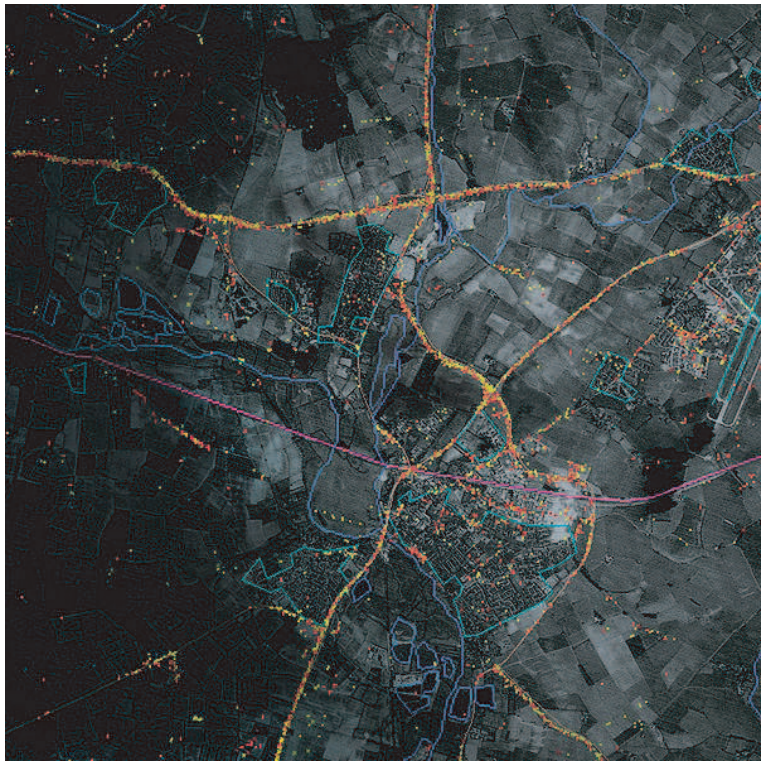

Figure 10.3. *An example of ground moving target indications from the joint surveillance attack radar system, superimposed on a terrain image (courtesy of U.S. Department of Defense).*

very sensitive to errors in the determination of the range difference $\Delta R = R_2 - R_1$. To see this, we use the chain rule

$$\frac{dh}{d(\Delta R)} = \frac{dh}{d\theta}\frac{d\theta}{d(\Delta R)} = R_1 \sin\theta \frac{d\theta}{d(\Delta R)} \tag{10.2}$$

and calculate the derivative $d\theta/d(\Delta R)$ implicitly from (10.1) with $R_2 = R_1 + \Delta R$:

$$\frac{d\theta}{d(\Delta R)} = -\frac{R_1 + \Delta R}{bR_1 \cos(\theta - \beta)}.$$

Using this in (10.2) gives

$$\frac{dh}{d(\Delta R)} = \frac{-(R_1 + \Delta R)\sin\theta}{b\cos(\theta - \beta)} \approx \frac{-R_2}{b}. \tag{10.3}$$

For satellite-borne SAR systems, the ratio R_2/b is very large; for the ERS-1 SAR, for example, R_1 and R_2 are both on the order of 800 km, and the baseline b is about 100 m [53]. Thus in estimating the ground height, range errors are magnified by a factor of 8000;

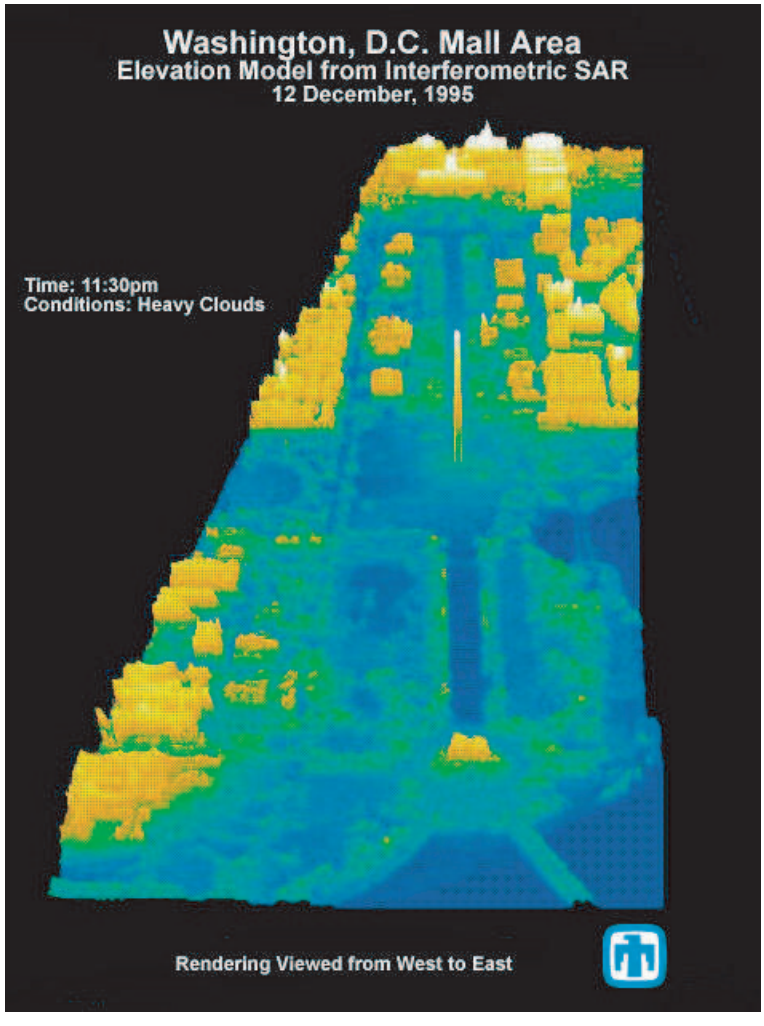

Figure 10.4. *A three-dimensional rendering from interferometric SAR data (courtesy of Sandia National Laboratories).*

the range resolution ΔR, however, is about 10 m, which means that the uncertainty in the estimated height is about 8 km, which is clearly unacceptable. It is for this reason that ground topography is found by interferometry, which provides a much more accurate method to estimate ΔR.

10.3.2 Interferometry

Interferometric SAR (IFSAR) [53] uses narrowband waveforms; thus we take the current density on the antenna to be of the form $j(t, \boldsymbol{y}) = p(t)\tilde{j}(\boldsymbol{y})$ with $p(t) = \tilde{p}(t)e^{-i\omega_0 t}$.

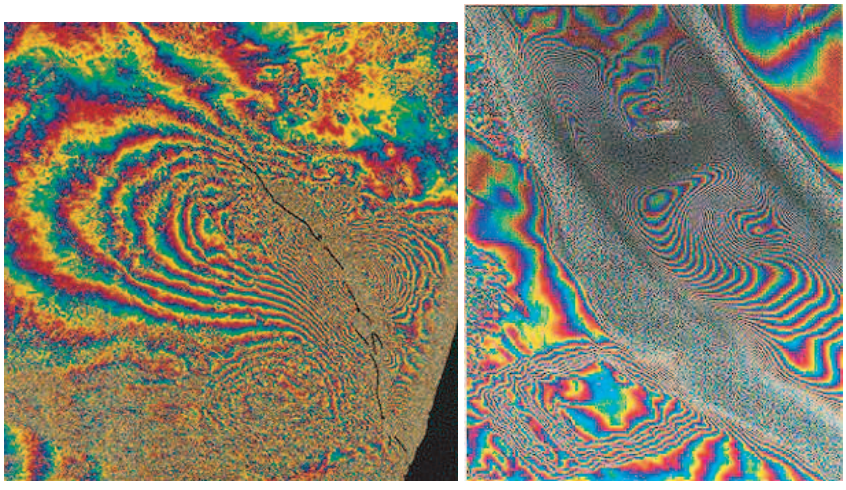

Figure 10.5. *Examples of SAR interferometry used to detect changes. On the left is an interferogram showing changes between April 24, 1992 and August 7, 1992 in a 90-by-110 km area around the Landers (California) fault line. Each color cycle represents a rise in elevation of 28 mm; the black line depicts the fault as mapped in the field. On the right is an interferogram for a glacier in the Himalayas (both images courtesy of NASA/JPL-Caltech).*

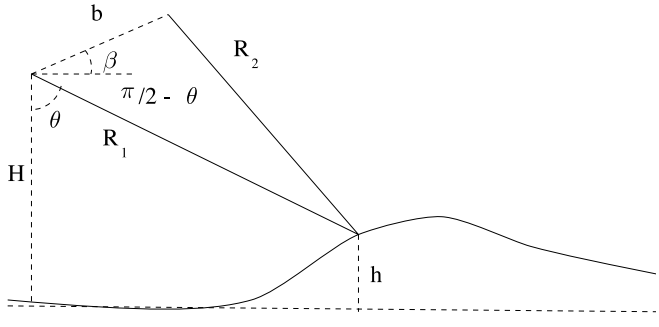

Figure 10.6. *This shows the geometry for stereometry.*

The received signal can therefore be written

$$\begin{aligned} p_{rec}(t,s) &= \iint e^{-i\omega(t-2|\boldsymbol{R}_{s,\boldsymbol{x}}|/c)} P(\omega)\tilde{A}(s,\boldsymbol{x})d\omega V(\boldsymbol{x})d\boldsymbol{x} \\ &= \int \tilde{p}(t-2|\boldsymbol{R}_{s,\boldsymbol{x}}|/c)e^{-i\omega_0(t-2|\boldsymbol{R}_{s,\boldsymbol{x}}|/c)}\tilde{A}(s,\boldsymbol{x})V(\boldsymbol{x})d\boldsymbol{x}. \end{aligned} \tag{10.4}$$

To obtain topography information, we assume that the scattering takes place on a surface $x_3 = h(x_1, x_2)$; thus we write $V(\boldsymbol{x}) = \tilde{V}(\mathbf{x})\delta(x_3 - h(\mathbf{x}))$, where $\mathbf{x} = (x_1, x_2)$. We write $\boldsymbol{x}_T = (\mathbf{x}, 0)$.

In (10.4) we write $\boldsymbol{x} = \boldsymbol{x}_T + h\hat{\boldsymbol{e}}_3$, where $\hat{\boldsymbol{e}}_3$ is a unit vector in the vertical direction, and then use the far-field expansion (7.1) in the form

$$|\boldsymbol{R}_{s,\boldsymbol{x}}| = |\boldsymbol{x} - \boldsymbol{\gamma}(s)| = |\boldsymbol{x}_T + h\hat{\boldsymbol{e}}_3 - \boldsymbol{\gamma}(s)| = |\boldsymbol{x}_T - \boldsymbol{\gamma}(s)| + \underbrace{h\hat{\boldsymbol{e}}_3 \cdot \widehat{(\boldsymbol{x}_T - \boldsymbol{\gamma}(s))}}_{d(\mathbf{x})} + \cdots$$

to write (10.4) as

$$p_{rec}(t, s) = \int \tilde{p}(t - 2|\boldsymbol{R}_{s,\boldsymbol{x}_T}|/c)e^{-i\omega_0(t-2|\boldsymbol{R}_{s,\boldsymbol{x}_T}|/c)}\tilde{A}(s, \boldsymbol{x})\left[e^{-2ik_0 d(\mathbf{x})}\tilde{V}(\mathbf{x})\right]d\mathbf{x}, \quad (10.5)$$

where $d(\mathbf{x}) = h\hat{\boldsymbol{e}}_3 \cdot \widehat{(\boldsymbol{x}_T - \boldsymbol{\gamma}(s))}$ and $k_0 = \omega_0/c$. Equation (10.5) is essentially the signal that would have been obtained from a flat earth with reflectivity function $\left[e^{-2ik_0 d(\mathbf{x})}\tilde{V}(\mathbf{x})\right]$. Thus we see that height information can be thought of as being encoded in the complex phase of the reflectivity function. This information can be extracted by comparing the phases of the two coregistered complex images.

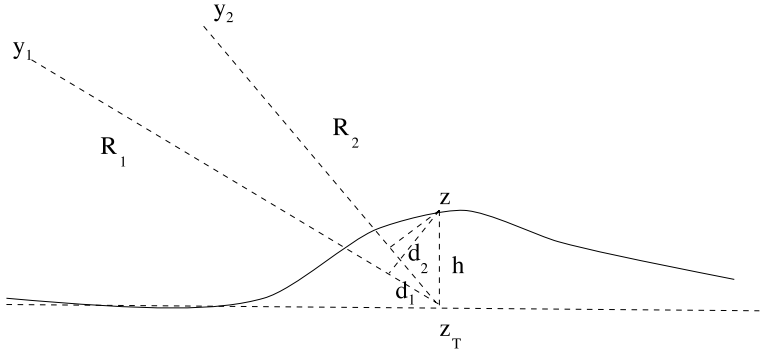

Figure 10.7. *This shows the geometry for IFSAR.*

More specifically, the height information is extracted as follows. Two separate, known flight tracks are each used to produce a complex-valued image, in which the pixel at location $\mathbf{z} = (z_1, z_2)$ represents the quantity $e^{-2ik_0 d(\mathbf{z})}\tilde{V}(\mathbf{z})$. In the jth image, this pixel occurs at range $r_j = |\boldsymbol{y}_j - \boldsymbol{z}_T|$, where $\boldsymbol{y}$ is the center of the synthetic aperture for $\boldsymbol{z}_T$. From Figure 10.7, we see that the true range is $R_j = r_j - d_j \approx |\boldsymbol{y}_j - \boldsymbol{z}_T|$. The two images are coregistered to make $r_1 = r_2$. The complex conjugate of one image is then multiplied by the other, resulting in a complex image whose phase at $\mathbf{z}$ is $2\omega_0(d_1(\mathbf{z}) - d_2(\mathbf{z}))/c$; from this, the range difference $d_1 - d_2$ is found (after solving a phase unwrapping problem). Then (10.1) can be used with $R_2 = R_1 + (d_1 - d_2)$.

The determination of $\Delta R = d_1 - d_2$ can be done with great accuracy—for example, to millimeter accuracy in the case of the ERS-1 satellite [53]. The estimate (10.3) then results in an uncertainty in h of the order of meters.

Chapter 11

Open Problems

In the decades since the invention of SAR, there has been much progress, but many open problems still remain. And most of these open problems are mathematical in nature.

11.1 Problems in Waveform Design

There are many interesting problems related to the design of radar waveforms for various purposes.

11.1.1 Problems in Coding

The coding theory problems typically deal with finding digital waveforms with desirable correlation properties. Many of these problems involve parts of mathematics that have not traditionally been regarded as "applied."

The following seven problems were suggested by Greg Coxson of Technology Service Corporation.

1. A *Barker code* [47] is a binary pulse code whose autocorrelation function has sidelobes whose maximum magnitude is 1. The only known Barker codes are given in Table 11.1. (The autocorrelation of the Barker code of length 5, for example, is the sequence {1, 0, 1, 0, 5, 0, 1, 0, 1}.) An open problem is to prove that no other Barker codes exist. Binary Barker codes of lengths between 14 and 10^{22} have been ruled out [78]. There are no Barker codes of odd length greater than 13 [139].

2. Do polyphase Barker codes [22] of length greater than 77 exist? (A length 77 code was found in [95].) Here the term "polyphase Barker code" refers to a polyphase sequence whose autocorrelation sequence has sidelobes of magnitude no greater than one.

3. Prove the conjecture that for every N, there exists a N-phase Barker code of length N [48].

4. How many digits of measurement precision are needed for N-phase Barker codes?

Table 11.1. *Barker codes.*

Number of bits	Code
2	$++, +-$
3	$++-$
4	$++-+, +++-$
5	$+++-+$
7	$+++--+-$
11	$+++---+--+-$
13	$+++++--++-+-+$

5. Classify autocorrelation-sidelobe-preserving groups for polyphase codes.

6. Develop (approximately) orthogonal code sets, particularly for the case of multiple transmitters and receivers located at different positions.

7. Find optimal radar waveforms when certain frequency intervals (within the radar's frequency band) cannot be used. This problem is becoming increasingly important as the electromagnetic spectrum becomes more crowded.

11.1.2 Problems in Ambiguity Theory

1. Ambiguity volume is not conserved for wideband waveforms, which suggests that it may be possible to design waveforms that can measure both range and velocity to arbitrary accuracy. Characterize such waveforms, and determine how to produce them. (For the wideband ambiguity function, see [128, 37, 5].)

2. How can we combine communications theory and radar ambiguity theory? In particular, can we design signals that produce high-bit-rate communications and also have desirable ambiguity properties?

11.1.3 Design of Waveform for Particular Purposes

1. How can we find waveforms that are best for identifying certain targets (see [67, 55])? What polarization is best for this [57]? The best waveforms would not only enhance scattering from targets of interest, but would also tend to reject clutter and noise (see [43, 114, 152, 141, 153]).

2. Given a desired power spectrum, find a *constant-amplitude* causal waveform that best approximates the desired one (see [102]). (Here "power spectrum" means the squared magnitude of the Fourier transform.) The constraint of constant amplitude is important for amplifier efficiency.

3. Find optimal waveforms for propagation through complex media, including attenuating media, dispersive media [99, 83], and the ionosphere (see [136]).

11.2 Problems Related to Antennas

There are some interesting theoretical questions associated with antennas.

1. How can we best design antennas [2, 3, 4] for various purposes? This is an example of an *inverse source problem* [65, 85, 80, 81]. In formulating the problem, we need to consider not only the radiation pattern, but also whether a given antenna design can be manufactured and fed.

2. How can we design antennas whose properties remain the same over a wide frequency band?

3. For a given frequency band, find the smallest antenna with a given beamwidth. Current antenna research considers not only different shapes but also [58] arrangements of different materials.

4. How can we best exploit the emerging technology of digital waveform generation for use in imaging? It is now possible to build array antennas in which each element is connected to a different signal generator, so that each element can be fed a different waveform. What can be done with such an *agile antenna*? What waveforms should be used for which purposes? How should the different waveforms be scheduled to adapt to a changing scene? These questions apply both in the case when antenna elements are close to each other and when they are far apart.

11.3 Problems Related to Synthetic-Aperture Imaging

1. How can we form images without using the Born approximation? The Born approximation leaves out many physical effects, including not only multiple scattering and creeping waves, but also shadowing and obscuration. But without the Born approximation (or the Kirchhoff approximation, which is similar), the imaging problem is nonlinear. How can we form images in the presence of multiple scattering? (See [21, 30, 92, 56, 145].) Can multiple scattering be exploited to improve resolution? (See [73].)

2. We need to develop scattering models that include as much of the scattering physics as possible, but that are still simple enough for use in the inverse problem. An example of a tractable model that includes relevant physics is [105].

3. Better methods for finding the relative motion between target and sensor are also needed [21, 124]. In particular, when there are multiple scatterers within a resolution cell, constructive and destructive interference may cause the range alignment procedure to break down [20].

4. When the target motion is complex (pitching, rolling, yawing), it may be possible to form a three-dimensional image; fast, accurate methods for doing this are needed [124].

5. How can we form SAR images of moving targets [103]? Moving targets cause Doppler shifts as well as presenting different aspects to the radar [29], and therefore cause artifacts in SAR images. Can we simultaneously track [107] moving objects and form three-dimensional images of them?

6. ISAR imaging and the associated issues need to be more fully developed for the case of a small number of transmitters and receivers [29, 45, 147, 148, 142, 155], which could be positioned far from each other. In this *multistatic* situation, methods need to be developed for establishing the relative phase relationships of the various signals. Methods need to be developed for handing sparse data [34].

7. Improved autofocus algorithms [63, 74] are needed.

8. We would like to develop fast imaging [23, 45, 151] and target-classification algorithms. Such algorithms should run in real time.

9. Theoretical bounds are needed for the target classification / identification problem [66].

10. How can we incorporate prior knowledge about the scene to improve resolution? We would like to go beyond the aperture/bandwidth-defined resolution. One approach that has been suggested is to apply compressive sensing ideas [8, 32, 86] to SAR.

11. How can we fully exploit the polarization information [36, 104, 18, 140] in the scattered field? This problem is closely connected to the issue of multiple scattering: we do not have a linear model that predicts any change in the polarization of the backscattered electric field. Consequently our linear imaging methods cannot provide information about how scatterers change the polarization of the interrogating field. A paper that may be useful here is [134].

12. How can we exploit the information in the radar shadow? In many cases it is easier to identify an object from its shadow than from its direct-scattering image. (See Figure 11.1.) A backprojection method for reconstructing an object's three-dimensional shape from its shadows obtained at different viewing angles is proposed in [44]. What determines the resolution of this reconstruction?

13. Can we exploit antenna agility for SAR?

14. Waves at typical radar frequencies are scattered by foliage. Lower-frequency waves penetrate the forest canopy better but result in lower-resolution images. How can we extract the most information from foliage-penetrating SAR (FOPEN)? Moreover, antennas that efficiently radiate low frequencies must be large; for airborne systems of a reasonable size, the antennas typically have poor directivity, which implies that the resulting imaging systems have left-right ambiguities. In addition, multiple scattering may be important in forested areas, whereas the known methods for forming images neglect multiple scattering. Probably the forest should be modeled as a random medium [134, 137, 65, 117].

    We would like to be able to obtain the bare earth topography and identify objects beneath foliage. We would also like to assess the forest itself [7, 33]: the forestry industry would like information about tree health and trunk volume, and climate modelers would like to know the forest biomass [46, 131].

15. How can we extract the most information from over-the-horizon (OTH) radar, in which electromagnetic energy is bounced off the ionosphere? The ionosphere is a complicated and rapidly changing medium that strongly affects low-frequency radio waves. It is also dispersive, meaning that different frequencies propagate with different speeds.

Figure 11.1. *A 4-inch resolution Ka-band image from Sandia National Laboratories [127]. Note the shadows of the historical airplane, helicopter, and trees (courtesy of Sandia National Laboratories and SPIE).*

16. How can we best use ground-penetrating radar (GPR or GPEN) [9, 26, 104] to obtain information about the ground and structures within it? Soil is a more complicated medium than air, which implies that the corresponding imaging problem is more difficult. In addition, the earth may be in the near field of the antenna, which means that the antenna properties change depending on what is in the soil.

    GPR is of interest in many areas. Global climate modelers would like to assess ice thickness and depth profiles. Civil engineers use GPR to assess the condition of roads and bridges and to identify buried utilities. Archaeologists use GPR to find sites of archaeological interest. GPR systems are being developed to identify land mines [9], unexploded ordinance (UXO), and underground bunkers.

17. How can we do radar imaging through walls [1] and rubble [6]? This can be important for finding victims in disaster areas. We would like to use radar to obtain the building layout and determine where people are located. In many cases, details of the construction of the wall may not be known. How does furniture such as metal desks and file cabinets affect the scattering? Can we detect breathing and heartbeat by exploiting the Doppler shift [31] in the radar signals, even if we cannot form an image?

18. How can we best do radar imaging of urban areas? It is difficult to form SAR images of urban areas, because in cities the waves undergo complicated multipath scattering. Areas behind buildings lie in the radar shadows, and images of tall buildings can overlay other features of interest. (See Figure 9.9.) In addition, urban areas tend to be sources of electromagnetic radiation that can interfere with the radiation used for imaging.

One approach that is being explored is to use a *persistent* or *staring* radar system [50] that would fly in circles [118] around a city of interest. Thus the radar would eventually illuminate most of the areas that would be shadowed when viewed from a single direction. Moreover, the layover effects can potentially be exploited to obtain three-dimensional information. However, this approach also introduces the difficulty that that same object will look different when viewed from different directions. How can the data from a staring radar system be used to obtain the maximum amount of information about the (potentially changing) scene?

19. How can we use radar for medical imaging? This area is sometimes called microwave tomography [112, 19]. It should be possible to use microwaves to form images of the interior of the human body. For this, the far-field approximation is probably inappropriate. We may want to use multiple antennas.

20. Can we use radar to identify individuals by their gestures or gait? Time-frequency analysis of radar signals gives rise to *micro-Doppler* time-frequency images [31], in which the motion of arms and legs can be identified.

21. It is now possible to build radar systems with multiple transmitters and receivers located at different positions. These are often called *multiple-input, multiple-output* (MIMO) radar systems. What can be done with such a system? Particularly if a small number of transmitters and receivers are available, where should they be positioned [138, 29, 150]? How often should they be active? How can images best be formed when sparse, random networks of antennas are used? Is it possible to exploit radiation from radio and TV stations to form images [60, 154, 155]?

22. If sensors are flown on *unoccupied aerial vehicles* (UAVs) , where should they fly? The notion of swarms of UAVs [25] gives rise not only to challenging problems in control theory but also to challenging imaging problems.

23. In many specific applications, we need to learn how to extract useful information from radar images and radar data. From radar images of a scene, can we identify not only the vehicles but also the vehicle type [32] and even individual vehicles? In images of the arctic regions, can we determine ice thickness [100]? How can we combine information from different frequency bands, and how can we combine radar images with those from different sensors such as optical or acoustic ones? For medical microwave tomography, can we determine tissue health from knowledge of its electromagnetic parameters? (See also number 19 above.) Some of these problems will require an understanding of scattering physics, whereas others are more akin to computer vision.

24. Many of these problems motivate a variety of more theoretical open problems, such as the question of whether backscattered data uniquely determines a penetrable object or a nonconvex surface [120, 143]. How can we extend the theory of Fourier integral operators to dispersive media and to nonlinear operators? How can we develop a theory of the information content [70, 98] of an imaging system?

Radar imaging is a mathematically rich field that is ready for more mathematical attention!

Bibliography

[1] F. Ahmad and M. G. Amin, "Noncoherent Approach to Through-the-wall Radar Localization," *IEEE Trans. Aerospace and Electronic Systems*, 42 (No. 4, Oct. 2006), 1405–1419.

[2] E.E. Altshuler and D.S. Linden,"Wire-antenna designs using genetic algorithms," *IEEE Antennas and Propagation Magazine*, 39 (issue 2, Apr. 1997), 33–43.

[3] T.S. Angell and A. Kirsch, "Multicriteria optimization in antenna design," *Math. Methods Appl. Sci.*, 15 (1992), 647–660.

[4] T.S. Angell, A. Kirsch, and R.E. Kleinman, "Antenna control and optimization," *Proc. IEEE.*, 79 (1991), 1559–1568.

[5] R.A. Altes, "Some invariance properties of the wideband ambiguity function," *J. Acoust. Soc. Am.*, 53 (1973), 1154–1160.

[6] I. Arai, "Survivor search radar system for persons trapped under earthquake rubble," in *Microwave Conference*, 2001. APMC 2001, Vol. 2, 2001, 663–668.

[7] J.I.H. Askne, P.B.G. Dammert, L.M.H. Ulander, and G. Smith, "C-band repeat-pass interferometric SAR observations of the forest," *IEEE Trans. Geoscience and Remote Sensing*, 35 (issue 1, Jan. 1997), 25–35.

[8] R. Baraniuk and P. Steeghs, "Compressive radar imaging" in *IEEE Radar Conference*, Waltham, MA, 2007, 128–133.

[9] C. E. Baum (Editor), *Detection and Identification of Visually Obscured Targets*, Taylor & Francis, Philadelphia, PA, 1999.

[10] J. Van Bladel, "Lorenz or Lorentz," *IEEE Antenn. Prop. Magazine*, 32 (1991), 69.

[11] E.G. Bowen, *Radar Days*, Hilgar, Bristol, UK, 1987.

[12] J. Bertrand and P. Bertrand, "Microwave imaging of time-varying targets," *Inverse Problems*, 13 (1997), 621–645.

[13] G. Beylkin and R. Burridge, "Linearized inverse scattering problems in acoustics and elasticity," *Wave Motion*, 12 (1990), 15–52.

[14] G. Beylkin, "Imaging of discontinuities in the inverse scattering problem by inversion of a causal generalized Radon transform," *J. Math. Phys.*, 26 (1985), 99–108.

[15] N. Bleistein, J. K. Cohen, and J.W. Stockwell, *The Mathematics of Multidimensional Seismic Inversion*, Springer, New York, 2000.

[16] N. Bleistein and R.A. Handelsman, *Asymptotic Expansions of Integrals*, Dover, New York, 1986.

[17] R.E. Blahut, W. Miller, and C.H. Wilcox, *Radar and Sonar, Part 1*, Springer, New York, 1991.

[18] W.-M. Boerner and Y. Yamaguchi, "A state-of-the-art review in radar polarimetry and its applications in remote sensing," *IEEE Aerospace & Electronic Systems Magazine*, 5 (June 1990), 3–6.

[19] E.J. Bond, Li Xu, S.C. Hagness, and B.D. Van Veen, "Microwave imaging via space-time beamforming for early detection of breast cancer," *IEEE Trans. Antennas and Propagation*, 51 (Issue 8, Aug. 2003), 1690–1705.

[20] B. Borden, *Radar Imaging of Airborne Targets*, Taylor & Francis, Philadelphia, PA, 1999.

[21] B. Borden, Mathematical problems in radar inverse scattering," *Inverse Problems*, 18 (2002), R1–R28.

[22] P. Borwein and R. Ferguson, "Polyphase sequences with low autocorrelation," *IEEE Trans. Information Theory*, 51 (2005), 1564–1567.

[23] M. Brandfass and W.C. Chew, "Microwave imaging as applied to remote sensing making use of a multilevel fast multipole algorithm," in *Algorithms for Synthetic Aperture Radar Imagery VII*, Proc. SPIE 4053, E.G. Zelnio, ed., Orlando, FL, 2000, 52–63.

[24] R. Buderi, *The Invention that Changed the World*, Simon & Schuster, New York, 1996.

[25] B. Bethke, M. Valenti, and J. P. How, "Cooperative Vision Based Estimation and Tracking Using Multiple UAVs," in *Advances in Cooperative Control and Optimization*, Springer, Berlin, 2007.

[26] L. Carin, N. Geng, M. McClure, J. Sichina, and Lam Nguyen, "Ultra-wide-band synthetic-aperture radar for mine-field detection," *IEEE Antennas and Propagation Magazine*, 41 (Issue 1, Feb. 1999), 18–33.

[27] W. C. Carrara, R. G. Goodman, and R. M. Majewski, *Spotlight Synthetic Aperture Radar: Signal Processing Algorithms*, Artech House, Boston, 1995.

[28] M. Cheney, "A mathematical tutorial on Synthetic Aperture Radar," *SIAM Review*, 43 (2001), 301–312.

[29] M. Cheney and B. Borden, "Imaging moving targets from scattered waves," *Inverse Problems*, 24 (2008), 035005.

[30] M. Cheney and R.J. Bonneau, "Imaging that exploits multipath scattering from point scatterers," *Inverse Problems*, 20 (2004), 1691–1711.

[31] V.C. Chen and H. Ling, *Time-Frequency Transforms for Radar Imaging and Signal Analysis*, Artech House, Boston, 2002.

[32] M. Çetin, W.C. Karl, and D.A. Castañon, "Analysis of the Impact of Feature-Enhanced SAR Imaging on ATR Performance," in *Algorithms for SAR Imagery IX*, Proc. SPIE vol. 4727, 2002, 134–145.

[33] J. Chen, D.S. Simonett, G. Sun, "Computer-aided interpretation of forest radar images," in *Pattern Recognition* 2 (1988), 1245–1249.

[34] W.C. Chew and J.M. Song, "Fast Fourier Transform of Sparse Spatial Data to Sparse Fourier Data," in *IEEE Antenna and Propagation International Symposium* 4 (2000), 2324–2327.

[35] S.R. Cloude, "Polarization coherence tomography," *Radio Science*, 41 (2006) RS4017.

[36] S.R. Cloude and K.P. Papathanassiou, "Polarimetric SAR interferometry," *IEEE Trans. Geoscience and Remote Sensing*, 36 (issue 5, part 1, Sep. 1998), 1551–1565.

[37] L. Cohen, *Time-Frequency Analysis*, Prentice Hall PTR, Upper Saddle River, NJ, 1995.

[38] C.E. Cook and M. Bernfeld, *Radar Signals*, Academic Press, New York, 1967.

[39] I.G. Cumming and F.H. Wong, *Digital Processing of Synthetic Aperture Radar Data: Algorithms and Implementation*, Artech House, Boston, 2005.

[40] J.C. Curlander and R.N. McDonough, *Synthetic Aperture Radar*, Wiley, New York, 1991.

[41] L.J. Cutrona, "Synthetic Aperture Radar," in *Radar Handbook*, 2nd edition, M. Skolnik, ed., McGraw-Hill, New York, 1990.

[42] J.J. Duistermaat, *Fourier Integral Operators*, Birkhäuser Boston, Boston, 1996.

[43] D. DeLong and E. Hofstetter,"On the design of optimum radar waveforms for clutter rejection," *IEEE Trans. Information Theory*, 13 (1967), 454–463.

[44] F.M. Dickey and A.W. Doerry, "Recovering shape from shadows in synthetic aperture radar imagery," in *Radar Sensor Technology XII*, K.I. Ranney and A.W. Doerry eds., Proc. of SPIE Vol. 6947, 2008, 694707.

[45] Y. Ding and D.C. Munson, Jr., "A fast back-projection algorithm for bistatic SAR imaging," in *Proc. of the IEEE International Conference on Image Processing*, Vol. 2, Rochester, NY, 2002, II-449–II-452.

[46] M.C. Dobson, F.T. Ulaby, L.E. Pierce, T.L. Sharik, K.M. Bergen, J. Kellndorfer, J.R. Kendra, E. Li, Y.C. Lin, A. Nashashibi, K. Sarabandi, and P. Siqueira, "Estimation of forest biophysical characteristics in Northern Michigan with SIR-C/X-SAR," *IEEE Trans. Geoscience and Remote Sensing*, 33 (1995), 877–895.

[47] B. Edde, *Radar: Principles, Technology, Applications*, Prentice-Hall, Englewood Cliffs, NJ, 1993.

[48] L. Ein-Dor, I. Kanter, and W. Kinzel, "Low autocorrelated multiphase sequences," *Physical Review E*, 65 (2002), R20102.

[49] C. Elachi, *Spaceborne Radar Remote Sensing: Applications and Techniques*, IEEE Press, New York, 1987.

[50] E. Ertin, C. D. Austin, S. Sharma, R. L. Moses, and L. C. Potter, "GOTCHA experience report: three-dimensional SAR imaging with complete circular apertures," in *Proc. SPIE Vol. 6568*, 2007, 656802.

[51] D.E. Fisher, *A Race on the Edge of Time: Radar—the Decisive Weapon of World War II*, McGraw-Hill, New York, 1988.

[52] J.R. Fienup, "Detecting moving targets in SAR imagery by focusing," *IEEE Trans. Aero. Electr. Systems*, 37 (2001), 794–809.

[53] G. Franceschetti and R. Lanari, *Synthetic Aperture Radar Processing*, CRC Press, Boca Raton, FL, 1999.

[54] F.G. Friedlander, *Introduction to the Theory of Distributions*, Cambridge University Press, New York, 1982.

[55] D.A. Garren, A.C. Odom, M.K. Osborn, J.S. Goldstein, S.U. Pillai, and J.R. Guerci, "Full-polarization matched-illumination for target detection and identification," *IEEE Trans. Aerospace and Electronic Systems*, 38 (2002), 824–837.

[56] J. Garnier and K. Sølna, "Coherent interferometric imaging for Synthetic Aperture Radar in the presence of noise," *Inverse Problems*, 24 (2008), 055001.

[57] D. Giuli, "Polarization diversity in radars," *Proceedings of the IEEE*, 74 (1986), 245–269.

[58] A. Grbic and G.V. Eleftheriades, "A backward-wave antenna based on negative refractive index L-C networks," in *Proceedings of the IEEE Antennas and Propagation Society International Symposium, Vol.* 4, IEEE, Washington, DC, 340–343.

[59] L. Greengard and J.-Y. Lee, "Accelerating the nonuniform fast Fourier transform," *SIAM Rev.*, 46 (2004), 443–454.

[60] H.D. Griffiths and C.J. Baker, "Measurement and analysis of ambiguity functions of passive radar transmissions," in *IEEE International Radar Conference*, IEEE, Washington, DC, 2005, 321–325.

[61] A. Grigis and J. Sjöstrand, *Microlocal Analysis for Differential Operators: An Introduction*, London Math. Soc. Lecture Notes Ser. 196, Cambridge University Press, Cambridge, UK, 1994.

[62] J.D. Jackson, *Classical Electrodynamics*, 2nd ed., Wiley, New York, 1962.

[63] C.V. Jakowatz, D.E. Wahl, P.H. Eichel, D.C. Ghiglia, and P.A. Thompson, *Spotlight-Mode Synthetic Aperture Radar: A Signal Processing Approach*, Kluwer, Boston, 1996.

[64] V. Isakov, *Inverse Source Problems*, AMS, Providence, RI, 1990.

[65] A. Ishimaru, *Wave Propagation and Scattering in Random Media*, IEEE Press, New York, 1997.

[66] A. Jain, P. Moulin, M.I. Miller, and K. Ramchandran, "Information-theoretic bounds on target recognition performance," in *Automatic Target Recognition X*, Proc. SPIE 4050, F.A. Sadjadi, ed., Orlando, FL, 2000, 347–358.

[67] E.M. Kennaugh, "The K-pulse concept," *IEEE Trans. Antennas and Propagation*, 29 (1981), 327–331.

[68] D.M. Kerns, *Plane-Wave Scattering-Matrix Theory of Antennas and Antenna-Antenna Interactions*, NBS Monograph 162, National Bureau of Standards, Washington, DC, 1981.

[69] R. Klemm, *Principles of Space-Time Adaptive Processing*, Institution of Electrical Engineers, London, 2002.

[70] A. Klug and R. A. Crowther, "Three-dimensional image reconstruction from the viewpoint of information theory," *Nature*, 238 (1972), 435–440.

[71] Y. Katznelson, *An Introduction to Harmonic Analysis*, Dover, New York, 1968.

[72] K.J. Langenberg, M. Brandfass, K. Mayer, T. Kreutter, A. Brüll, P. Felinger, and D. Huo, "Principles of microwave imaging and inverse scattering," *EARSeL Advances in Remote Sensing*, 2 (1993), 163–186.

[73] G. Lerosey, J. de Rosny, A. Tourin, and M. Fink, "Focusing beyond the diffraction limit with far-field time reversal," *Science*, 315 (2007), 1120–1122.

[74] F. Lee-Elkin, "Autofocus for 3D imaging," in *Proc. SPIE Vol.* 6970, 2008, 697000.

[75] A. Leon-Garcia, *Probability and Random Processes for Electrical Engineering*, Wiley, New York, 1989.

[76] N. Levanon, *Radar Principles*, Wiley, New York, 1988.

[77] N. Nguyen and Q.H. Liu, "The regular Fourier matrices and nonuniform fast Fourier transforms," *SIAM J. Sci. Comput.*, 21 (1999), 283–293.

[78] K.H. Leung and B. Schmidt, "The field descent method," *Designs, Codes and Cryptography*, 36 (2005), 171–188.

[79] L. Mandel, "Interpretation of instantaneous frequency," *Amer. J. Phys.,* 42 (1974), 840.

[80] E.A. Marengo and A.J. Devaney, "The inverse source problem of electromagnetics: Linear inversion formulation and minimum energy solution," *IEEE Trans. Antennas and Propagation*, 47 (1999), 410–412.

[81] E.A. Marengo, A.J. Devaney, and F.K. Gruber, "Inverse source problem with reactive power constraint," *IEEE Trans. Antennas and Propagation*, 52 (2004), 1586–1595.

[82] D.L. Mensa, *High Resolution Radar Imaging*, Artech House, Dedham, MA, 1981.

[83] J. H. Morales Bárcenas, *Synthetic-Aperture Radar Imaging and Waveform Design for Dispersive Media*, Ph.D. thesis, Rensselaer Polytechnic Institute, Troy, NY, 2008.

[84] W. Moran, "The Mathematics of Radar," in *Twentieth Century Harmonic Analysis*, J. S. Byrnes, ed., Kluwer, Dordrecht, The Netherlands, 2001.

[85] H.E. Moses, "The time-dependent inverse source problem for the acoustic and electromagnetic equations in the one- and three-dimensional cases," *J. Math. Phys.*, 25 (1984), 1905.

[86] R. Moses, M. Çetin, and L. Potter, "Wide angle SAR imaging," in *SPIE Algorithms for Synthetic Aperture Radar Imagery XI*, Orlando, FL, 2004, 164–175.

[87] F. Natterer, *The Mathematics of Computerized Tomography*, SIAM, Philadelphia, 2001.

[88] F. Natterer, M. Cheney, and B. Borden, "Resolution for radar and X-ray tomography," *Inverse Problems*, 19 (2003), S55–S64.

[89] F. Natterer and F. Wübbeling, *Mathematical Methods in Image Reconstruction*, SIAM, Philadelphia, 2001.

[90] R.G. Newton, *Scattering Theory of Waves and Particles*, Dover, Minneola, NY, 2002.

[91] C.J. Nolan and M. Cheney, "Synthetic aperture inversion for arbitrary flight paths and non-flat topography," *IEEE Trans. Image Processing*, 12 (2003), 1035–1043.

[92] C.J. Nolan, M. Cheney, T. Dowling, and R. Gaburro, "Enhanced angular resolution from multiply scattered waves," *Inverse Problems*, 22 (2006), 1817–1834.

[93] C. J. Nolan and W. W. Symes, "Global solution of a linearized inverse problem for the acoustic wave equation," *Comm. Partial Differential Equations*, 22 (1997), 919–952.

[94] D.O. North, "Analysis of the factors which determine signal / noise discrimination in radar," Report PPR 6C, RCA Laboratories, Princeton, NJ, 1943 (classified). Reproduction: D.O. North, "An analysis of the factors which determine signal / noise discrimination in pulsed-carrier systems," in *Proc. IEEE*, 51 (1963), 1016–1027.

[95] C.J. Nunn and G. E. Coxson, "Polyphase pulse compression codes with optimal peak and integrated sidelobes," *IEEE Trans. Aerospace and Electronic Systems*, 45 (2009), 775–780.

[96] C. Oliver and S. Quegan, *Understanding Synthetic Aperture Radar Images*, Scitech, Raleigh, NC, 2004.

[97] A.V. Oppenheim and R.W. Shafer, *Digital Signal Processing*, Prentice-Hall, Englewood Cliffs, NJ, 1975.

[98] J.A. O'Sullivan, R.E. Blahut, and D.L. Snyder, "Information-theoretic image formation," *IEEE Trans. Inform. Theory*, 44 (1998), 2094–2123.

[99] K.E. Oughstun and G.C. Sherman, *Electromagnetic Pulse Propagation in Causal Dielectrics*, Springer, New York, 1997.

[100] J. Paden, S. Mozaffar, D. Dunson, C. Allen, S. Gogineni, and T. Akins, "Multiband multistatic synthetic aperture radar for measuring ice sheet basal conditions," in *Proceedings of IGARSS'04*, Anchorage, AK, 2004, 136–139.

[101] A. Papoulis, *Probability, Random Variables, and Stochastic Processes*, McGraw-Hill, New York, 1965.

[102] L.K. Patton and B.D. Rigling, "Modulus constraints in adaptive radar waveform design," in *Proceedings of IEEE Radar Conference*, 2008, 1–6.

[103] R.P. Perry, R.C. DiPietro, and R.L. Fante, "SAR imaging of moving targets," *IEEE Trans. Aerospace and Electronic Systems*, 35 (1999), 188–200.

[104] R. Pike and P. Sabatier, *Scattering: Scattering and Inverse Scattering in Pure and Applied Science*, Academic Press, New York, 2002.

[105] L.C. Potter and R.L. Moses, "Attributed scattering centers for SAR ATR," *IEEE Trans. Image Processing*, 6 (1997), 79–91.

[106] D. Potts, G. Steidl, and M. Tasche, "Fast Fourier transforms for nonequispaced data: A tutorial," in *Modern Sampling Theory: Mathematics and Applications*, J.J. Benedetto and P. Ferreira, eds., Birkhäuser Boston, Boston, 2001, Chapter 12, 249–274.

[107] K.V. Ramachandra, *Kalman Filtering Techniques for Radar Tracking*, CRC Press, Boca Raton, FL, 2000.

[108] M. Reed and B. Simon, *Methods of Modern Mathematical Physics. Vol. 1: Functional Analysis*, Academic Press, New York, 1972.

[109] J.R. Reitz, F.J. Milford, and R.W. Christy, *Foundations of Electromagnetic Theory*, Addison-Wesley, Reading, MA, 1992.

[110] A.W. Rihaczek, *Principles of High-Resolution Radar*, McGraw-Hill, New York, 1969.

[111] G. Strang, *Linear Algebra and Its Applications*, Academic Press, New York, 1980.

[112] S.Y. Semenov, R.H. Svenson, A.E. Bulyshev, A.E. Souvorov, A.G. Nazarov, Y.E. Sizov, A. Pavlovsky, V.Y. Borisov, B.G. Voinov, G. Simonova, A.N. Starostin, G.P. Tatsis, and V.Y. Baranov, "Three dimensional microwave tomography. Experimental prototype of the system and vector Born reconstruction method," *IEEE Trans. BME*, 46 (1999), 937–946.

[113] B. Simon, *Quantum Mechanics for Hamiltonians Defined as Quadratic Forms*, Princeton University Press, Princeton, NJ, 1971.

[114] S.P. Sira, D. Cochran, A. Papandreou-Suppappola, D. Morrell, W. Moran, S.D. Howard, and R. Calderbank, "Adaptive waveform design for improved detection of low-RCS targets in heavy sea clutter," *IEEE J. Selected Topics in Signal Processing*, 1 (2007), 56–66.

[115] M. Skolnik, *Introduction to Radar Systems*, McGraw-Hill, New York, 1980.

[116] G.S. Smith, "Teaching antenna reception and scattering from a time-domain perspective," *Amer. J. Phys.*, 70 (2002), 829–844.

[117] K. Sobczyk, *Stochastic Wave Propagation*, Elsevier, New York, 1985.

[118] M. Soumekh, *Synthetic Aperture Radar Signal Processing with MATLAB Algorithms*, Wiley, New York, 1999.

[119] I. Stakgold, *Green's Functions and Boundary Value Problems*, 2nd ed., Wiley-Interscience, New York, 1997.

[120] P. Stefanov and G. Uhlmann, "Inverse backscattering for the acoustic equation," *SIAM J. Math. Anal.*, 28 (1997), 1191–1204.

[121] E.M. Stein, *Singular Integrals and Differentiability Properties of Functions*, Princeton University Press, Princeton, NJ, 1970.

[122] G.W. Stimson, *Introduction to Airborne Radar*, SciTech, Mendham, NJ, 1998.

[123] R.M. Stolt, "Migration by change of variables," *Geophysics*, 43 (1978), 23–49.

[124] M.A. Stuff, P. Sanchez, and M. Biancala, "Extraction of three-dimensional motion and geometric invariants," *Multidimensional Systems and Signal Processing*, 14 (2003), 161–181.

[125] W.L. Stutzman and G.A. Thiele, *Antenna Theory and Design*, Wiley, New York, 1998.

[126] R.J. Sullivan, *Radar Foundations for Imaging and Advanced Concepts*, SciTech, Raleigh, NC, 2004.

[127] A.D. Sweet, D.F. Dubbert, A.W. Doerry, G.R. Sloan, and V. Dee Gutierrez, "A portfolio of fine resolution Ku-band miniSAR images: Part I," in *Radar Sensor Technology X*, Proc. SPIE 6210, (2006), 621002.

[128] S.S. Swords, *Technical History of the Beginnings of Radar*, Peregrinus, London, 1986.

[129] D.A. Swick, "A Review of Wideband Ambiguity Functions," NRL Report 6994, 1969.

[130] M.E. Taylor, *Pseudodiferential Operators*, Princeton University Press, Princeton, NJ, 1981.

[131] T. Le Toan, A. Beaudoin, J. Riom, and D. Guyon, "Relating forest biomass to SAR data," *IEEE Trans. Geoscience and Remote Sensing,* 30 (1992), 403–411.

[132] F. Treves, *Basic Linear Partial Differential Equations*, Academic Press, New York, 1975.

[133] F. Treves, *Introduction to Pseudodifferential and Fourier Integral Operators*, volumes I and II, Plenum Press, New York, 1980.

[134] R.N. Treuhaft and P.R. Siqueira, "Vertical structure of vegetated land surfaces from interferometric and polarimetric radar," *Radio Science*, 35 (2000), 141–177.

[135] J. A. Trischman, S. Jones, R. Bloomfield, E. Nelson, and R. Dinger, "An X-band linear frequency modulated radar for dynamic aircraft measurement," in *AMTA Proc.* (Long Beach, CA), AMTA, New York, 1994, 431.

[136] S. Tsynkov, "On SAR imaging through the Earth's ionosphere," *SIAM J. Imaging Sciences*, 2 (2009), 140–182.

[137] L. Tsang, J.A. Kong, and R.T. Shin, *Theory of Microwave Remote Sensing*, Wiley, New York, 1985.

[138] T. Tsao, M. Slamani, P. Varshney, D. Weiner, H. Schwarzlander, and S. Borek, "Ambiguity function for bistatic radar," *IEEE Trans. Aerospace and Electronic Systems*, 33 (1997), 1041–1051.

[139] R. Turyn and J. Storer, "On binary sequences," *Proc. AMS*, 12 (1961), 394–399.

[140] F.T. Ulaby and C. Elachi, eds., *Radar Polarimetry for Geoscience Applications*, Artech House, Norwood, MA, 1990.

[141] T. Varslot, C.E. Yarman, M. Cheney, and B. Yazici, "A variational approach to waveform design for synthetic-aperture imaging," *Inverse Problems and Imaging*, 1 (2007), 577–592.

[142] T. Varslot, B. Yazici, and M. Cheney, "Wideband pulse-echo imaging with distributed apertures in multi-path environments," *Inverse Problems*, 24 (2008), 045013.

[143] T.E. Walsh, " Military radar systems: History, current position, and future forecast," *Microwave J.*, 21 (1978), 87, 88, 91–95.

[144] J.-N. Wang, "Inverse backscattering problem for Maxwell's equations," *Mathematical Methods in the Applied Sciences*, 21 (1998), 1441–1465.

[145] A.B. Weglein, F.V. Araújo, P.M. Carvalho, R.H. Stolt, K.H. Matson, R.T. Coates, D. Corrigan, D.J. Foster, S.A. Shaw, and H. Zhang, "Inverse scattering series and seismic exploration," *Inverse Problems*, 19 (2003), R27–R83.

[146] D. Wehner, *High-Resolution Radar*, 2nd ed., Scitech, Raleigh, NC, 1995.

[147] N.J. Willis, *Bistatic Radar*, Scitech, Raleigh, NC, 1995.

[148] N.J. Willis and H.D. Griffiths, *Advances in Bistatic Radar*, Scitech, Raleigh, NC, 2007.

[149] P.M. Woodward, *Probability and Information Theory, with Applications to Radar*, McGraw-Hill, New York, 1953.

[150] S. Xiao, "Topics in CT and SAR Imaging: Fast Back-Projection Algorithms and Optimal Antenna Spacings," PhD thesis, Univ. of Illinois at Urbana-Champaign, 2001.

[151] S. Xiao, D.C. Munson, S. Basu, and Y. Bresler, "An $N^2 log N$ back-projection algorithm for SAR image formation," in *Proc. 34th Asilomar Conf. on Signals, Systems, and Computers*, Pacific Grove, CA, 2000, 3–7.

[152] B. Yazici, M. Cheney, and C.E. Yarman, "Synthetic-aperture inversion in the presence of noise and clutter," *Inverse Problems*, 22 (2006), 1705–1729.

[153] G. Yazici and G. Xie , "Wideband extended range-Doppler imaging and waveform design in the presence of clutter and noise," *IEEE Trans. Information Theory*, 52 (2006), 4563–4580.

[154] C.E. Yarman and B. Yazici, "Synthetic aperture hitchhiker imaging," *IEEE Trans. Image Processing*, 17 (2008), 2156–2173.

[155] C.E. Yarman, B. Yazici, and M. Cheney, "Bistatic synthetic aperture hitchhiker imaging," in *Proceedings of IEEE International Conference on Acoustics, Speech and Signal Processing*, 2007, I537–I540.

[156] A.H. Zeemanian, *Distribution Theory and Transform Analysis*, Dover, New York, 1965.

Index